

Observation of ^8B Solar Neutrinos from 300-day data at
Super-Kamiokande

Takayuki Yamaguchi

Graduate school of science,
University of Osaka

January, 1998

Acknowledgments

First of all, my sincere appreciation goes to my advisor, Prof. Yorikiyo Nagashima. He introduced me to experimental physics and his serious attitude toward physics always refreshed me. Without his excellent guidance and encouragement on many occasions, this thesis would never have been completed.

I would like to thank Prof. T.Yamanaka, Dr. M.Hazumi, and Dr. T.Hara. They always supported and encouraged me.

I am grateful to Prof. Y.Suzuki for valuable advice about my research activities in this experiment. I extend my thanks to Prof. Y.Totsuka, and Prof. T.Kajita for their kind support to my studies.

I am particularly indebted to the members of the low-energy analysis sub-group of this experiment for sharing daily work of solar neutrino analysis. Prof. M.Nakahata, Dr. K.Inoue, Dr. Y.Takeuchi, Dr. Y.Fukuda, Mr. Y.Koshio, and Dr. K.Martens gave me many fine suggestions and discussions about the solar neutrino analysis and supported me on various occasions. Ms. H.Okazawa, Mr. H.Ishino, Mr. E.Ichihara, Mr. N.Sakurai, Ms. M.Nemoto and Dr. J.Hill assisted me on many occasions.

I would like to thank all the Super-Kamiokande collaborators for help with the experiments. Particular thanks to Dr.Y.Itow. He helped me to maintain High Voltage power supply system.

I owe thanks to my colleagues Mr. K.Adachi, Mr. T.Kawasaki, Mr. K.Hanagaki, Mr. T.Tsuji, Mr. K.Fujita, Mr. Y.Hayato, and Mr. S.Kasuga. They gave me useful discussions and supported me on various occasions.

My thanks go to all graduate students in Nagashima group at Osaka University.

I thank the cooperation of Kamioka Mining and Smelting Company.

At the last, I would like to express my great thanks to Dr. M.Takita. He taught me physics, statistics, hardware and software and I learned from him the whole of the experiments. I will never forget his kindness and useful instructions.

Abstract

The ${}^8\text{B}$ solar neutrino flux ($E_{\text{recoil electron}} \geq 6.5\text{MeV}$) is measured by Super-Kamiokande based on 306.3-day data from May 31, 1996 to June 23, 1997. The total number of recoil electrons scattered by ${}^8\text{B}$ solar neutrinos detected during the detector live days amounts to $4395_{-108}^{+114}(\text{stat.})_{-154}^{+444}(\text{syst.})$ events. The observed ${}^8\text{B}$ neutrino flux is $2.44 \pm 0.06(\text{stat.})_{-0.09}^{+0.25}(\text{syst.})$ [$\times 10^6 \text{cm}^{-2} \text{s}^{-1}$], which should be compared with the standard solar model prediction (BP95) [9] $6.62_{-1.12}^{+0.93}(\text{theo.})$ [$\times 10^6 \text{cm}^{-2} \text{s}^{-1}$]. The ratio of the observed ${}^8\text{B}$ solar neutrino flux to the expected flux (BP95) is $0.368_{-0.009}^{+0.010}(\text{stat.})_{-0.013}^{+0.037}(\text{syst.})_{-0.052}^{+0.062}(\text{theo.})$. The measured ${}^8\text{B}$ solar neutrino flux is consistent with the KAMIOKANDE-II & III results within 1σ , and the deficit in the ${}^8\text{B}$ solar neutrino flux (solar neutrino puzzle) is confirmed.

Neutrino oscillation is proposed as a plausible explanation for the solar neutrino puzzle and possible MSW solutions are examined using the 306.3-day Super-Kamiokande data. A new region is excluded from the currently allowed region on the $(\sin^2 2\theta, \Delta m^2)$ plane. A future prospect is discussed, too.

Contents

1	Introduction	1
2	Solar Neutrinos	5
2.1	SSM(Standard Solar Models)	5
2.2	Solar Neutrino Experiments	9
2.2.1	Homestake Experiment	10
2.2.2	Kamiokande II and III	11
2.2.3	GALLEX and SAGE	12
2.3	Possible solutions to the solar neutrino problem	15
2.3.1	Astrophysical solutions	15
2.3.2	Neutrino Oscillations	18
2.3.3	Allowed region of the MSW effect	24
2.4	Solar neutrino interaction in water	24
3	Super-Kamiokande Detector	28
3.1	Detection principle of solar neutrinos at Super-Kamiokande	29
3.2	Water Tank	30
3.3	Water system	31
3.3.1	Water purification system	31
3.3.2	Radon free air	34
3.4	Inner Detector(ID)	34
3.4.1	PMT in the inner detector	34
3.4.2	Electronics system for inner detector	38
3.5	Outer Detector(OD)	41
3.5.1	Outer-Detector PMT	41
3.5.2	Electronics system for outer-detector	41
3.6	Online DAQ system	42
3.7	Off-line Analysis System	43
3.8	MC simulation of Super-Kamiokande	43
3.8.1	Electron tracking	43
3.8.2	Trigger efficiency	45
4	Calibration	46
4.1	Gain of PMTs	46
4.1.1	Relative Gain of PMTs	46
4.1.2	Single p.e. distribution	47

4.2	Relative Timing of PMTs	49
4.3	Consideration of PMT response in Monte Carlo simulation(MC)	51
4.4	Water Transparency measurement	51
4.4.1	Direct Measurement with laser	52
4.4.2	Measurement with μ -decay electrons	53
4.4.3	Input parameters of our MC simulation	55
4.5	Absolute Energy Scale and Energy resolution Calibrations	57
4.5.1	Definition of Energy Scale	59
4.5.2	Energy Scale Pre-tuning and its Position dependence by Radioactive source	59
4.5.3	LINAC	64
4.5.4	Comparison between Ni and LINAC	67
4.5.5	Long-term stability in energy scale measured by μ -decay electrons	71
4.5.6	Summary	72
5	Data Reduction and Analysis	73
5.1	Data Set	73
5.2	Event Reduction	73
5.2.1	First reduction	73
5.2.2	Second reduction	75
5.3	Final Sample	76
5.3.1	Spallation and γ -ray cuts	76
5.3.2	Summary	79
5.4	Remaining Background	79
6	Results	83
6.1	Extraction of Solar Neutrino Signal	83
6.2	Solar Neutrino Flux	85
6.3	Day-Night Variation of Solar Neutrino Flux	87
6.4	Energy Spectrum of Solar Neutrinos	88
6.5	Systematic errors	91
7	Discussions	93
7.1	Interpretation of Results from Solar Neutrino Experiments	93
7.2	How to incorporate MSW effect	94
7.2.1	Day/Night effect	94
7.2.2	Spectral shape	95
7.2.3	Combined result	96
7.3	Future Prospect	97
8	Conclusions	100
A	Vertex Point Reconstruction(Low-energy Events)	i
A.1	Hit PMT selection	i
A.2	Reconstruction method	iii
A.3	Quality of reconstruction	iv

B Reconstruction of track direction(Low-energy Events)	vi
B.1 Reconstruction Method	vi
B.2 Quality of reconstruction	vii
C Noise cleaner	ix
C.1 Vertex Position Cleaner	ix
C.2 Direction Cleaner	xi
D Muon track fitting	xvi
D.1 Reconstruction method	xvii
D.1.1 Fast reconstruction method	xvii
D.1.2 1st Judgment	xviii
D.1.3 Precise reconstruction	xix
D.1.4 2nd Judgment	xix
D.2 Quality of reconstruction	xx
D.2.1 Event type dependence of the muon fitter	xx
D.2.2 Track reconstruction resolution	xx
E Spallation cut	xxii
E.1 Basic Idea	xxii
E.2 Likelihood function	xxii
E.2.1 $L_{spa}^{DL}(DL, ResQ)$	xxiii
E.2.2 $L_{spa}(DT)$	xxv
E.2.3 $L_{spa}^{ResQ}(ResQ)$	xxvi
E.2.4 How to find a pairing muon	xxvii
E.3 Dead time due to the spallation cut	xxvii
F Energy Determination	xxxii

List of Tables

2.1	Measured solar parameters	5
2.2	Neutrino fluxes predicted by BP95	8
2.3	S-factors of nuclear reaction	9
2.4	Individual neutrino source contributions to ^{37}Cl and ^{71}Ga experiment	10
2.5	S-factors employed by different SSMs and the resultant solar neutrino fluxes	17
4.1	Water transparency measured by laser system.	53
4.2	Thermal neutron capture information	59
4.3	Position dependence of the energy scale obtained by Ni calibration runs	63
4.4	LINAC electron Momentum vs Magnetic field	65
4.5	Systematic error in absolute energy scale	69
4.6	Summary of the energy scale calibration methods	72
5.1	List of radioactive isotopes which decay accompanied with β and/or γ -rays of with energies greater than 6.5MeV	76
5.2	Reduction factor of γ -ray cut	78
6.1	Systematic errors	92
7.1	Observed solar neutrino fluxes by current solar neutrino experiments	93
A.1	Vertex position shift and resolution measured at several positions	v
D.1	Event type dependence of the μ -fitter	xx

List of Figures

1.1	Proton-proton chain	1
1.2	CNO cycle	2
2.1	Temperature distribution	6
2.2	Electron density profile in the sun	7
2.3	Energy spectrum of solar neutrinos	7
2.4	Radial profiles of solar neutrino flux	8
2.5	The time variation of the solar neutrino flux at Homestake experiment	11
2.6	The time variation of the solar neutrino flux ratio at the Kamiokande-II+III	12
2.7	The solar neutrino flux during the daytime and the nighttime at Kamiokande-II+III	13
2.8	Observed flux ratio of ^8B solar neutrinos as a function of recoil electron energy	13
2.9	Solar neutrino flux measured by GALLEX	16
2.10	Solar neutrino flux measured by SAGE	16
2.11	^8B and ^7Be solar neutrino flux constraints from the combined Cl, Ga and Čerenkov experiments	17
2.12	Feynman diagrams of the reaction $\nu_e + e^- \rightarrow e^- + \nu_e$	19
2.13	The MSW effect(adiabatic change) in the Sun	21
2.14	$P(\nu_e \rightarrow \nu_e)$ in the Sun	22
2.15	The density profile in the Earth[21]	22
2.16	$P(\nu_e \rightarrow \nu_e)$ at Super-Kamiokande with earth effect	23
2.17	Definition of δ_{sun}	23
2.18	Allowed regions at 95% C.L. on the $(\sin^2 2\theta, \Delta m^2)$ plane	24
2.19	Feynman diagrams of one-loop electroweak radiative corrections	25
2.20	Feynman diagram of one-loop QCD radiative corrections	26
2.21	$\nu - e$ cross section	26
2.22	Energy spectrum of the recoil electrons	27
3.1	Overview of Super-Kamiokande detector	28
3.2	Relative Čerenkov light spectrum and spectral dependence of quantum efficiency of the inner-detector PMT.	29
3.3	Electronics huts on the tank	30
3.4	Schematic view of Super-Kamiokande tank	30
3.5	PMT mounting	31
3.6	Super-Module	32
3.7	Outer-detector PMT and wavelength shifter	32
3.8	Water purification system	33

3.9	Radon free air system	34
3.10	Inner detector 20-inch-in-diameter PMT	35
3.11	ID PMT base	36
3.12	1 photoelectron(p.e.) distribution of ID PMT.	36
3.13	Time variation of dark noise rate of ID PMT	37
3.14	Helmholtz coils to cancel out the geomagnetic field	37
3.15	The electronics system of Inner detector	38
3.16	The block diagram of ID front-end electronics	39
3.17	Time variation of trigger rate	41
3.18	Schematic view of HV control system	42
3.19	Schematic view of data flow	44
3.20	Trigger efficiency	45
4.1	PMT gain calibration system	46
4.2	Charge distribution after gain calibration	47
4.3	Single charge distribution in unit of pC	48
4.4	Occupancy for barrel PMT	48
4.5	Occupancy for top and bottom PMT	49
4.6	Timing calibration system	50
4.7	TQ-map	50
4.8	Timing resolution of inner-detector PMT	51
4.9	Schematic view of direct measurement of water transparency	52
4.10	Typical stopping muon and μ -decay electron	53
4.11	Schematic view of hit PMT selection for calculation of water transparency	54
4.12	Variation of the detector water transparency measured by μ -decay electrons	55
4.13	The refraction index of water dependent on wavelength	56
4.14	Water transparency	57
4.15	Reflectivity of black sheet	58
4.16	Reflectivity of PMT surface	58
4.17	The transition diagram of $^{58}\text{Ni}(n,\gamma)^{59}\text{Ni}^*$	60
4.18	Schematic view of the calibration system with the radioactive $\text{Ni}+^{252}\text{Cf}$ source	61
4.19	Time distribution measured from fission trigger	62
4.20	Ni distribution at LINAC position	62
4.21	Position dependence of energy scale with Ni data	63
4.22	Schematic view of LINAC	64
4.23	The whole LINAC calibration system	64
4.24	Around the end point of the LINAC beam pipe	65
4.25	Schematic view of the Ge calibration system for the LINAC beam momentum	66
4.26	Deviation of the LINAC beam momentum	66
4.27	Energy distributions of LINAC data at Z=0m and 12m	67
4.28	Comparison between LINAC data and Ni-tuned MC	68
4.29	Energy distribution of LINAC at Z=0m and 12m	69
4.30	Comparison between LINAC data and MC after correcting the energy scale shift.	70
4.31	N_{eff} distributions of μ -decay electrons for data and MC.	71
4.32	Long-term stability of energy scale	72

5.1	Total ID charge distribution of a typical raw data	74
5.2	<i>goodness</i> distribution for raw data.	75
5.3	Zenith angle distribution of the events before γ -ray cut	78
5.4	Definition of effective distance	78
5.5	D_{eff} distributions	79
5.6	Vertex and direction distribution of the events before and after γ -ray cut	80
5.7	Summary of event reduction	81
5.8	Energy Spectrum at each reduction step	82
6.1	Definition of θ_{sun}	83
6.2	Expected $\cos\theta_{sun}$ distribution of recoil electron	84
6.3	$\cos\theta_{sun}$ distribution of the final data(dots) sample	84
6.4	The likelihood distribution of the final sample	86
6.5	Expected day/night ^8B solar neutrino flux variation	87
6.6	Daytime/Nighttime ^8B solar neutrino flux variation	88
6.7	$\cos\theta_{sun}$ distribution of 5 divided nighttime.	89
6.8	Flux of day/night sample	90
6.9	Expected energy spectrum distortion of recoil electrons	90
6.10	Measured energy Spectrum	91
7.1	Excluded region(day/night) at 95% C.L.	95
7.2	Excluded region(energy spectrum) at 95% C.L.	96
7.3	Allowed region(day/night, spectrum and flux) at 95% C.L.	97
7.4	Expected excluded region on the $(\sin^2 2\theta, \Delta m^2)$ plane.	98
A.1	A typical timing distribution of hit PMT	i
A.2	The definition of signal and noise hits	ii
A.3	Vertex position distribution	iv
B.1	likelihood distribution for direction reconstruction	vi
B.2	Distribution of the angle between the direction of the electron from LINAC and the reconstructed direction	vii
B.3	The angular resolution calculated by the MC simulation	viii
C.1	Typical low-energy event which will be removed by the noise cleaner	ix
C.2	Cartoon of a typical misfit low-energy event.	x
C.3	Definition of Δ_{ijl}	x
C.4	ΔV distribution of low-energy event	xi
C.5	$\cos\theta_{sun}$ distribution of low-energy events before and after vertex position cleaner	xii
C.6	A typical MC direction-misfit event	xii
C.7	Typical cumulative distributions of low-energy events	xiii
C.8	“ <i>Dirks</i> ” distributions of real data(Before “spallation cut”, 200-day data(cf. Appendix.E) and ^8B neutrino MC events	xiv
C.9	Reduction factor of the Noise cleaners	xv
D.1	A typical cosmic-ray single-track muon	xvi
D.2	Schematic view of the μ reconstruction	xvii

D.3	A typical stopping muon event and multiple-muon event	xviii
D.4	Definition of l_μ and l_{ph} for precise muon fitter.	xix
D.5	Track resolution of the muon fitter	xxi
E.1	DL distributions	xxiii
E.2	$L_{spa}^i(DL)$ distributions	xxiv
E.3	DT distribution	xxv
E.4	$ResQ$ distributions	xxvi
E.5	$Lspa(ResQ)$ distributions	xxvii
E.6	Spallation likelihood distributions	xxviii
E.7	Dead-time vs Significance	xxix
E.8	Position dependence of dead-time	xxx
F.1	Definition of θ_i and ϕ_i for photo-coverage correction	xxxii
F.2	$R_{cover}(\theta_i, \phi_i)$ distribution on the (θ_i, ϕ_i) plane	xxxii
F.3	The energy scale defined by N_{eff}	xxxiv

Chapter 1

Introduction

The origin of the stellar evolution is, as well known, the nuclear fusion processes in the pp chain and the CNO cycle which Fig.1.1 and 1.2 demonstrate. As shown in these figures, some

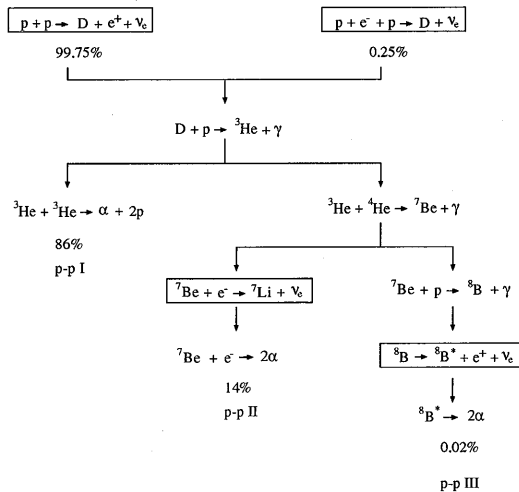


Figure 1.1: Proton-proton chain

reactions emit an electron neutrino(ν_e). Hence, the experimental detection of neutrinos which come from the Sun, the nearest main-sequence star, is a direct evidence for the nuclear fusion processes occurring in the Sun.

Optical observations of the Sun have continuously provided a lot of information on its surface and the theory of the Sun has been developed with the information. The theory is called Standard Solar Model (SSM), and it was extensively developed in 1950s and 1960s as precise optical measurements became available. However, SSM has been improved continuously over past decades stimulated by solar neutrino measurements as well as by solar seismology.

In the late of 1960s, R.Davis and his collaborators started the first pioneering experiment of the solar neutrino measurement in the Homestake Gold Mine, in Lead, South Dakota, U.S.A. In this experiment, they employed an inverse β -decay reaction $\nu_e + {}^{37}\text{Cl} \rightarrow {}^{37}\text{Ar} + e^-$ of which the energy threshold is 0.814 MeV, and counted the number of generated ${}^{37}\text{Ar}$ atoms. Total solar neutrino flux in this experiment was predicted to be 7.5 SNU(Solar Neutrino Unit:

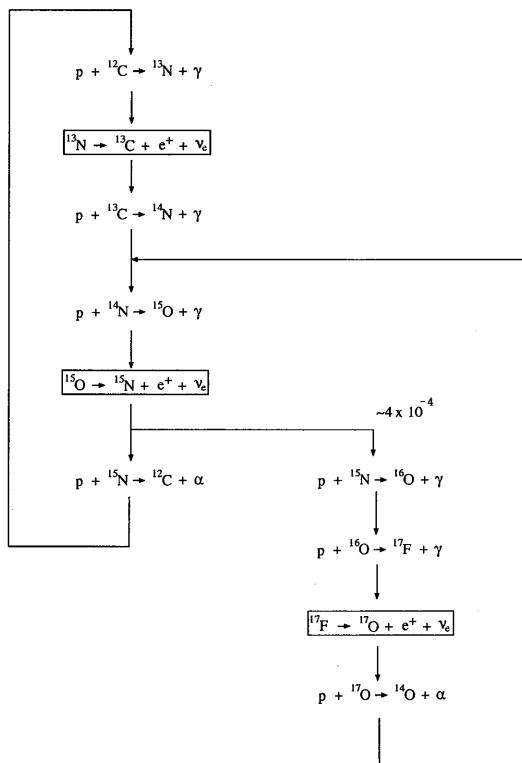


Figure 1.2: CNO cycle

10^{-36} captures/target atom/sec) [2], but the observed rate during the first year of experiment was below 3 SNU [3]. While the experiment proved that origin of the solar energy generation was nuclear fusion processes, it reported an unexpected deficit in the solar neutrino flux in the framework of SSM. The experiment has been continued over 20 years, and the deficit has been unchanged. This deficit in the solar neutrino flux has been called “solar neutrino problem”.

Approximately 20 years later from commencement of the ^{37}Cl experiment, the second solar neutrino experiment called “Kamiokande-II” was started in Kamioka mine, Gifu prefecture, Japan. The detector in its original form was constructed to search for nucleon decays. After some improvements, the detection of solar neutrinos became possible. In this experiment, an imaging water Čerenkov detector with 4,500t of pure water was used, and solar neutrinos above 7.5 MeV, almost all of which come from ^8B β decays, were detected through a recoil electron from neutrino elastic scattering off an orbital electron in water; $\nu + e^- \rightarrow \nu + e^-$. This was the first experiment which had ability to measure direction and energy of the solar neutrinos in real time. Therefore, results from Kamiokande-II are free from doubt of the neutrino sources. The neutrino flux observed in Kamiokande-II from 1987 to 1990 was only $2.7 \times 10^6 \text{ cm}^{-2} \text{ s}^{-1}$ [4][5], while the prediction $6.62 \times 10^6 \text{ cm}^{-2} \text{ s}^{-1}$ [9]. Hence, the previous deficit in the solar neutrino was confirmed.

In 1990s, two other experiments were started; GALLEX at the Gran Sasso Laboratory in Italy, and SAGE at the Baksan Neutrino observatory in Russia. Both of these Gallium radiochemical experiments used a neutrino absorption reaction of $\nu_e + ^{71}\text{Ga} \rightarrow ^{71}\text{Ge} + e$ to detect solar neutrinos. The advantage is its low reaction threshold energy of 0.2332 MeV which made the two experiments sensitive to neutrinos from the pp fusion into deuterium ($E_{max}=0.42\text{MeV}$). The observed neutrino fluxes are

$$\begin{aligned} \text{SAGE}[16] & \quad 69 \pm 10(\text{stat.}) \begin{matrix} +5 \\ -7 \end{matrix} \text{ (SNU)} \\ \text{GALLEX}[15] & \quad 69.7 \pm 6.7(\text{stat.}) \begin{matrix} +3.9 \\ -4.5 \end{matrix} \text{ (SNU)} \end{aligned} \tag{1.1}$$

The predicted rate for the ^{71}Ga experiment is 137_{-7}^{+8} SNU [9]. The solar neutrino flux from the pp and pep reaction is believed to be theoretically robust. Solar neutrino deficit in pp and pep neutrinos is confirmed as well.

To solve the solar neutrino problem, various theoretical efforts have been made. These are classified into two groups; to modify SSM and/or to introduce new neutrino properties to the standard electroweak theory [25] of elementary particles. Especially, among them, the theory of the neutrino flavor oscillations is the most attractive [7]. The extension of the theory to neutrino flavor oscillations in matter advocated originally by L. Wolfenstein and later applied to the solar neutrino problem by S.P. Mikheyev and A. Yu. Smirnov predicts the conspicuous neutrino energy dependence of the deficit in the solar neutrino flux. This is called “MSW solution”. The next-generation experiment “Super-Kamiokande” was started in April, 1996 to make it conclusive whether the deficit is caused by neutrino oscillations.

In this thesis, the result on the ^8B solar neutrino observation in Super-Kamiokande based on 300-day data is reported in detail. The current status of SSM and of solar neutrino experiments, and possible solutions to the solar neutrino problem are described in Chapter 2.

In Chapter 3 and 4, details of the Super-Kamiokande detector and detector calibration are described, respectively. The data analysis is then detailed in Chapter 5. The results and

discussions are summarized in Chapter 6 and 7, respectively, leading to the conclusion in Chapter 8. In addition, the event reconstruction methods are explained in Appendix.

Chapter 2

Solar Neutrinos

2.1 SSM(Standard Solar Models)

The Sun is the nearest star from the Earth, and it is a typical main-sequence star which generates energies by nuclear fusion processes. The overall reaction is represented by



In other words, four protons are fused into one α particle, two positrons, and two electron-neutrinos with a total released energy of 26.73MeV. Actually, this reaction does not occur directly but via several reaction chains. In a main-sequence star, there exist two types of reaction chains; pp-chain and CNO cycle. This reaction schemes are already shown in Fig.1.1 and Fig.1.2, respectively. The major reactions which generate almost all the energy(=luminosity) in a main-sequence star such as the Sun is the pp-chain. Contribution from the CNO cycle to the total solar luminosity is approximately 1.5% in SSM.

As seen in Fig.1.1, there are four processes which generate neutrinos in the pp-chain. Neutrinos from each of these four processes are called “pp”, “pep”, “ ^7Be ”, and “ ^8B ” neutrinos respectively. In addition, there is another process named “hep” in the pp-chain, but it is omitted due to its small contribution(0.00002 %) in this thesis. The energy spectrum of pp and ^8B neutrinos obey a standard continuous β -decay spectrum with an end point energy of 0.420MeV (pp) and ~ 16 MeV (^8B), respectively. On the other hand, pep and ^7Be neutrinos have a monochromatic energy spectrum of 1.42 MeV (pep) , 0.861 MeV (90% of ^7Be) or 0.383 MeV (10% of ^7Be).

Basically, construction of SSM is based on measured solar parameters. They are measured by optical methods and are summarized in Table.2.1. Standard solar models have been developed

Parameter	value
Photon Luminosity(L_{\odot})	$3.844(1 \pm 0.004) \times 10^{33} \text{ erg} \cdot \text{s}^{-1}$
Mass(M_{\odot})	$1.989 \times 10^{30} \text{ kg}$
Radius(R_{\odot})	$6.96 \times 10^8 \text{ m}$
Oblateness	$\leq 2 \times 10^{-5}$
Age	$(4.57 \pm 0.02) \times 10^9 \text{ year}$

Table 2.1: Measured solar parameters

by a number of theorists since 1960's ([8][9][12][13]). In this thesis, when one refers to the standard solar model, it is the one calculated by Bahcall and Pinsonneault in 1995[9] abbreviated as "BP95". It should be noted that the solar neutrino fluxes calculated by different solar models are in good agreement within a difference of 2%[8] or better, when the same input parameters are given.

For construction of SSM, nuclear reaction cross sections, chemical abundance, radiative opacity and solar constants are the most significant input parameters. In calculation, the following conditions are assumed; hydrostatic equilibrium between gravitational force and pressure gradient, mass continuity, energy conservation, energy transportation by radiation or convective motions, energy generation by nuclear reactions, and that variation of chemical abundance is affected only by nuclear reactions. Under these conditions, differential equations of stellar evolution models are numerically calculated by integration and iteration until a good numerical agreement is obtained between the calculated result and the observation. Further, in BP95[9], diffusion effects of not only helium but also other heavy elements are included.

Solar quantities such as mass fractions of hydrogen, helium, and other heavy elements, density distribution, temperature, and neutrino fluxes are determined as a result of solving the stellar evolution equations. In Fig.2.1, 2.2, 2.3, and 2.4, temperature, electron density, and neutrino energy distribution and radial profiles of the neutrino fluxes are demonstrated respectively. As seen in Fig.2.3, the energy of solar neutrinos is less than 20 MeV, and pp

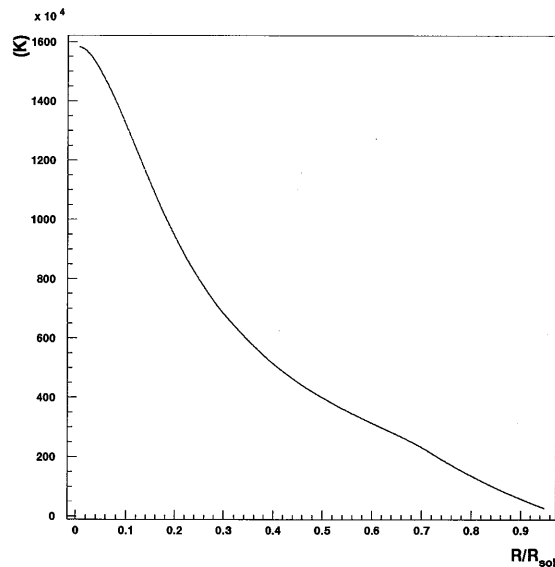


Figure 2.1: Temperature distribution in the Sun predicted by BP95[9] SSM.

neutrinos dominate among them. Almost all the neutrinos have energies less than 2MeV, and the fraction is $\sim 99.98\%$. Numerical values of the solar neutrino fluxes predicted by BP95[9] are listed in Table.2.2.

As described before, the most significant input parameters in SSM are nuclear reaction cross sections, chemical abundance, radiative opacity and solar constants. Therefore theoretical uncertainties in the solar neutrino flux originate mainly from uncertainties in these parameters.

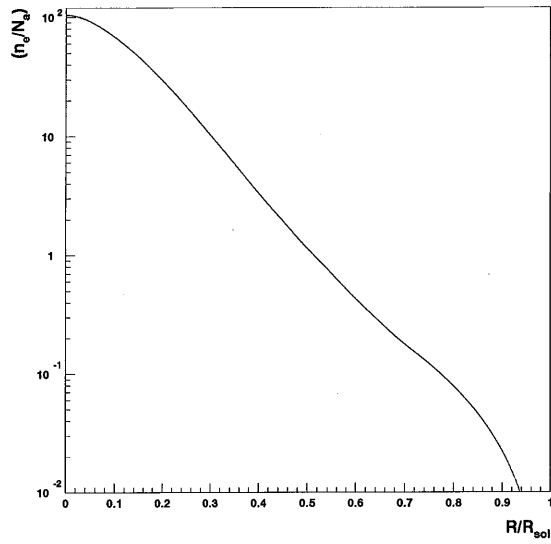


Figure 2.2: Electron density profile in the Sun predicted by BP95[9]. n_e and N_a represent the electron density and the Avogadro's number, respectively.

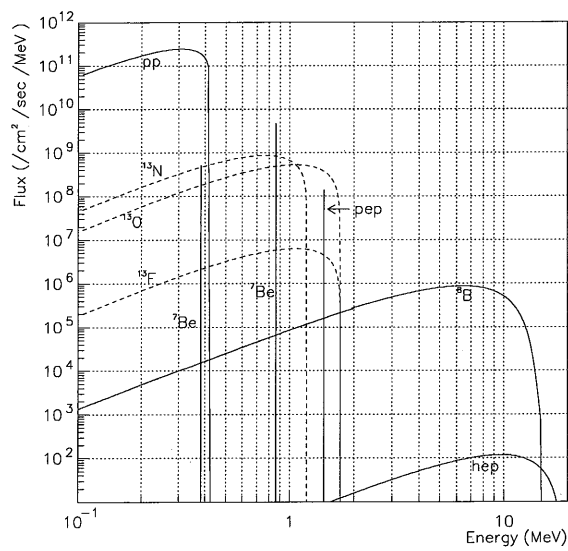


Figure 2.3: Energy spectrum of solar neutrinos predicted by BP95[9]

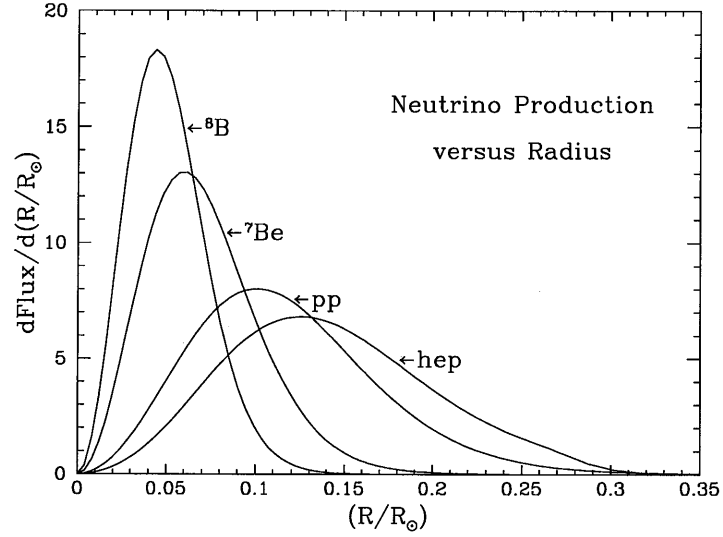


Figure 2.4: Radial profiles of solar neutrino flux

Neutrino Source	Flux($\text{cm}^{-1}\text{s}^{-1}$)
pp	$5.91(1.00^{+0.01}_{-0.01}) \times 10^{10}$
pep	$1.40(1.00^{+0.01}_{-0.02}) \times 10^8$
^7Be	$5.15(1.00^{+0.06}_{-0.07}) \times 10^9$
^8B	$6.62(1.00^{+0.14}_{-0.17}) \times 10^6$
hep	1.21×10^3
^{13}N	$6.18(1.00^{+0.17}_{-0.20}) \times 10^8$
^{15}O	$5.45(1.00^{+0.19}_{-0.22}) \times 10^8$
^{17}F	$6.48(1.00^{+0.15}_{-0.19}) \times 10^6$

Table 2.2: Neutrino fluxes predicted by BP95[9]. Errors in this table is one σ .

The dependence of the neutrino fluxes on the input parameters can be expressed in the power-law relations as,

$$\phi(\text{pp}) \propto S_{11}^{0.14} S_{33}^{0.03} S_{34}^{-0.06} L_{\odot}^{0.73} (Z/X)^{-0.08} (\text{Age})^{-0.07} \quad (2.2)$$

$$\phi(^7\text{Be}) \propto S_{11}^{-0.97} S_{33}^{-0.43} S_{34}^{0.86} L_{\odot}^{3.46} R_{\odot}^{0.22} (Z/X)^{0.58} (\text{Age})^{1.3} \quad (2.3)$$

$$\phi(^8\text{B}) \propto S_{11}^{-2.6} S_{33}^{-0.40} S_{34}^{0.81} S_{17}^{1.0} L_{\odot}^{6.8} R_{\odot}^{0.48} (Z/X)^{1.3} (\text{Age})^{1.3} \quad (2.4)$$

where L_{\odot} is the total solar luminosity, R_{\odot} is the solar radius, (Z/X) is the initial chemical abundance ratio of heavy elements to hydrogen which is equal to 0.0245 in BP95[9], Age is the solar age, and S is astrophysical S-factors defined by

$$S = \sigma(E) \cdot E \cdot e^{2\pi\eta(E)} \quad (2.5)$$

$$\eta(E) = \frac{2\pi Z_1 Z_2 e^2}{hv} \quad (2.6)$$

where $\sigma(E)$ is the cross section for the reaction, $\eta(E)$ is the Sommerfeld parameter, v is the relative velocity of two particles in the initial state, Z_1 and Z_2 are their charges, and E is the relative energy. The suffix i and j of S_{ij} represent the atomic numbers which are involved in the reaction, for instance, S_{17} stands for the reaction $^7\text{Be} + p \rightarrow ^8\text{B} + \gamma$. Then, the S-factors used in BP95[9] are summarized in Table.2.3 As seen in Eq.2.2, 2.3, and 2.4, the pp neutrino

Reaction ($S_{ij}(0)$)	value($eV \cdot b$)
$^1\text{H}(p, e^+ \nu_e)^2\text{H}$ (S_{11})	$3.89(1 \pm 0.011) \times 10^{-19}$
$^3\text{He}(^3\text{He}, 2p)^4\text{He}$ (S_{33})	$4.99(1 \pm 0.06) \times 10^6$
$^3\text{He}(^4\text{He}, \gamma)^7\text{Be}$ (S_{34})	$5.23(1 \pm 0.032) \times 10^2$
$^7\text{Be}(p, \gamma)^8\text{B}$ (S_{17})	$22.4(1 \pm 0.093)$

Table 2.3: S-factors of nuclear reaction

flux is relatively insensitive to all of the input parameters but total solar luminosity. The total solar luminosity has been measured by several satellites, and its uncertainty is estimated to be $\pm 0.4\%$ [9]. On the contrary, ^7Be and ^8B solar neutrino fluxes are very sensitive to the input parameters. Furthermore, the neutrino fluxes also depend on the temperature in the Sun and the temperature dependence is described as

$$\phi(\text{pp}) \propto T^{-1.2}, \quad \phi(^7\text{Be}) \propto T^8, \quad \phi(^8\text{B}) \propto T^{18} \quad (2.7)$$

where T is the temperature of the solar core. The ^8B solar neutrino flux is very sensitive to it compared with others. For example, if it is 4% lower, the ^8B neutrino flux becomes half, while pp and ^7Be neutrino fluxes become 5% higher and 30% lower, respectively.

2.2 Solar Neutrino Experiments

Since 1968, prior to Super-Kamiokande, there have been four solar neutrino experiments: Homestake, Kamiokande-II+III, GALLEX, SAGE. In this section, these 4 experiments are explained and recent results from these are summarized.

2.2.1 Homestake Experiment

The Homestake experiment is the first pioneering experiment to observe solar neutrinos and it has been operated since 1968 by R.Daivis and his collaborators. This experiment uses the inverse β -decay reaction to detect solar neutrinos:



The threshold energy of this reaction is 0.814MeV. An ${}^{37}\text{Ar}$ atom decays into ${}^{37}\text{Cl}$ via electron capture and it releases a 2.82keV Auger electron at the decay. The half life of ${}^{37}\text{Ar}$ is 35days. In this experiment, they use 3.8×10^5 liters (corresponding to 615 metric tons) of liquid perchloroethylene (C_2Cl_4) contained in a horizontal cylindrical-tank, which includes 2.16×10^{30} ${}^{37}\text{Cl}$ target atoms(natural abundance = 24.23%) . The ${}^{37}\text{Ar}$ atoms produced in the detector are extracted by helium gas bubbling operated every 3 months. After bubbling, the number of ${}^{37}\text{Ar}$ atoms is measured by counting the Auger electron with a proportional counter. In order to eliminate cosmic-ray muons which cause the serious background, the detector is located at a depth of 1480m underground(4400m water equivalent) in the Homestake Gold Mine at Lead, South Dakota(U.S.A).

The expected rate is $9.3_{-1.4}^{+1.2}$ SNU(Solar Neutrino Unit: 10^{-36} captures/target atom/sec) from SSM of BP95[9]. The contribution to the 9.3 SNU from individual neutrino sources is summarized in Table.2.4. The Homestake experiment is sensitive to ${}^7\text{Be}$ and ${}^8\text{B}$ solar neutrinos.

Neutrino source	Cl (SNU)	Ga (SNU)
pp	0.00	69.7
pep	0.22	3.0
${}^7\text{Be}$	1.24	37.7
${}^8\text{B}$	7.36	16.1
${}^{13}\text{N}$	0.11	3.8
${}^{15}\text{O}$	0.37	6.3
Total	$9.3_{-1.4}^{+1.2}$	137_{-7}^{+8}

Table 2.4: Individual neutrino source contributions to the calculated event rates in ${}^{37}\text{Cl}$ and ${}^{71}\text{Ga}$ experiments[9]. The error corresponds to 1σ .

The average flux measured at the Homestake experiment is

$$2.55 \pm 0.14(\text{stat.}) \pm 0.14(\text{syst.}) \text{ SNU}. \quad (2.9)$$

This result is significantly smaller than SSM prediction(9.3 SNU). Namely, the ratio, Data/SSM becomes

$$0.273 \pm 0.021. \quad (2.10)$$

Subsequently, the Homestake experiment claimed possible time variation of the solar neutrino flux as is shown in Fig.2.5. Several papers pointed out that there might exist possible anti-correlation between sunspot numbers(solar cycle) and the observed solar neutrino flux at the Homestake experiment. In Fig.2.5, the time variation of the sunspot numbers is also overlaid

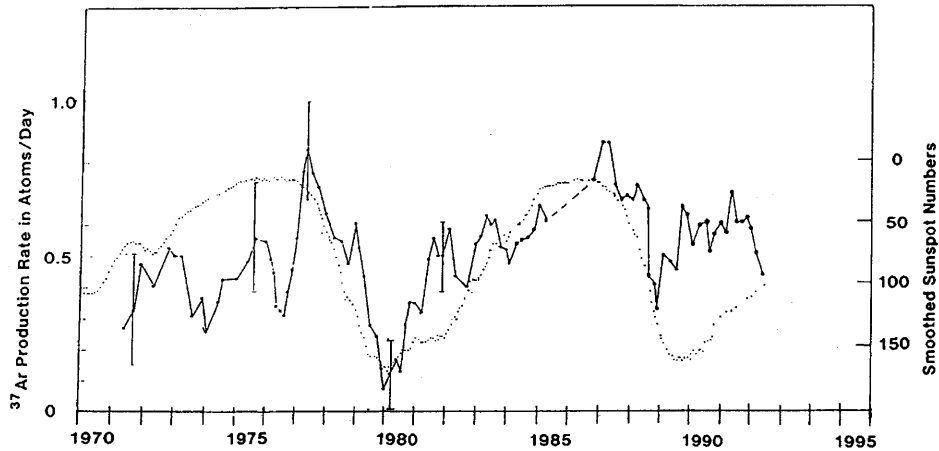


Figure 2.5: The time variation of the solar neutrino flux at the Homestake experiment (data points), together with the time variation of the sunspot numbers.

for comparison. If this anti-correlation actually existed, it would imply new intrinsic properties of the neutrino, for example, a finite mass and/or a large magnetic moment, as the core region of the Sun where the solar neutrinos are generated is thought to be stable. Yet, as seen in Fig.2.5, this possible anti-correlation may not be recognized since 1989. The apparent time variation was also studied by Kamiokande-II+III, and there was no such evidence. This will be described in Subsection.2.2.2.

2.2.2 Kamiokande II and III

The solar neutrino measurement by the Kamiokande-II detector was started in January 1987 and ended in April 1990 for the detector upgrade to Kamiokande-III. After upgrading the detector, the measurement by Kamiokande-III started in December 1990 and finished in February 1995. The Kamiokande detector is an imaging water Čerenkov counter with 4500 tons of water located about 1000m underground(2700m water equivalent) in the Mozumi mine, Kamioka town, Gifu prefecture, Japan.

The solar neutrino measurement by Kamiokande-II+III is based on neutrino-electron elastic scattering($\nu_e + e \rightarrow \nu_e + e$). The detector detects Čerenkov light photons radiated from the recoil electron and is sensitive to only ^8B solar neutrinos. As described in Section.2.4, one big advantage of the detector is that the direction of the incident neutrino can be measured. Kamiokande-II is the first experiment which established an evidence for the detection of neutrinos coming from the Sun.

The total effective live time of Kamiokande-II+III is 2079 days. The threshold energy is 9.3MeV for the first 449 days, 7.5MeV for the next 594 days, and 7.0MeV for the last 1036 days. The ^8B solar neutrino flux is measured to be

$$2.80 \pm 0.19(\text{stat.}) \pm 0.33(\text{syst.}) \times 10^6 (\text{cm}^{-2}\text{sec}^{-1})[6], \quad (2.11)$$

which should be compared with the flux predicted by BP95[9];

$$6.62 \begin{matrix} +0.93 \\ -1.13 \end{matrix} \times 10^6 \text{ (cm}^{-2}\text{sec}^{-1}\text{)}. \quad (2.12)$$

Thus, the ratio of DATA/SSM is

$$0.423 \pm 0.029(\text{stat.}) \pm 0.050(\text{syst.}). \quad (2.13)$$

In Fig.2.6, the time variation of the observed solar neutrino flux is shown. From this figure, no significant correlation between the neutrino flux and the sunspot numbers(already shown in Fig.2.5) was seen within the error bars.

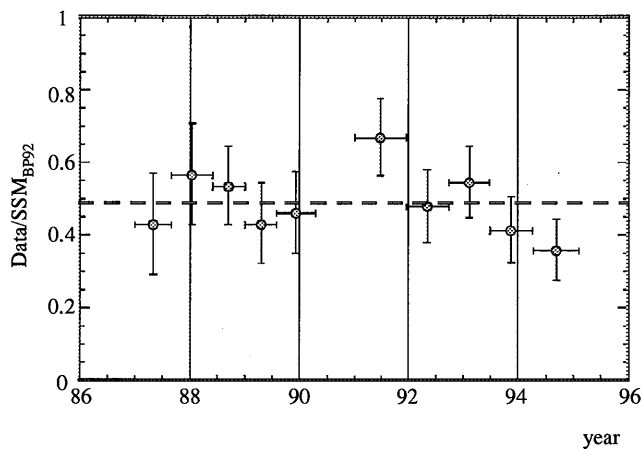


Figure 2.6: The time variation of the solar neutrino flux ratio at the Kamiokande-II+III. The dashed line is the average flux ratio for the entire time periods. The standard solar model employed in the figure is BP92[8].

Further, as described in Section.2.4, the Kamiokande-II+III detectors can measure arrival time of the incident neutrino and recoil electron energy. In Fig.2.7, and 2.8, the solar neutrino flux during the daytime when the Sun is above the horizon and the nighttime and the energy spectrum of recoil electrons are shown, respectively. Difference in flux between the daytime and the nighttime as well as difference in energy spectrum between the data and SSM prediction are very important to confirm neutrino oscillations caused by the MSW effect, which is described in Section.2.3.2. Yet, in Kamiokande-II+III, these possible differences were not observed.

2.2.3 GALLEX and SAGE

Both GALLEX and SAGE are radiochemical experiments similar to Homestake and use ^{71}Ga as target atoms to detect solar neutrinos, by means of the following reaction:



Threshold energy of this reaction is 0.233MeV. Thus, the ^{71}Ga experiments are currently the only one which is sensitive to pp neutrinos having an end point energy of 0.42MeV. The theoretical

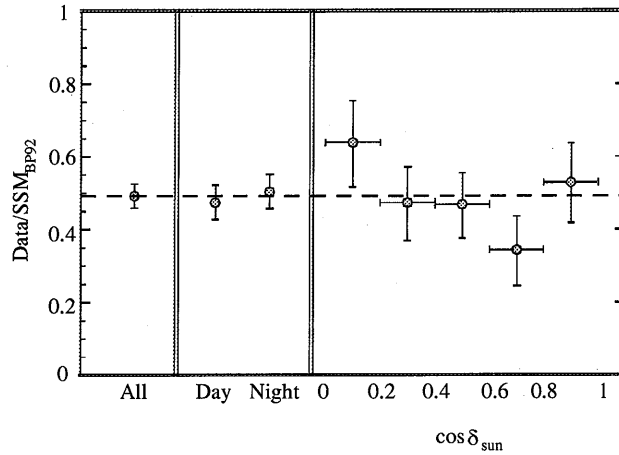


Figure 2.7: The solar neutrino flux during the daytime and the nighttime. The nighttime data sample is divided into 5 subsamples as a function of direction with respect to the Sun where δ_{sun} is defined in Fig.2.17. The standard solar model employed is BP92[8]. The dashed line is the average flux ratio for the entire time period.

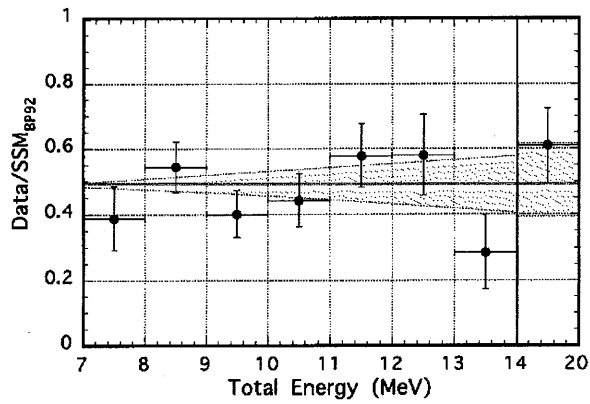


Figure 2.8: Observed flux ratio of ^8B solar neutrinos as a function of recoil electron energy. The hatched area shows the range of systematic uncertainty.

calculation of the pp neutrino flux is believed to be robust. Its variation typically less than, or of the order of 2% among recent solar models[8][9][10][11].

The radioactive ^{71}Ge atom decays into ^{71}Ga via electron capture, the inverse of the reaction in Eq.2.14, with a half-life of 11.43 days. To count the number of ^{71}Ge atoms, Auger electrons and X-rays emitted in the ^{71}Ge electron capture are measured. The energies of the Auger electrons are 10.367keV(41.5 %), or 1.17keV with 9.2keV X-ray(5.3 %), or 0.12keV with 10.26keV X-ray(41.2 %), in the K-electron capture mode, 1.2keV(10.3 %) in the L-electron capture mode, and 0.12keV(1.7 %) in the M-electron capture mode, respectively.

The GALLEX experiment started in 1991 and finished in 1997. Its detector is located at the Gran Sasso Underground Laboratory(3300m water equivalent) in Italy. In this experiment, the ^{71}Ga target is used in the form of concentrated gallium chloride ($\text{GaCl}_3\text{-HCl}$) solution with a weight of 100 tons, which includes 30.3 tons of gallium. The ^{71}Ge atom produced by an incident solar neutrino forms the volatile molecule GeCl_4 . A measured amount of inactive Ge carrier atoms, which also form GeCl_4 , is added at the beginning of a run to provide a sufficiently large sample for extraction so that the efficiency can be determined experimentally after each run. At the end of an exposure, the GeCl_4 is swept out of the solution by bubbling air or nitrogen gas through the tank. The gas stream is then passed through two gas scrubbers where the GeCl_4 is absorbed in water. The GeCl_4 is then extracted into CCl_4 , back-extracted into tritium-free water, and finally reduced to ~ 0.1 to 1 cm^3 of the gas germane, GeH_4 , by means of NaBH_4 . The GeH_4 , together with xenon, is introduced into a small proportional counter, where the number of ^{71}Ge atoms is determined by observing their radioactive decay. The small proportional counter is sensitive to both of K-peak and L-peak electrons.

The SAGE experiment started in 1990, and its detector is located 4715m water equivalent underground at the Baksan Neutrino observatory in Russia. In this experiment, as the target, 30t(till July 1991) or 60t(after July 1991) of gallium metal is used. As Ga metal melts at 29.8°C , permitting the liquid(which has a density of 6.0 g cm^{-3}) to be mixed with dilute hydrochloric acid. To remove germanium, hydrogen peroxide is added to the dilute acid and the entire mass is mixed vigorously. Upon mixing, the metallic gallium is dispersed in the acid in the form of small globules each coated with an oxide layer. The mass appears as a black mud. If the concentration of HCl is chosen correctly, a few minutes of vigorous stirring causes the oxide coating of the globules of metal to dissolve and a clean metallic layer to form with the acid on top. The reaction is carried out in a Teflon vat provided with a mechanical mixer. In the full scale experiment, 10 identical reactor vessels will contain the gallium. The dilute acid from the 10 units will be combined and, after the solution is concentrated by evaporation, concentrated acid will be added. The germanium, which is in the concentrated acid, can be removed by purging with gas and collected in a water scrubber using a procedure similar to that described above for the GALLEX experiment. The germanium chloride collected is subsequently converted to germane by reduction with sodium borohydride. Since very large volumes of hydrochloric acid are used in this method, a procedure was developed to recover the hydrochloric acid and reuse it. After extraction of ^{71}Ge , amount of ^{71}Ge is determined by counting. The proportional counter used in the SAGE experiment can measure only the K-peak.

There are 3 main differences between these two ^{71}Ga experiments; (1) form of gallium target($\text{GaCl}_3\text{-HCl}$, or metal), (2) mass of target, and (3) performance of the proportional counter. Advantages of metal target are (1)less sensitive to the background reaction caused by radioactive impurities and (2) a smaller volume which reduces some other background because of its large density, and provides a larger interaction rate in a laboratory calibration experiment (for ex-

ample, with ^{51}Cr). The main disadvantage of the metal target is that each time the germanium is separated it is necessary to add fresh chemical reagents. One must therefore control strictly the germanium impurities. The greater complexity of the initial extraction procedure makes it more difficult to demonstrate that the chemical processing is free of unknown systematic effects.

The initial expected production rate in the gallium experiments is 137_{-7}^{+8} SNU from SSM of BP95[9]. The contribution from individual neutrino sources are summarized in Table.2.4. As seen in this table, approximately 50 % are the pp neutrinos in the gallium experiment.

The measured solar neutrino flux by each experiment is

$$\text{GALLEX}[15] : 69.7 \pm 6.7(\text{stat.}) \begin{matrix} +3.9 \\ -4.5 \end{matrix} (\text{syst.}) \text{ SNU}, \quad (2.15)$$

$$\text{SAGE}[16] : 69 \pm 10(\text{stat.}) \begin{matrix} +5 \\ -7 \end{matrix} (\text{syst.}) \text{ SNU}. \quad (2.16)$$

The ratio of data to SSM prediction(BP95[9]) is

$$\text{GALLEX} : 0.509 \pm 0.049(\text{stat.}) \begin{matrix} +0.028 \\ -0.033 \end{matrix} (\text{syst.}) \quad (2.17)$$

$$\text{SAGE} : 0.504 \pm 0.073(\text{stat.}) \begin{matrix} +0.036 \\ -0.051 \end{matrix} (\text{syst.}) \quad (2.18)$$

Both results are significantly smaller than the expected value from SSM. The deficit in the solar neutrino flux is also confirmed in pp neutrinos.

The time variation of the solar neutrino flux measured by GALLEX and SAGE is shown in Fig.2.10 and 2.9. Both results have very large statistical errors. By the statistical analysis of time variation, however, GALLEX came to a conclusion that there were observed no evidence for any statistically significant time dependence of the observed ^{71}Ge production rate[15].

2.3 Possible solutions to the solar neutrino problem

Possible solutions to the solar neutrino problem(solar neutrino deficit) are classified into 2 categories: One is an astrophysical solution and the other is related to the intrinsic properties of neutrinos, especially neutrino oscillations. In this section, both of these solutions are explained in detail.

2.3.1 Astrophysical solutions

One of the methods to solve the deficit in the observed solar neutrino flux is the modification of SSM. As described in Section.2.1, the ^8B solar neutrino flux is very sensitive to the input parameters of SSM, the temperature of the solar core and S -factors. Especially, S_{17} is directly proportional to the ^8B solar neutrino flux. Changing this parameter, some other solar models can be constructed, and the result is summarized in Table.2.5.

DS94[13] predicts the lowest ^8B solar neutrino flux which is consistent with the result of Kamiokande-II+III result($2.80 \pm 0.19 \pm 0.33 (\times 10^6)[\text{cm}^{-2}\text{sec}^{-1}]$). It is, however, still inconsistent with the Homestake result($2.55 \pm 0.14 \pm 0.14$ SNU)

Then, recently, N.Hata and P.Langacker[18] compared the results from the solar neutrino experiments with several modified SSMs. The result of their comparison is shown in Fig.2.11. In

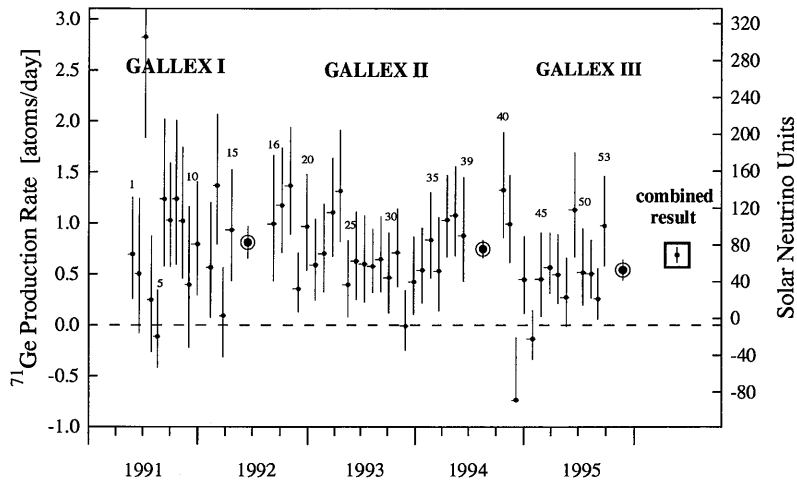


Figure 2.9: Solar neutrino flux measured by GALLEX from 1991 to 1995[15]. The entire data-taking period is divided into 3 periods called GALLEX I (labels 1~15), II(labels 16~39), and III(labels 40~53). Small filled circle corresponds to each run and larger filled circle with open one stands for the average flux for each period. The label “combined” indicates the global mean value for the entire experimental period. Error bars are $\pm 1\sigma$, statistical only.

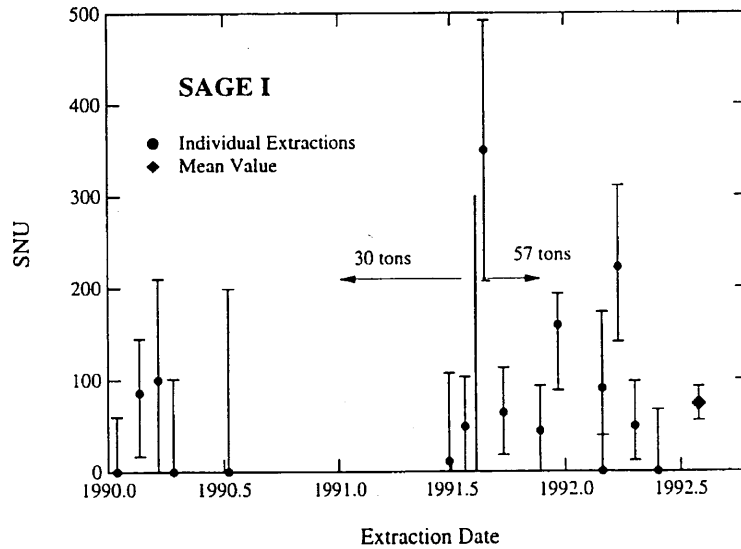


Figure 2.10: Solar neutrino flux in unit of SNU measured by SAGE from 1990 to 1995[16]

Model	$S_{17}(0)$ ($eV \cdot b$)	expected for ^{37}Cl [SNU]	^8B neutrino flux [$\text{cm}^{-2}\text{s}^{-1}$]
BP92[8]	22.4	8.0 ± 3.0	$5.69(1 \pm 0.43) \times 10^6$
TL93[12]	24.3	6.4 ± 1.4	$(4.44 \pm 1.1) \times 10^6$
DS94[13]	17	4.2 ± 0.5	$(2.77 \pm 0.35) \times 10^6$
BP95[9]	22.4	$9.3^{+1.2}_{-1.4}$	$(6.62^{+0.93}_{-1.12}) \times 10^6$

Table 2.5: S-factors employed by different SSMs and the resultant solar neutrino fluxes

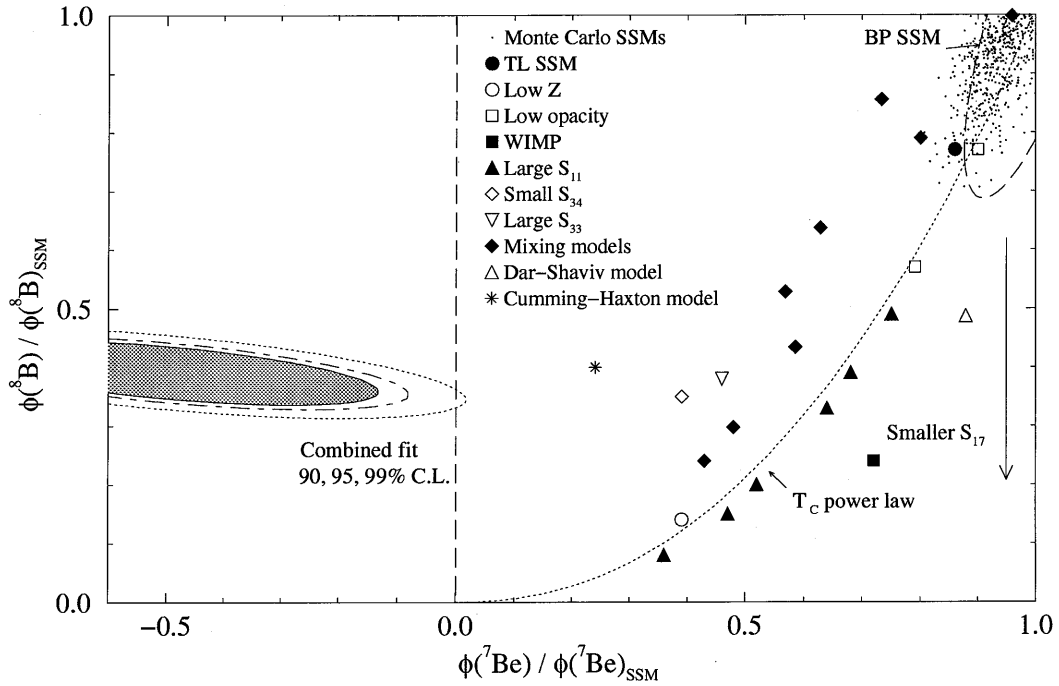


Figure 2.11: The constraints from the combined Cl, Ga and Čerenkov experiments[18]. The hatched area corresponds to the allowed region at 90% C.L. and the allowed region contours at 95% and 99% C.L. are also given by the dot-dashed and the dotted line, respectively. Also shown are the Bahcall-Pinsonneault SSM (BP SSM) region at 90% C.L.[9], the core temperature power law (T_C power law) and standard and nonstandard solar models[17]. A smaller S_{17} cross section moves the solar model predictions to a smaller ^8B solar neutrino flux as indicated by the arrow.

this comparison, they allowed the ${}^7\text{Be}$ flux to be negative. The result implies that no modified SSM is consistent with the experimental results. The experimental results suppress the ${}^7\text{Be}$ neutrino flux excessively. Therefore, it is difficult to explain the solar neutrino problem by uncertainties in SSM.

2.3.2 Neutrino Oscillations

In the simplest form of the standard electroweak model, neutrinos are assumed to be purely massless particles, while there is no underlying physical reason for this assumption. In this section, the flavor oscillations of massive neutrinos in matter as well as in vacuum are described. The details are described, for example in Ref.[1].

Vacuum Oscillations

In general, neutrino flavor eigenstates ν_e , ν_μ and ν_τ are not necessarily the same as the mass eigenstates, ν_1 , ν_2 and ν_3 . If they are different, the neutrino flavor eigenstates are described by superposition of different neutrino mass eigenstates. Here, to simplify the problem, the discussion about the mixing is restricted to the two flavor mixing case.

The mixture of the mass eigenstates is expressed by

$$\begin{pmatrix} \nu_e \\ \nu_\mu \end{pmatrix} = \begin{pmatrix} \cos\theta & \sin\theta \\ -\sin\theta & \cos\theta \end{pmatrix} \begin{pmatrix} \nu_1 \\ \nu_2 \end{pmatrix} \equiv \mathbf{U} \begin{pmatrix} \nu_1 \\ \nu_2 \end{pmatrix}, \quad (2.19)$$

where θ is the mixing angle in vacuum, and ν_1 and ν_2 are the mass eigenstates of the neutrinos, with a mass of m_1 and m_2 , respectively. The time evolution of ν_1 and ν_2 obeys the Schrödinger equation:

$$i \frac{d}{dt} \begin{pmatrix} \nu_1(t) \\ \nu_2(t) \end{pmatrix} = \begin{pmatrix} E_1 & 0 \\ 0 & E_2 \end{pmatrix} \begin{pmatrix} \nu_1(t) \\ \nu_2(t) \end{pmatrix}, \quad (2.20)$$

where E_i is the energy of ν_i ($i = 1, 2$). The solution of this equation is

$$\begin{pmatrix} \nu_1(t) \\ \nu_2(t) \end{pmatrix} = \begin{pmatrix} e^{-iE_1 t} & 0 \\ 0 & e^{-iE_2 t} \end{pmatrix} \begin{pmatrix} \nu_1(0) \\ \nu_2(0) \end{pmatrix}, \quad (2.21)$$

Hence, the flavor eigenstate is written as

$$\begin{pmatrix} \nu_e(t) \\ \nu_\mu(t) \end{pmatrix} = \mathbf{U} \begin{pmatrix} e^{-iE_1 t} & 0 \\ 0 & e^{-iE_2 t} \end{pmatrix} \mathbf{U}^{-1} \begin{pmatrix} \nu_e(0) \\ \nu_\mu(0) \end{pmatrix}, \quad (2.22)$$

The mass of each neutrino is assumed to be small compared with E_i , and E_i can be approximated by

$$E_i = \sqrt{p^2 + m_i^2} \cong E + \frac{m_i^2}{2E} \quad (i = 1, 2) \quad (2.23)$$

where p is the neutrino momentum, and $p \cong E$. Then Eq.2.22 becomes

$$\begin{pmatrix} \nu_e(t) \\ \nu_\mu(t) \end{pmatrix} = \begin{pmatrix} \cos \frac{\Delta m^2}{4E} t + i \cos 2\theta \sin \frac{\Delta m^2}{4E} t & -i \sin 2\theta \sin \frac{\Delta m^2}{4E} t \\ -i \sin 2\theta \sin \frac{\Delta m^2}{4E} t & \cos \frac{\Delta m^2}{4E} t - i \cos 2\theta \sin \frac{\Delta m^2}{4E} t \end{pmatrix} \begin{pmatrix} \nu_e(0) \\ \nu_\mu(0) \end{pmatrix}, \quad (2.24)$$

where $\Delta m^2 \equiv m_2^2 - m_1^2$ (when $m_2 > m_1$). If an electron neutrino is produced at $t = 0$, the probability of detecting this neutrino in the same flavor state at $t = t$ can be written by

$$P(\nu_e \rightarrow \nu_e) = 1 - \sin^2 2\theta \sin^2 \frac{\pi L}{L_\nu}, \quad (2.25)$$

where L is the neutrino propagation length at $t = t$, L_ν is the oscillation length in vacuum defined by

$$L_\nu \equiv \frac{4\pi E}{\Delta m^2} = 2.48 \left(\frac{E}{\text{MeV}} \right) \left(\frac{\text{eV}^2}{\Delta m^2} \right) [\text{m}], \quad (2.26)$$

A number of experiments to search for the neutrino oscillation have been carried out using reactors and accelerators. An experiment usually aims at being sensitive to as small a Δm^2 as possible. Since Δm^2 appears in the oscillation phase in a form of $\Delta m^2 \cdot L/E$, the best one can do is to use lower energy neutrinos which travel a longer distance. A typical sensitivity to Δm attainable with artificial neutrino source is down to $\sim 10^{-2} \text{ eV}^2$.

As seen in Eq.2.26, neutrino oscillations can be probed by means of the solar neutrinos down to $\Delta m^2 \approx 10^{-10} \sim 10^{-11} \text{ eV}^2$, where the vacuum oscillation length is equivalent to the distance between the Sun and the Earth ($1.5 \times 10^8 \text{ km}$).

Neutrino Oscillations in matter (MSW effect)

When a neutrino propagates in matter, it generally feels potential energy caused by interaction with matter. Especially when both electron and muon neutrinos are considered, only electron neutrinos undergo an additional potential by the charged current interaction with electrons in matter (see Fig.2.12). This effect was first proposed by S.P.Mikheyev and A.Yu.Smirnov

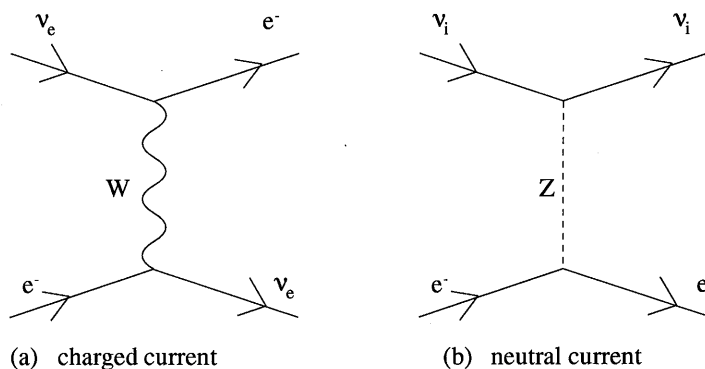


Figure 2.12: Feynman diagrams of the reaction $\nu_e + e^- \rightarrow e^- + \nu_e$. (a) charged current and (b) neutral current. reaction (b) is forgiven for each flavor of neutrino, while reaction (a) is only forgiven for electron neutrinos.

based on the theory advocated by L.Wolfenstein, abbreviated as the MSW effect[19][20].

In matter, time evolution of the flavor eigenstates is written as

$$i \frac{d}{dt} \begin{pmatrix} \nu_e(t) \\ \nu_\mu(t) \end{pmatrix} = \left[\mathbf{U} \begin{pmatrix} E_1 & 0 \\ 0 & E_2 \end{pmatrix} \mathbf{U}^{-1} + \begin{pmatrix} V_e & 0 \\ 0 & 0 \end{pmatrix} \right] \begin{pmatrix} \nu_e(t) \\ \nu_\mu(t) \end{pmatrix}, \quad (2.27)$$

where V_0 is an arbitrary potential energy:

$$V_0 = \sqrt{2} \mathcal{M}_0 \mathcal{M}_1 \quad (2.27)$$

where \mathcal{M}_0 is the Fermi coupling constant, and \mathcal{M}_1 is an electron number density. Choosing common phases, Eq.(27) reduces to

$$\begin{aligned} \frac{d}{dz} \begin{pmatrix} \nu_e(z) \\ \nu_\mu(z) \end{pmatrix} &= \begin{pmatrix} -\frac{\Delta m^2 \cos 2\theta}{4E} - \frac{1}{L_e} & \frac{\Delta m^2 \sin 2\theta}{4E} \\ \frac{\Delta m^2 \sin 2\theta}{4E} & \frac{\Delta m^2 \cos 2\theta}{4E} - \frac{1}{L_e} \end{pmatrix} \begin{pmatrix} \nu_e(z) \\ \nu_\mu(z) \end{pmatrix} \\ &= \frac{1}{L_e} \begin{pmatrix} -\cos 2\theta + \frac{1}{2} & \sin 2\theta \\ \sin 2\theta & \cos 2\theta - \frac{1}{2} \end{pmatrix} \begin{pmatrix} \nu_e(z) \\ \nu_\mu(z) \end{pmatrix}, \end{aligned} \quad (2.28)$$

where L_e is the neutrino-electron interaction length:

$$L_e = \frac{N_A \sigma_{\nu e}}{N_e \sigma_{\nu e}} = \frac{2\pi}{N_e}. \quad (2.29)$$

Assuming a constant electron density, the mixing matrix in matter which is analogous to the vacuum oscillation case can be expressed by:

$$\begin{pmatrix} \nu_e^M \\ \nu_\mu^M \end{pmatrix} = \begin{pmatrix} \cos \theta_m & -\sin \theta_m \\ \sin \theta_m & \cos \theta_m \end{pmatrix} \begin{pmatrix} \nu_e \\ \nu_\mu \end{pmatrix}, \quad (2.30)$$

where ν_i^M ($i = e, \mu$) is the effective mass eigenstate, and θ_m is the mixing angle in matter which is defined by:

$$\tan 2\theta_m = \frac{\sin 2\theta}{\cos 2\theta - \frac{1}{2}} \quad (2.31)$$

where $\theta_m > \theta_v$. The mixing angle in matter becomes undefined at $\cos 2\theta = \frac{1}{2}$ and is often referred to as the "resonance condition". The resonance condition can be written in another way by the electron density:

$$N_{e, \text{res}} = \frac{2\Delta m^2 \cos 2\theta}{2\sqrt{2} \sin 2\theta}. \quad (2.32)$$

If the variation in time of the electron density is relatively small, an adiabatic solution is valid. Namely, the solution is obtained simply by relaxing the assumption of the constant solar density. Neutrinos produced in the core region of the Sun fly toward the surface (of the Sun). Their average production energies $\langle E \rangle$ are close to certain values $\langle E_{\nu_i} \rangle$ for each i .

$$\langle E_{\nu_i} \rangle = E_0 \cos 2\theta \left(\frac{\Delta m^2}{4E_0^2 - \Delta m^2} \right) M_e c^2, \quad (2.33)$$

where the lower eigenstate ν_1 is essentially the heavier mass eigenstate ν_2 . After passing through the resonance region, ν_1 is almost the same as ν_μ . Hence, the produced neutrino is observed as ν_μ . This is the case if the change of the electron density is slow enough around the resonance to keep the mass eigenstate adiabatically ($|\frac{d}{dz} \frac{\Delta m^2}{4E^2}| \ll \frac{1}{L_e} \cos 2\theta$). This effect is illustrated in Fig. 2.13.

In a region where the electron density variation is too rapid around the resonance to keep the mass eigenstate ($|\frac{d}{dz} \frac{\Delta m^2}{4E^2}| \gg \frac{1}{L_e} \cos 2\theta$), however, the adiabatic solution is no longer appropriate. Presumably, the MSW is nonresonantly perturbed for a concrete. The survival probability

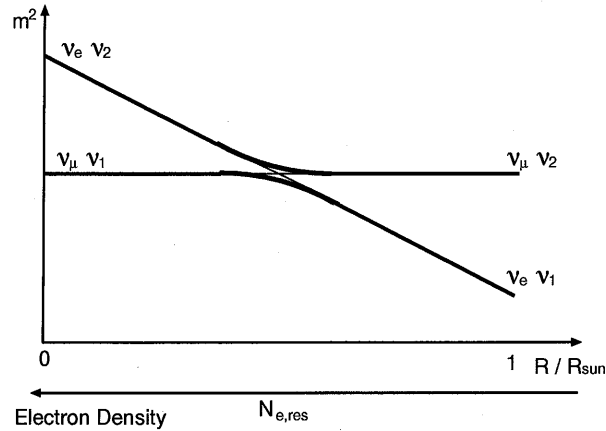


Figure 2.13: The MSW effect (adiabatic change) in the Sun. While neutrino propagates in the Sun, the electron density (N_e) decreases and the resonance condition is satisfied ($N_e = N_{e,res}$). Under this condition, the flavor conversion occurs. The vertical axis is the effective mass of neutrinos in the Sun. The horizontal axis is the distance from the center of the Sun in unit of the solar radius.

for electron neutrinos which are created at a density larger than that in the resonant region is solved as

$$P(\nu_e \rightarrow \nu_e) = \frac{1}{2} + \left(\frac{1}{2} - P_{jump} \right) \cos 2\theta_m \cos 2\theta \quad (2.35)$$

The probability of the level jumping, P_{jump} , is obtained by using an approximation developed by L.D.Landau[22], and C.Zener[23], in which the electron density varies linearly in the region near the resonance. Under this condition, P_{jump} is

$$P_{jump} = \exp \left[\frac{-\pi \Delta m^2 \sin^2 2\theta}{4E \cos 2\theta} \left(\frac{N_e}{|dN_e/dr|} \right)_{res} \right], \quad N_e > N_{e,res} \quad (2.36)$$

If the following condition is satisfied, the jump does not occur.

$$E \leq \frac{\Delta m^2 \sin^2 2\theta}{\cos 2\theta} \left(\frac{N_e}{|dN_e/dr|} \right)_{res} \quad (2.37)$$

An example of the MSW effect in the Sun at $\sin^2 2\theta = 1.0 \times 10^{-3}$ and $\frac{E}{\Delta m^2} = 6.0 \times 10^5$ MeV/eV² is shown in Fig.2.14.

Furthermore, when solar neutrinos are detected at the Earth, the MSW effect in the Earth must be considered. The electron density profile in the Earth[21] is shown in Fig.2.15. The electron density profile in the Earth is not as smooth as that in the Sun. Hence, $P(\nu_e \rightarrow \nu_e)$ depends on neutrino path. In Fig.2.16, $P(\nu_e \rightarrow \nu_e)$ at Super-Kamiokande with matter oscillation at $\sin^2 2\theta = 0.1$ and with $\cos \delta_{sun} = 0.5, 1.0$ or with no MSW effect in the Earth are shown. Here, the definition of $\cos \delta_{sun}$ is shown in Fig.2.17. Hence, by investigating the difference in the solar neutrino flux between the daytime and the nighttime, one can probe the MSW effect independent of SSMS.

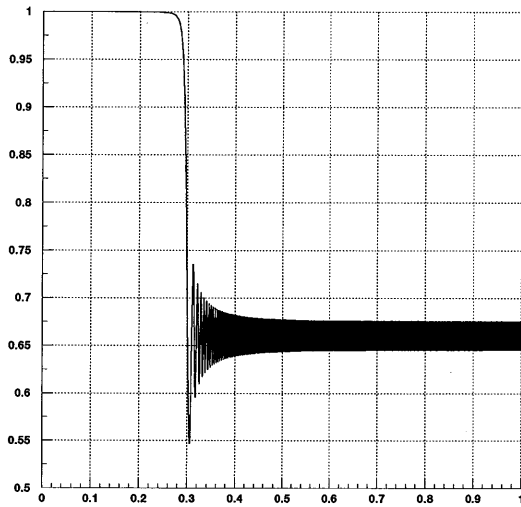


Figure 2.14: $P(\nu_e \rightarrow \nu_e)$ in the Sun at $\sin^2 2\theta = 1.0 \times 10^{-3}$ and $\frac{E}{\Delta m^2} = 6.0 \times 10^5$ MeV/eV². The horizontal axis is the solar radius (R/R_{sun}), and the vertical axis is the survival probability of electron neutrinos.

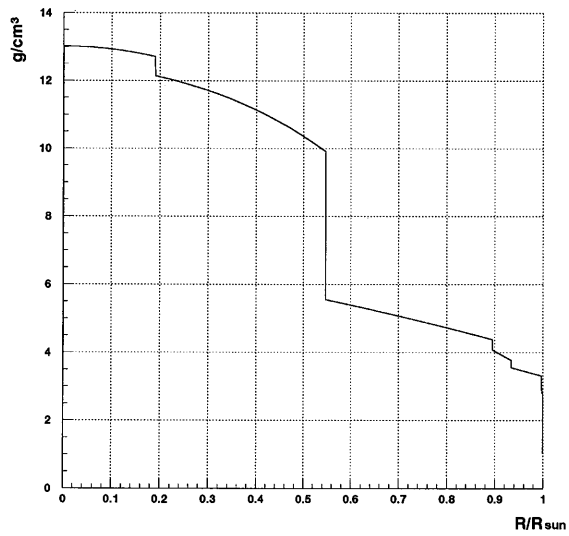


Figure 2.15: The density profile in the Earth[21]

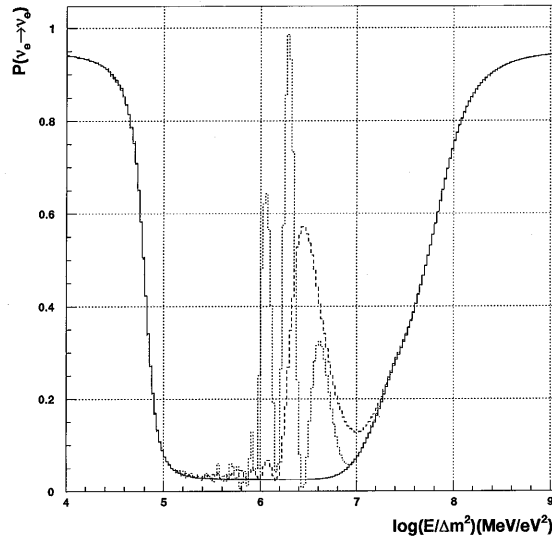


Figure 2.16: $P(\nu_e \rightarrow \nu_e)$ at Super-Kamiokande with matter oscillation at $\sin^2 2\theta = 0.1$ with $\cos \delta_{sun} = 0.5$ (dashed), 1.0 (dotted) and no MSW effect in the Earth effect(solid).

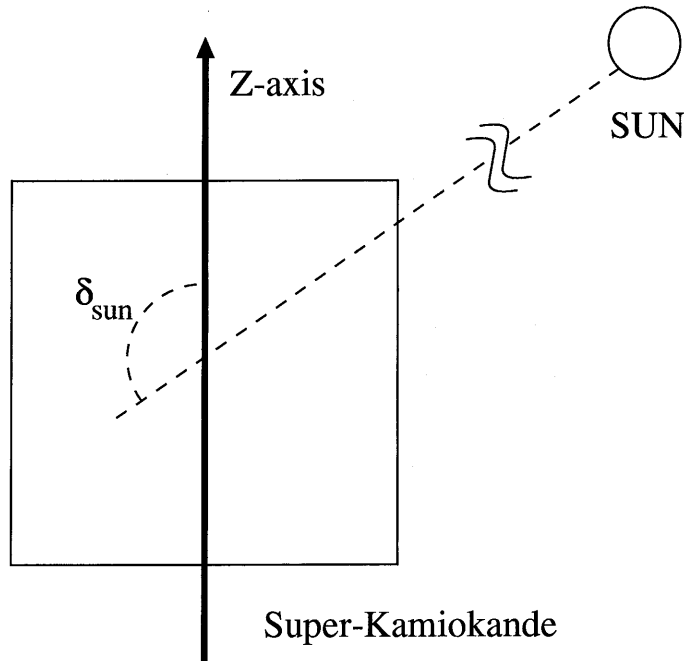


Figure 2.17: Definition of δ_{sun} . δ_{sun} is the relative angle between the direction to the Sun and the z-axis of the detector.

2.3.3 Allowed region of the MSW effect

Combining the available solar neutrino data from Homestake, Kamiokande-II+III, GALLEX, and SAGE, the MSW effects has been studied[18]. As shown in Fig.2.18, there exist 2 allowed regions on the $(\sin^2 2\theta, \Delta m^2)$ plane. The region which sits around $\Delta m^2 \approx 10^{-5} eV^2$ and $\sin^2 2\theta \approx$

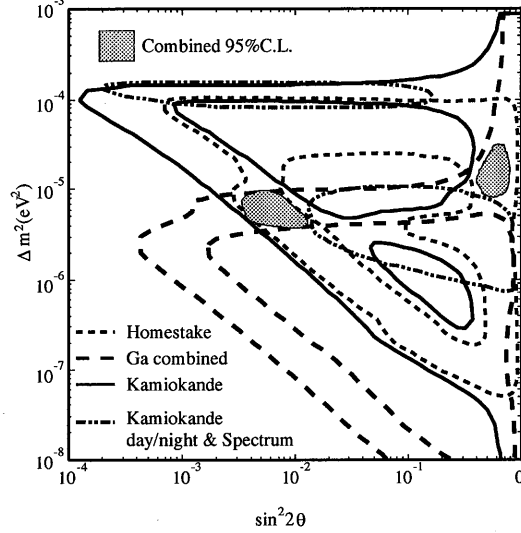


Figure 2.18: Allowed region at 95% C.L. on the $(\sin^2 2\theta, \Delta m^2)$ plane. The MSW effect is taken into account. Combination of the current solar neutrino experiments leaves just two hatched areas.

0.6 is called the large-angle solution where all the solar neutrinos are uniformly suppressed in all the energy region. The region which sits around $\Delta m^2 \approx 10^{-5} eV^2$ and $\sin^2 2\theta \approx 0.01$ is called the non-adiabatic solution where lower energy neutrinos are preferentially converted.

2.4 Solar neutrino interaction in water

The Super-Kamiokande detector detects Čerenkov photons emitted by a recoil electron scattered with a 8B solar neutrino.

Therefore, the measurement of 8B solar neutrinos at Super-Kamiokande is based on the elastic scattering of a neutrino with an orbital electron in water;

$$\nu + e \rightarrow \nu + e. \quad (2.38)$$

The cross section of neutrino-electron elastic scattering is given by

$$\frac{d\sigma}{dT_e} = \frac{G_F^2 m_e}{2\pi} \left[A_0 + B_0 \left(1 - \frac{T_e}{E_\nu}\right)^2 + C_0 \frac{m_e T_e}{E_\nu^2} \right] [24] \quad (2.39)$$

where T_e is the kinetic energy of the recoil electron, E_ν is the incident neutrino energy, G_F (Fermi coupling constant) = $1.16639 \times 10^{-5} \text{ GeV}^{-2}$, and m_e is the electron rest mass; $m_e = 0.511 \text{ MeV}/c^2$.

Numerical value of the constant outside the square bracket in Eq.2.39 is

$$\frac{G_F^2 m_e}{2\pi} = 4.31 \times 10^{-45} \quad (\text{cm}^2/\text{MeV}) \quad (2.40)$$

Parameters A_0 , B_0 , and C_0 are defined by

$$A_0 = (g_V + g_A)^2, B_0 = (g_V - g_A)^2, C_0 = (g_A^2 - g_V^2) \quad (2.41)$$

$$g_V = 2 \sin^2 \theta_W + \frac{1}{2}, \quad g_A = +\frac{1}{2} \quad \text{for } \nu_e \quad (2.42)$$

$$g_V = 2 \sin^2 \theta_W - \frac{1}{2}, \quad g_A = -\frac{1}{2} \quad \text{for } \nu_\mu, \nu_\tau [24] \quad (2.43)$$

where θ_W is the Weinberg angle = 0.2317[26]. Then, the total cross section is obtained by integrating the differential cross section(see Eq.(2.39)) from 0 to T_{max} ,

$$\sigma_{total} = \int_0^{T_{max}} \frac{d\sigma}{dT_e} dT_e \quad (2.44)$$

$$= \frac{G_F^2 m_e}{2\pi} \left[A_0 T_{max} + \frac{B_0 \cdot E_\nu}{3} \left\{ 1 - \left(1 - \frac{T_{max}}{E_\nu} \right)^3 \right\} + \frac{C_0}{2} \frac{m_e}{E_\nu} \frac{T_{max}^2}{E_\nu} \right], \quad (2.45)$$

where T_{max} is the maximum value of the electron kinetic energy given by a kinematical limit as follows,

$$T_{max} = \frac{E_\nu}{1 + \frac{m_e}{2E_\nu}} \quad (2.46)$$

Subsequently, the radiative corrections are taken into account[26]. The Feynman diagrams for the one-loop electroweak(see Fig.2.19), and QCD(see Fig.2.20) corrections, respectively. After

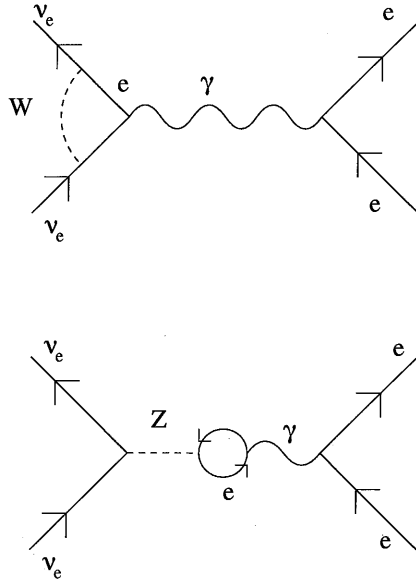


Figure 2.19: Feynman diagrams of one-loop electroweak radiative corrections

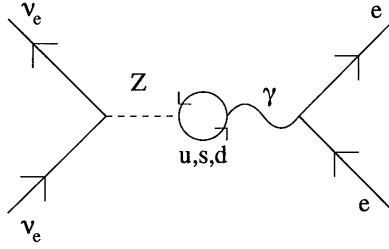


Figure 2.20: Feynman diagram of one-loop QCD radiative corrections

these radiative corrections, the $\nu_e + e^- \rightarrow \nu_e + e^-$ scattering cross section decreases by 2%. The shape of the recoil electron spectrum produced by ${}^8\text{B}$ solar neutrinos changes and is reduced by approximately 4% at the highest electron energies. In the case of $\nu_\mu + e^- \rightarrow \nu_\mu + e^-$ scattering, only the neutral-current radiative correction is taken into considerations. The resultant total neutrino cross sections are shown in Fig.2.21.

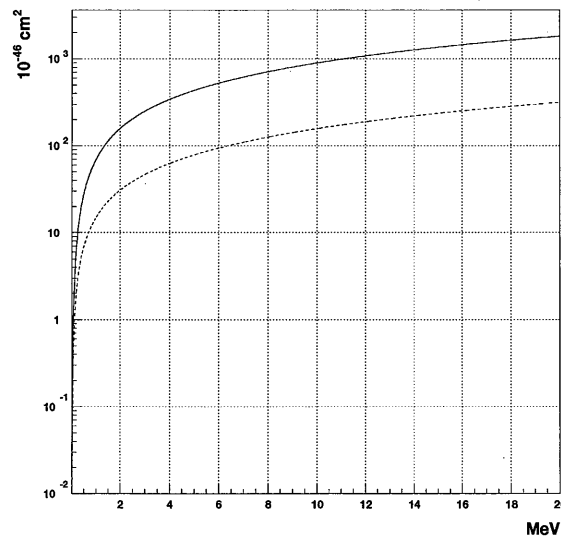


Figure 2.21: Total cross sections for $\nu - e$ scatterings. The horizontal axis is the incident neutrino energy in unit of MeV and the vertical axis is total cross section in unit of 10^{-46} cm^2 . The solid line corresponds to $\nu_e - e$ cross section, while the dashed line corresponds to $\nu_\mu - e$ cross section.

The energy of a recoil electron reflects the energy of its incident neutrino. Therefore, one can measure indirectly the energy distribution of incident neutrinos by means of the recoil electron energy spectrum. The energy spectrum of the recoil electrons is given by

$$F(T_e)dT_e = \left[\int_0^{E_{\nu, \max}} \phi(E_\nu) \frac{d\sigma}{dT_e} dE_\nu \right] dT_e \quad (2.47)$$

shown in Fig.2.22, where $\phi(E_\nu)$ is the ^8B solar neutrino spectrum and $E_{\nu,max}$ is the end point energy of the neutrinos.

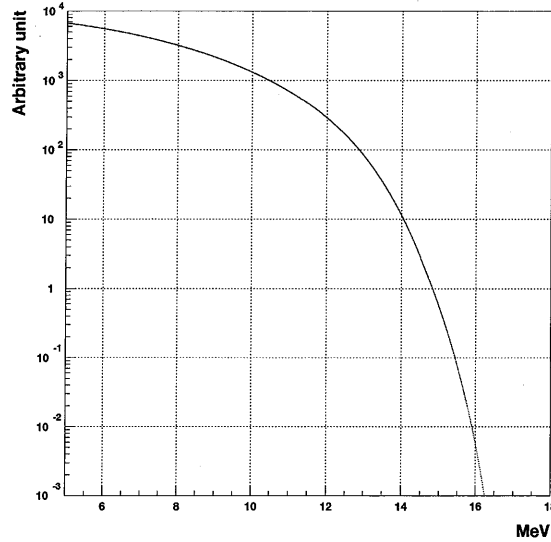


Figure 2.22: Energy spectrum of the recoil electrons produced by ^8B solar neutrinos with electron energies greater than 5 MeV. The horizontal axis is the total energy of the recoil electron in unit of MeV, and the vertical axis is an arbitrary unit.

The angle between the direction of the recoil electron and that of the incident neutrino is given by

$$\cos \vartheta = \frac{1 + \frac{m_e}{E_\nu}}{\sqrt{1 + \frac{2m_e}{T_e}}} \quad (2.48)$$

The kinematical limit of the scattering angle is :

$$\vartheta^2 \leq \frac{2m_e}{T_e} \quad (E_\nu \rightarrow \infty) \quad (2.49)$$

The angular resolution, however, is limited by multiple Coulomb scatterings of the recoil electrons in water. By means of the strong correlation between the reconstructed direction of recoil electron and the solar direction, one can separate electrons of solar ν origin from background.

Then, the unique advantages of Super-Kamiokande are summarized as follow;

1. one can get exact arrival time information of the incident neutrino
2. the recoil electron preserves the direction of the incident neutrino
3. the energy distribution of the recoil electrons reflects the energy spectrum of the incident neutrinos.

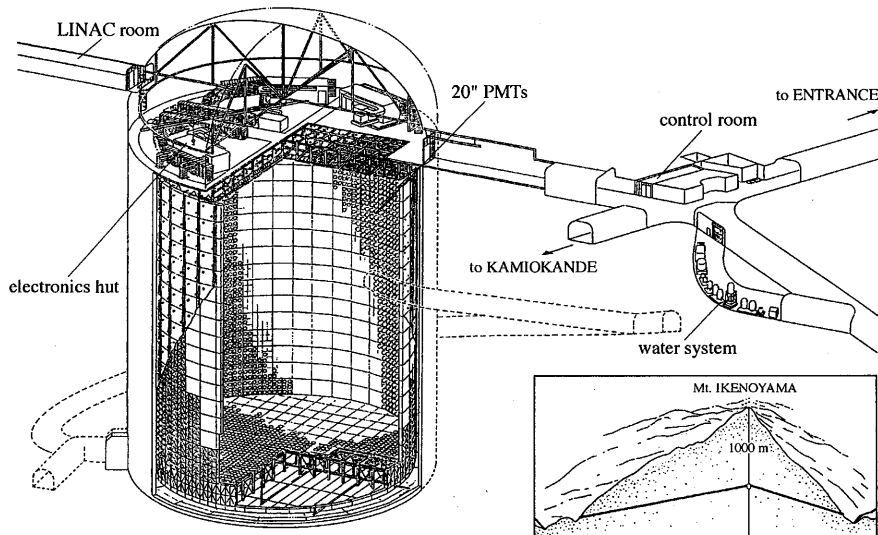
Hence, one can measure not only flux but also other important experimental information; the energy spectrum and time dependence of the ^8B solar neutrino flux.

Chapter 3

Super-Kamiokande Detector

Super-Kamiokande detector is an imaging water Čerenkov detector, which detects Čerenkov light photons emitted by a charged particle.

The detector consists of a cylindrical stainless steel tank, about 50,000t of pure water, water and air purification systems, 11,146 20-inch(50.8-cm)-in-diameter PMTs¹ and 1,885 8-inch(20.32-cm)-in-diameter PMTs, and electronics system. Schematic view of the detector is shown in Fig.3.1.



SUPERKAMIOKANDE INSTITUTE FOR COSMIC RAY RESEARCH UNIVERSITY OF TOKYO

NIKKEN SEKKEI

Figure 3.1: Overview of Super-Kamiokande detector

The detector is located $36^{\circ}25'N(25^{\circ}8'N)$ in latitude, and $137^{\circ}18'E$ in longitude, about 1,000m underground (2,700m water equivalent) in Mt. Ikenoyama in Kamioka town, Gifu

¹PhotoMultiplier Tube

prefecture, Japan. The detector is constructed underground so as to reduce cosmic-ray muon by a factor of 10^5 .

In this chapter, the detection principle of the Super-Kamiokande detector and the detector components are described in detail.

3.1 Detection principle of solar neutrinos at Super-Kamiokande

The Super-Kamiokande detector detects Čerenkov light photons generated by a recoil electron scattered by a ^8B solar neutrino.

When a charged particle traverses in a medium having index of refraction n , with a velocity v larger than the light velocity in matter; $c' = c/n$, Čerenkov light is emitted. Čerenkov photons are emitted in a cone of half opening angle θ measured from the direction of the particle track, where

$$\cos \theta = \frac{1}{n\beta}, \quad (\beta = \frac{v}{c}) \quad (3.1)$$

In the relativistic limit, $v = c$, θ becomes 42° in water ($n = 1.334$ at 546.1nm).

The spectrum of Čerenkov light (see Fig.3.2) as a function of wavelength is calculated,

$$\frac{d^2 N}{dx d\lambda} = 2\pi\alpha \left(1 - \frac{1}{n^2\beta^2}\right) \frac{1}{\lambda^2} \quad (3.2)$$

where λ is the wavelength, x is the distance of the electron traversed and α is the fine structure constant. Integrating this equation over the visible wavelength, an electron typically emits approximately 340 photons/cm.

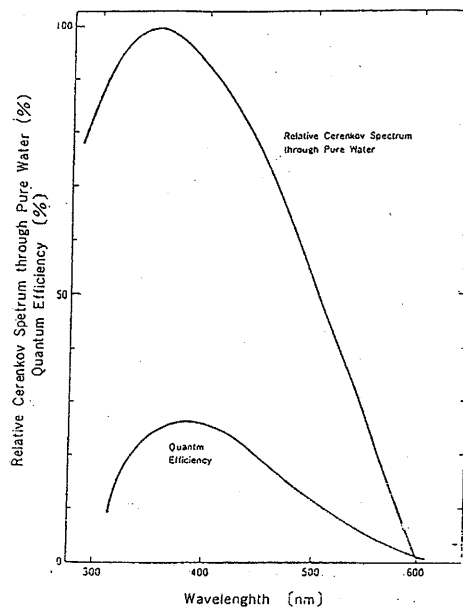


Figure 3.2: Relative Čerenkov light spectrum and spectral dependence of quantum efficiency of the inner-detector PMT.

3.2 Water Tank

The cylindrical water tank of Super-Kamiokande is filled with about 50,000t of pure water. The size is 3,930cm in diameter and 4,140cm in height. The tank is placed in a excavated cavity in the rock and is separated from the rock layer by stainless steel plates, except for the top part of the tank. On the top of the tank, there are 5 huts for the electronics system. (see Fig.3.3)

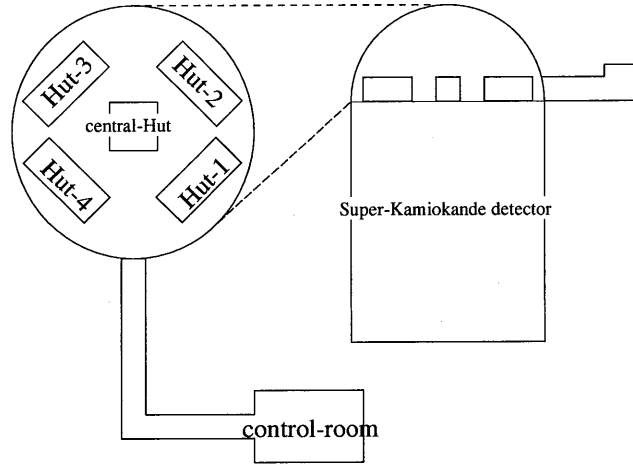


Figure 3.3: Electronics huts on the tank

The tank is divided into 3 parts; Inner detector(abbreviated as ID), Outer detector(abbreviated as OD) and photo-insensitive volume(see Fig.3.4). The inner detector is 1,690cm in

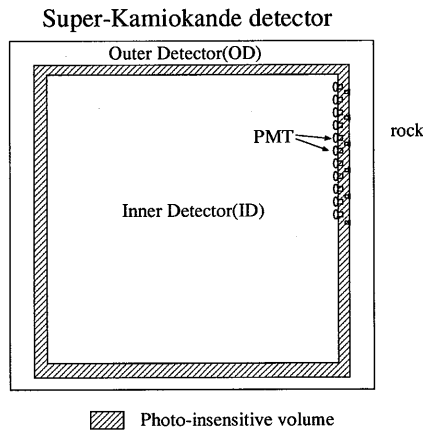


Figure 3.4: Schematic view of Super-Kamiokande tank.

radius and 3,620cm in height. The inner detector is filled with 32,000t of water. Thickness of the outer detector is 260cm in the barrel section and 275cm in the top and bottom sections. Thickness of the photo-insensitive volume is 55cm in the barrel region, and 45cm in the top and bottom regions. The inner detector and the photo-insensitive volume are optically isolated by plastic black sheets. The outer detector is covered with reflective tyvek sheets, reflectivity of

which is roughly 80%, to optically isolate from the other parts and to collect as many photons as possible. The main reasons why the detector is divided are to identify events which are caused by charged particles coming from outside of the detector (for example cosmic-ray muon event), and to provide a passive shield against γ -rays and neutrons from the rock surrounding the detector. Therefore, the outer detector usually serves as a veto counter.

All of the PMTs are mounted in the photo-insensitive volume (see Fig.3.5) on stainless steel frames. A stainless steel frame to support twelve inner-detector PMTs and two outer-detector

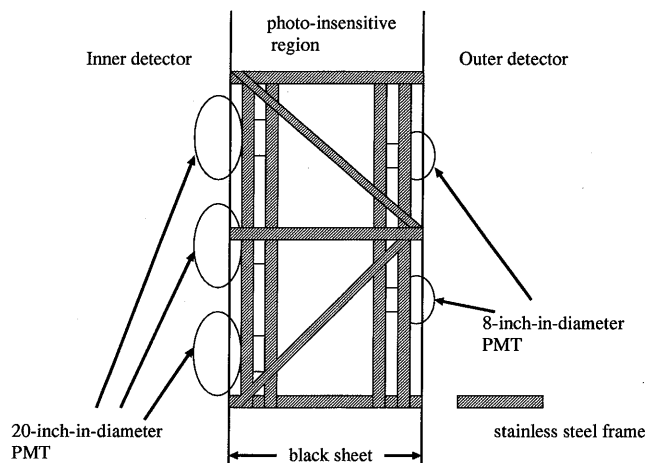


Figure 3.5: PMTs are mounting in the photo-insensitive volume on stainless steel frames.

PMTs constitute one Super-Module (see Fig.3.6). The Super-Modules are subsequently installed on the detector wall. A total of 11,146 20-inch(50.8-cm)-in-diameter PMTs are mounted on the inner detector: 7,650, 1,748 and 1,748 PMTs are allocated in the barrel, top and bottom sections, respectively. Two PMTs are arranged every 1 m^2 , and the resultant photosensitive coverage amounts to 40% of the total surface of the inner detector. Also a total of 1,885 8-inch(20.32-cm)-in-diameter PMTs are installed in the outer detector: 1,275, 302 and 308 PMTs are allocated in the barrel, top and bottom sections, respectively. Around each outer PMT, attached is a wavelength shifter plate to increase the photo-coverage(see Fig.3.7.)

3.3 Water system

3.3.1 Water purification system

In order to collect photons as efficiently as possible, the detector water must be kept as transparent as possible. The vertex position dependence of energy in an event should be minimize. Furthermore, radioactive elements dissolved in the water in the tank should be removed, as they are serious background sources against the solar neutrino signal. Especially, β decays of ^{214}Bi from ^{222}Rn in the water with an end point energy of 3.26MeV are troublesome, as the finite energy resolution of the detector smears them up to the analysis threshold.

In the Kamioka mine, natural clean underground water is available for free. The natural water is further purified before it is supplied into the tank. The water purification system consists of the following 7 elements as shown in Fig.3.8

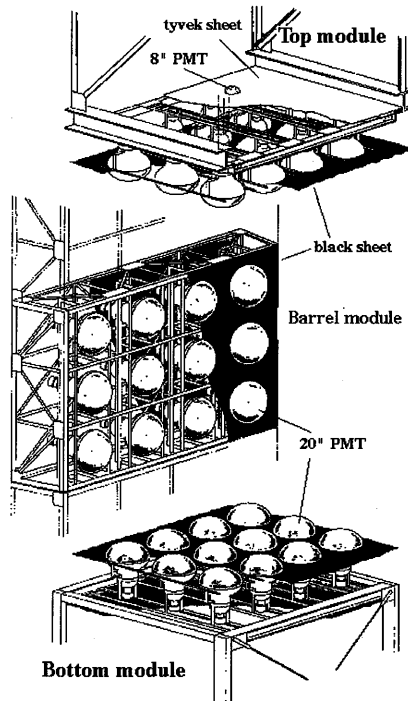


Figure 3.6: Super-Module

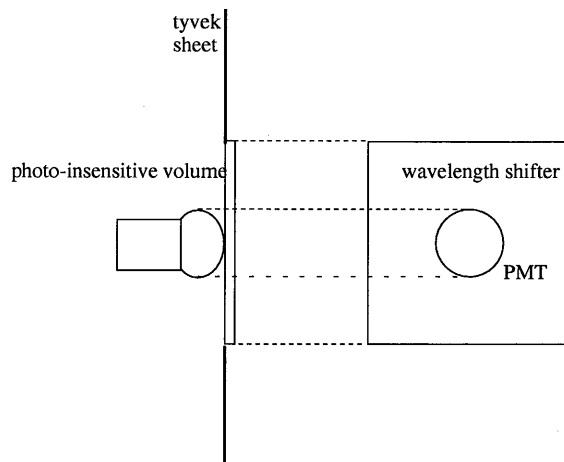


Figure 3.7: Outer-detector PMT and wavelength shifter

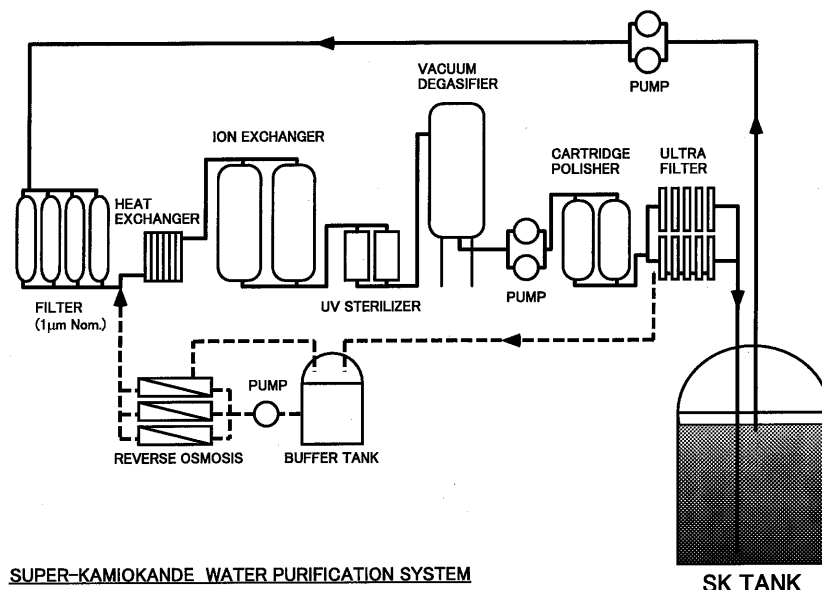


Figure 3.8: Water purification system

1. $1\mu\text{m}$ Filter

2. Heat exchanger

The water temperature constantly rises because of the heat generated from the water pumps and PMTs. To keep the water temperature less than 14°C that suppresses the proliferation of bacteria, the heat exchanger is needed.

3. Ion exchanger

To remove various metal ions in the water.

4. Ultra-Violet sterilizer

5. Vacuum degasifier

To remove gases in the water. It can remove about 99% of oxygen gas and 96% of radon gas contained in the fresh water.

6. Cartridge polisher

This is a high-performance ion exchanger.

7. sub- μm Ultra filter

To remove sub-micron dusts. After this filter, the ohmic resistance of the water is $18.20\text{ M}\Omega\text{cm}$ which is comparable to its chemical limit of $18.24\text{ M}\Omega\text{cm}$.

Going through these elements, the water is returned to the tank. As shown in Fig.3.8, the water is usually circulated through the purification system and the flow rate is about 50 tons/hour. This system keeps the water transparency at about 70m.

3.3.2 Radon free air

As radon gas is suspected to sneak into the water tank due to the incomplete airtightness of the top part of the detector, we pump up radon free air in the empty space in the water tank to pressurize it. Radon free air system is shown in Fig.3.9. The system is made up of the following components:

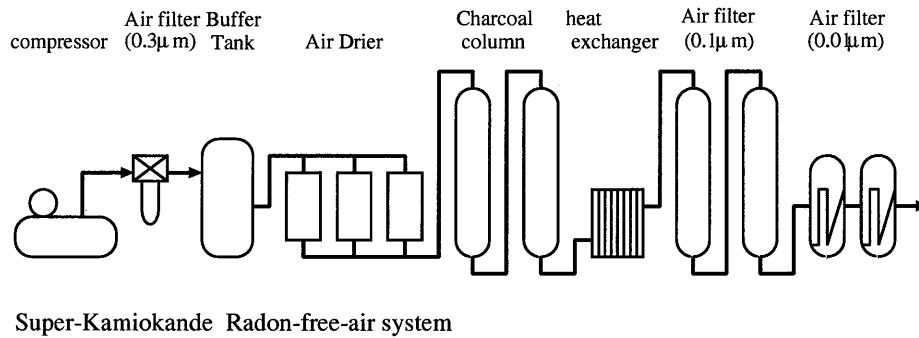


Figure 3.9: Radon free air system

1. Compressor

Fresh air is compressed to 7.0 ~ 8.5 atm.

2. 0.3 μm air filter

3. Buffer tank

4. Air drier

To remove the water contained in the gas, as radon gas in the wet air is not removed efficiently. This can remove CO_2 in the gas, too.

5. Charcoal column

To remove radon gas.

6. 0.1 μm and 0.01 μm air filters

With this system, the radon concentration in the air is reduced by a factor of 10^5 .

The Rn concentration in the Super-Kamiokande water went down gradually since the start of the experiment. After about 100 days, it became about $5\text{mBq}/\text{m}^3$ which is at 1/1000 level in Kamiokande-III, and now it is stable.

3.4 Inner Detector(ID)

3.4.1 PMT in the inner detector

As explained in Section.3.2, there are 11,146 20-inch(50.8-cm)-in-diameter PMTs mounted on the surface of the inner detector. The PMT is an improved-version of the PMT employed

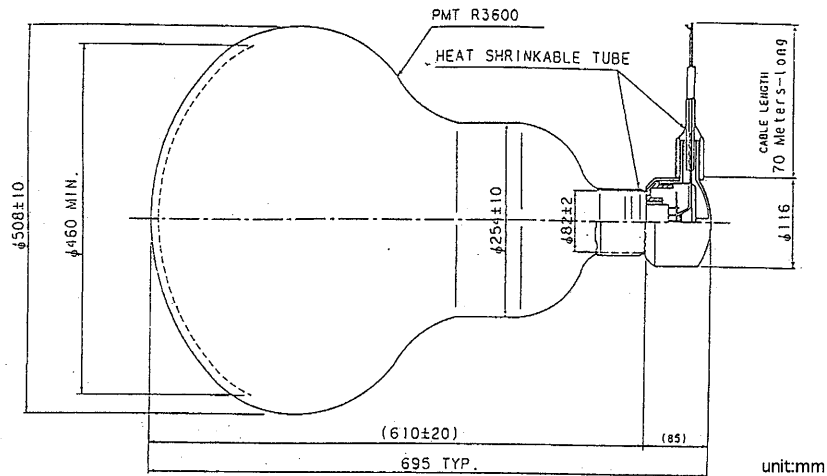


Figure 3.10: Inner detector 20-inch-in-diameter PMT

in Kamiokande[27]. It is specially developed for Super-Kamiokande by Hamamatsu Photonics Co. Ltd. The structure of the PMT is shown in Fig.3.10. The photo-cathode is made of bialkali(Sb-K-Cs) metal. This material is sensitive to the wavelength spectrum of Čerenkov light photons (see Fig.3.2). The quantum efficiency(Q.E.) is also shown in Fig.3.2 and reaches 22% at $\lambda=390\text{nm}$ which is a typical wavelength of Čerenkov light photons.

The PMT employs Venetian-blind dynodes, because they have the advantage of large photo-sensitive area. However, this type has a smaller collection efficiency(40 ~50%) for secondary electrons compared with other types, and this makes the energy and timing resolutions worse. Therefore, the first 3 dynode stages on which the collection efficiency mainly depends are optimized by means of simulation for electron trajectory, in which length and slant angle of blinds, distance between each stage, relative position of blinds and voltage division are tuned parameters. As a result of simulation, the number of stages is settled to 11 and the dividing ratio of high voltage is settled to 8 : 3 : 3 : 1 : : 1 (see Fig.3.11). After the optimization, the average collection efficiency for the new PMT exceeds 70%. Single photoelectron(p.e.) distribution of the PMT is shown in Fig.3.12. One p.e. peak is clearly separated from the noise. Single p.e. charge and timing resolutions are important for the solar neutrino analysis, as almost all the PMTs count only one photoelectron in a low-energy ($\sim 10\text{MeV}$) event.

Another important feature of the PMT is its water-proof structure, since the PMTs are set deep in water and have to tolerate as much pressure as 5 atm. The water-proof structure passed the testing under 6 atm. There has been no PMT broken due to water leakage in Super-Kamiokande, indeed.

The average dark noise rate in the PMT is about 4 kHz at the beginning of the experiment decreases to 3.1 kHz and stable now(see Fig.3.13).

In addition, since the large PMTs are sensitive to a small magnetic field, the geomagnetic field(450 mG) should be reduced. In order to cancel out the geomagnetic field, we use Helmholtz coils (Fig.3.14) which reduce the geomagnetic field to less than 100 mG in every position of the water tank.

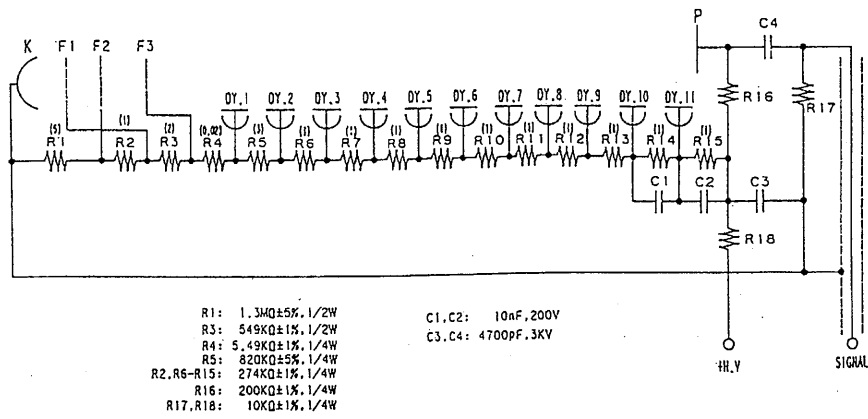


Figure 3.11: ID PMT base

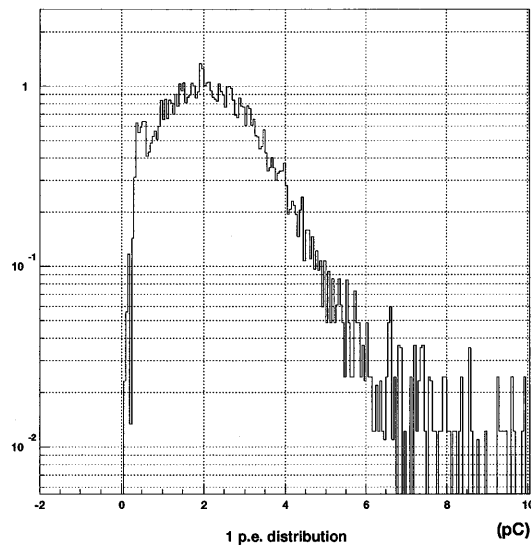


Figure 3.12: 1 photoelectron(p.e.) distribution of ID PMT.

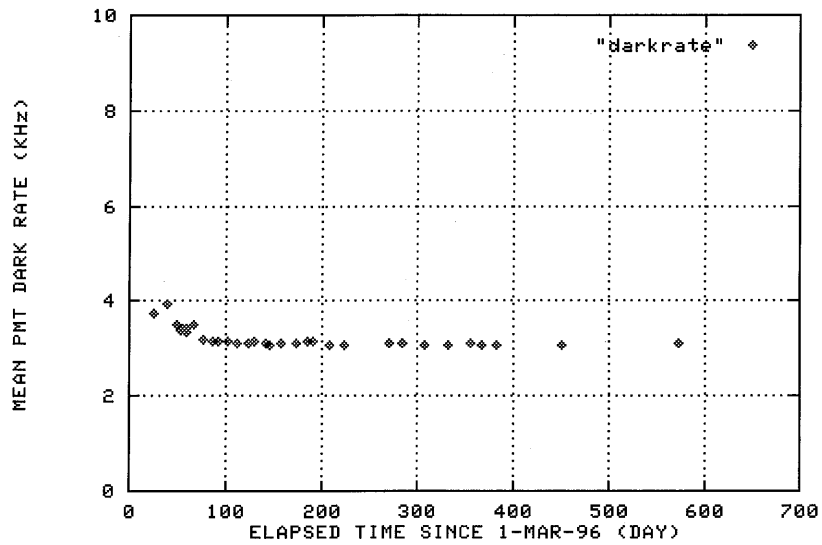


Figure 3.13: Time variation of dark noise rate of ID PMTs. The horizontal axis is the elapsed day from April 1, 1996 and the vertical axis is the dark noise rate in unit of kHz. At the beginning of the experiment, the dark noise rate was about 4kHz. But it gradually decreases to about 3 kHz and it is stable.

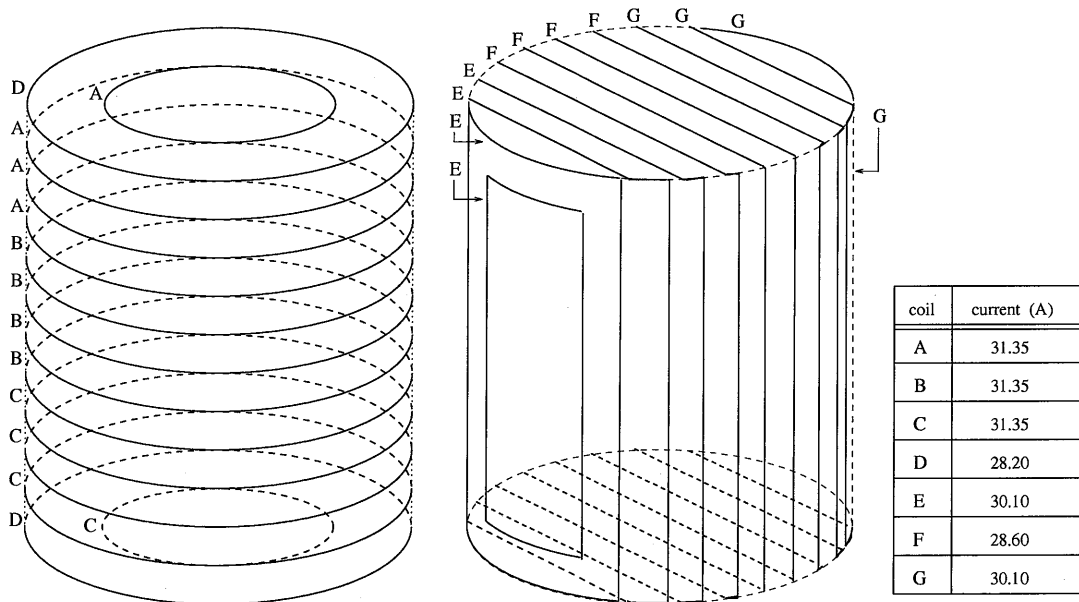


Figure 3.14: Helmholtz coils to cancel out the geomagnetic field

3.4.2 Electronics system for inner detector

The schematic view of the electronics system employed in the inner detector of Super-Kamiokande is shown in Fig.3.15. The electronics system is composed of front-end electronics,

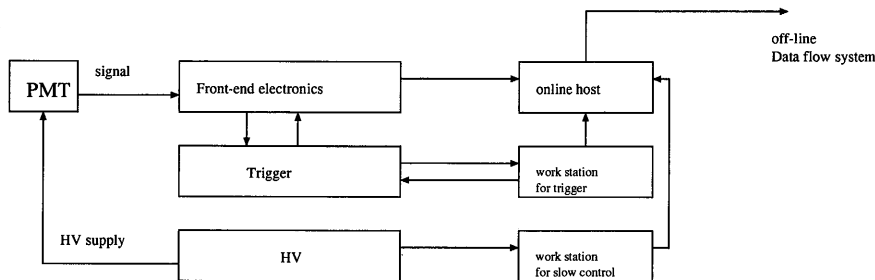


Figure 3.15: The electronics system of Inner detector

trigger system and high-voltage system. In this section, these components are explained one by one.

Front-end electronics

The front-end electronics of the inner detector employs 2 types of standard: one is TKO² and the other is VME. The schematic view of the front-end electronics is shown in Fig.3.16.

The front-end analog electronics adopted in Super-Kamiokande is named ATM³ which record both charge and timing information of each hit PMT. A signal from a hit PMT is fed into an ATM module which digitizes analog charge information and relative time between the photon arrival time and the global trigger time generated by the trigger system.

Each ATM module has 12 inputs and 20 ATM modules are nominally arranged in each TKO crate. In Super-Kamiokande, a total of 934 of ATM modules are used: they are distributed in 48 TKO crates. For readout, each TKO crate has one interface module "SCH"⁴, one trigger signal distribution module "GONG"⁵ and one summing circuit. Data received in a TKO crate which corresponds to approximately 240 channels are sent via SCH to SMP⁶ which is placed in a VME crate. One SMP has 6 data buffers and data in SMP are read out by an online computer via SBus-VME interface.

In the ATM, the signal from PMT is split into two. One is fed into an amplifier with a gain of 100, then discriminated when it goes over a threshold value of about 0.32p.e. Each output signal from a discriminator is summed by the module(12 channels). The signal after the summation is then sent to the trigger electronics for a HITSUM input with a width of 200 nsec and a voltage of -15mV. And a rectangular pulse of which width is 900 nsec is generated as a HIT signal, simultaneously. This HIT signal initiates charging of TAC⁷ and the charging

²TRISTAN/KEK Online

³Analog Timing Module by the TKO standard

⁴Super Control Header

⁵GO/NoGo

⁶Super Memory Partner

⁷time to analog converter

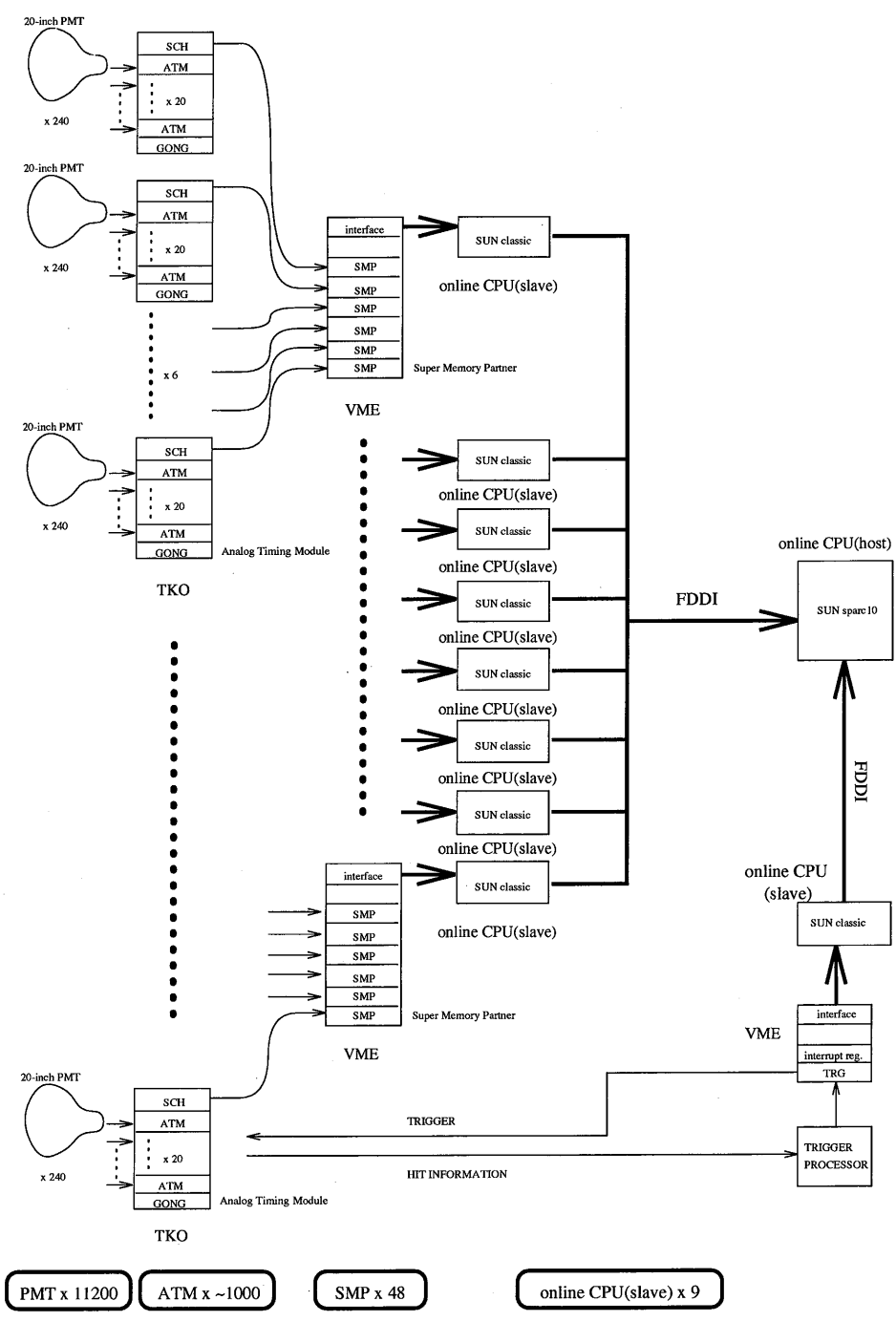


Figure 3.16: The block diagram of ID front-end electronics

ends when the global trigger signal arrives. The other split signal from PMT is fed into QAC⁸ and the HIT signal initiates the charge integration of QAC with its gate width of 400nsec. If the global trigger does not arrive, the TAC/QAC are reset 1.3 μ sec after the discriminator's hit. If the global trigger arrives, ADC⁹ start digitizing the voltages stored in the TAC/QAC capacitors. The ADC outputs are stored in a 1023-word FIFO¹⁰ memory tagged with the event ID¹¹ number. In addition, each TAC/QAC has a double buffer. This makes the DAQ¹² system essentially dead-time free.

Pedestal change affects the energy scale of low-energy events, so pedestal must be measured periodically in the data taking. In Super-Kamiokande, a pedestal run is taken every 30 minutes and it takes one minute for each 11146 channel check. Furthermore, to reduce dead time for possible supernova searches, the pedestal data is taken for a 1/8 part of all the ATMs at a time which are controlled by 1 DAQ online machine(described in Section.3.6).

Trigger system

The HITSUM signal mentioned above is summed up by using a summing amplifier in each TKO crate; after the summing, 1 hit signal is equivalent to about -10mV. Then, all the HITSUM signals are summed again and forms a global trigger signal if the summed signal exceeds a threshold value of -340mV corresponding to about 34 hits(5 ~ 6 MeV for an electron). In Super-Kamiokande, the trigger rate is about 10 Hz(see Fig.3.17) among which 2.2Hz comes from cosmic-ray muons.

The global trigger signal is fed into a "TRG¹³" module. This module has a 16-bit event counter and a 50MHz 48-bit clock. The relative time of an event is recorded with a 20 nsec resolution. The event information is stored in a FIFO memory located in the TRG module. The global trigger signal and the event counter signal is distributed to 48 GONG modules in the TKO crates. The GONG modules then distribute the global trigger signal and the event counter information to the ATM modules.

The trigger efficiency for an electron is described in Section.3.8.2.

High Voltage system

The high voltage(HV) power supply system is composed of HV modules(A933K), intelligent mainframes(SY527) and the VME interface modules(V288) which are made by CAEN Co. In Super-Kamiokande, about 480 A933K modules, 48 SY527 mainframes, and 4 V288 modules are used. One A933K has 24 HV output channels and 1 primary HV generator. The output voltage(maximum HV drop of 900V from the primary HV) of each channel is set and monitored(0.2 V resolution) individually and the primary HV generator has a current monitor (1 μ A resolution). Therefore, one can set and monitor the output voltage of each channel and monitor output current of each module. Typically 10 A933Ks are accommodated in a SY527 crate which is controlled remotely via a V288 module(VME \leftrightarrow CAENet interface).

⁸charge to analog converter

⁹analog to digital converter

¹⁰First In/First Out

¹¹Identification

¹²Data AcQuisition

¹³TRiGger

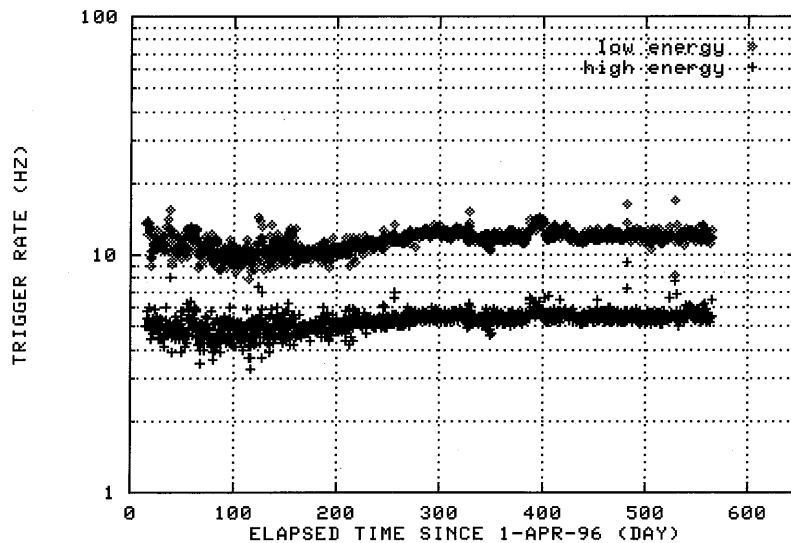


Figure 3.17: Time variation of trigger rate. The horizontal axis is elapsed days from April 1, 1996. The vertical axis is the trigger rate, and unit is Hz. Diamonds represents the low-energy trigger(~ 32 hits) rate, while crosses stands for the high-energy trigger(~ 34 hits) rate.

Schematic view of the high voltage power supply system in Super-Kamiokande is shown in Fig.3.18. The supplied high voltage of each PMT is monitored and checked every 10 minutes.

3.5 Outer Detector(OD)

3.5.1 Outer-Detector PMT

In the outer detector, 1,885 8-inch(20.8-cm)-in-diameter PMTs manufactured by Hamamatsu Co. are two-dimensionally mounted. Each PMT is equipped with a 60×60 cm wavelength shifter plate(see Fig.3.7). Photons in a wavelength range between 300 nm and 400 nm are absorbed by the wavelength shifter and approximately 55% of the photons are isotropically re-emitted with a longer wavelength . The PMT photo-coverage is consequently doubled due to the wavelength shifter plate.

3.5.2 Electronics system for outer-detector

The outer-detector PMT signals are separated from the positive HV supplied to the PMT in a HV pickoff cards. One HV pickoff card handles outputs from 12 PMTs. The PMT signals are processed by "QTC" modules. One QTC handles signals from 48 PMTs. This modules record both the arrival time and the total charge integrated over the 200nsec window, and the threshold is $1/4$ p.e.. The output of QTC consists of the short pulse making the time, and following variable pulse proportional to the PMT charge. Both pulses in 80 QTC modules are fed directly into a Lecroy 1877 TDC(Time to Digital Converter) channel to be digitized. After

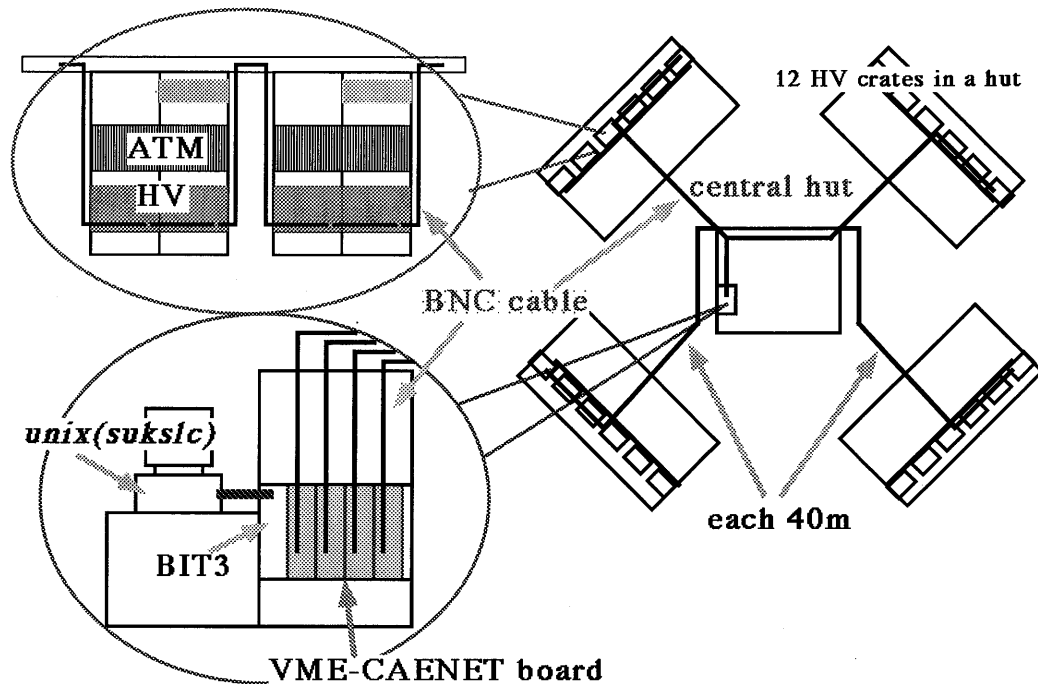


Figure 3.18: Schematic view of HV control system

digitization, if the global trigger arrives, the data is read out to a very large VME buffer with a connection via FDDI¹⁴ to an online host computer as described in the next section.

In addition, the output of QTC has the sum of the discriminatory outputs, or analog HIT-SUM output, and it is used for an outer-detector trigger to detect the event which doesn't enter the inner detector. The outer-detector trigger threshold is set to coincidence of 16 PMTs hit in a 200nsec window.

3.6 Online DAQ system

As explained in Section.3.4.2, charge signals and relative time information of each hit PMT is digitized by ATMs, sent to SMPs, and read out by online computers via SBus-VME interface.

Super-Kamiokande uses 8 slave online computers for the inner-detector data acquisition, and 1 online computer for the outer-detector data acquisition, 1 computer for the trigger and 1 host computer to integrate data collected by the online-computers. In each electronics hut, there are 2 online computers(Sun SPARClassic S4/CL, named "sukon") for the inner detector and each online computer collects about 1440 PMTs' data. These data are transferred to the host computer(Sun SPARCstation 10 S4/10) via FDDI. The trigger computer placed in the central hut controls the TRG module and receives the output signal from the TRG module. The trigger information received by the trigger-computer are also sent to the host computer. The data from the outer-detector PMTs are collected by the outer-detector online-computer("sukant") which is placed in the central hut. The outer-detector's data are transferred to the host-computer

¹⁴high speed ring network with optical fiber cable

via Ethernet and the host-computer integrates data from the inner-detector and outer-detector PMTs and the trigger information.

Data which are integrated by the host-computer(“sukonh”) are sent to a monitor computer and a data-reformatting computer. The monitor computer (SPARCstation 20) placed in the control room is used to check the data acquisition and the detector status. The reformatting computer(UltraSPAC, named “sukrfm”) which is also placed in the control room is used to change the online data format into an off-line data format ZEBRA¹⁵

3.7 Off-line Analysis System

After the reformatting process, the data are sent to the off-line host computer every 10 minutes: This file is about 70 MBytes in size. The off-line host computer(VPX210/10S, “skuop”) is located in the computer room of the laboratory outside the mine. This host computer saves all the data in a mass storage¹⁶ library(MTL) and converts the integer data of ADCs and TDCs to the number of photoelectrons and nano seconds, respectively. This conversion process is called “TQreal”.

After TQreal, the data are distributed to off-line computers. Each off-line computer(Sun SPARCstation 20, “sukeve”) has 2 CPUs and is connected with the host and the others via network named “UltraNet1000”. These off-line computers serve as event fitters. More workstations are available for analysis. A flowchart of the online DAQ and the off-line analysis is shown in Fig.3.19.

3.8 MC simulation of Super-Kamiokande

Here, we consider behaviors of scattered electrons and Čerenkov photons in the Super Kamiokande detector. Hence, using a Monte Carlo(MC) simulation, we estimate the detector response. The MC simulation is constituted by 4 components; 1) electron tracking, 2)Čerenkov photon generation and propagation , 3)PMT and 4)trigger efficiency. Considering the behaviors of the components the MC was tuned with Ni calibration data which will be described in Section.4.5. In this section, the first and the last components are described. The others are described in the next Chapter. Some considerations for the solar neutrino analysis are explained in Section.5.3.1.

3.8.1 Electron tracking

In this analysis, a simulator which is based on GEANT is used. GEANT is a tool for the detector simulation developed in CERN¹⁷. EGS¹⁸ is used in GEANT to simulate electromagnetic interactions. EGS supports an energy range from a few tens of keV to a few TeV for charged particles and from 1keV to several thousand GeV for a photon. GEANT-EGS simulation system take account of the following physical processes; Coulomb multiple scatterings, ionization loss, δ -ray production, bremsstrahlung, annihilation of positron, Møller and Bhabha scatterings

¹⁵ZEBRA is the tool for data management which is developed in CERN.

¹⁶In Super-Kamiokande, the compact magnetic tape(CMT 3090) is used.

¹⁷European laboratory for particle physics

¹⁸Electron-Gamma Shower code

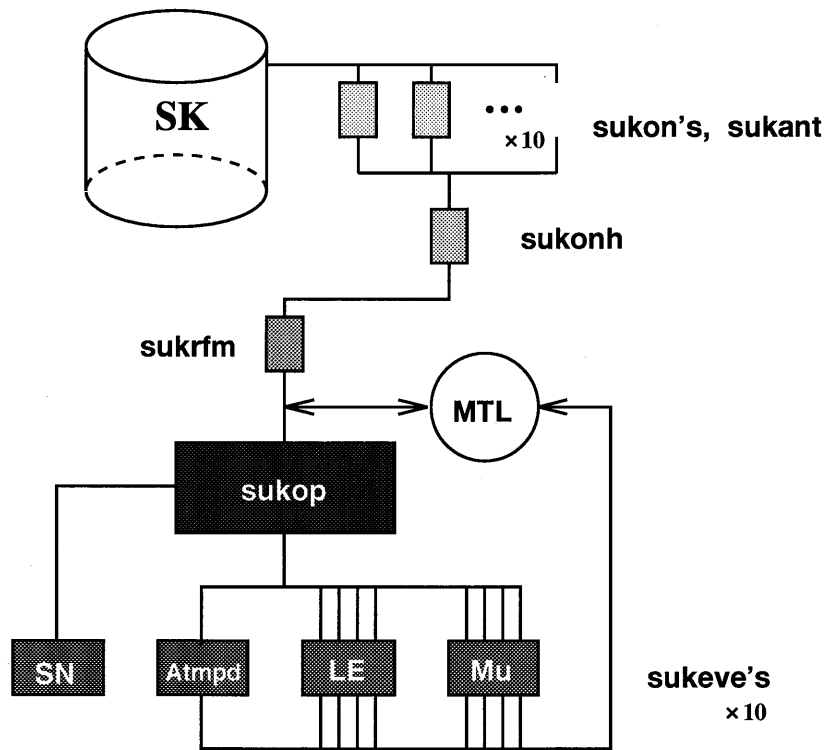


Figure 3.19: Schematic view of data flow. SN represents a supernova monitoring process. Atmpd represents an analyzing process for atmospheric neutrino events and nucleon-decay search. LE represents an analyzing process for low-energy events and Mu represents an analyzing process for cosmic-ray muon events.

and generation of Čerenkov photons for an electron; pair production, Compton and Rayleigh scatterings and photoelectric effect for a photon.

3.8.2 Trigger efficiency

Trigger efficiency is simulated and compared with real data. For this comparison, Ni calibration data are used. Figure 3.20 shows the trigger efficiency of MC simulation and Ni calibration data as a function of visible energy N_{eff} . (For definition of N_{eff} , see Appendix.F) Our MC

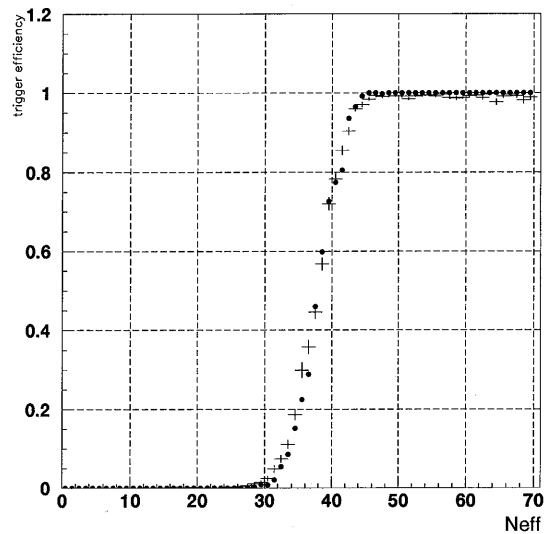


Figure 3.20: Trigger efficiency. Horizontal axis is N_{eff} defined in Appendix.F, and the vertical axis is efficiency. Black dots correspond to simulated result, and cross correspond to Ni calibration data. In this figure, 7MeV is about $47 N_{eff}$.

simulation reproduces data quite well in the energy region greater than 7MeV($\sim 47 N_{eff}$). But in the lower energy region, the agreement becomes slightly worse. For example, at 6.5 MeV($\sim 43 N_{eff}$), the difference(Data-MC) is +1.2% which is taken into considerations in the systematic errors.

Chapter 4

Calibration

4.1 Gain of PMTs

4.1.1 Relative Gain of PMTs

In order to keep uniformity of the detector, the high voltage of each PMT is adjusted to make the relative gain of all the PMTs same.

Our system to measure the relative gain of each PMT is shown in Fig.4.1. Light from a

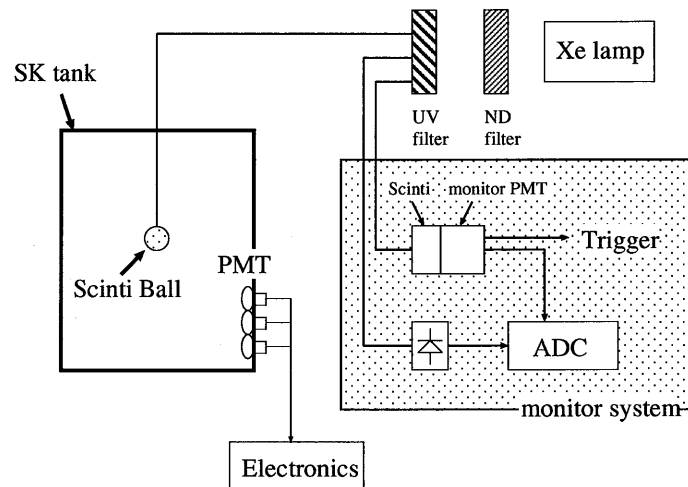


Figure 4.1: PMT gain calibration system

Xe-lamp is passed through ultra-violet filters and injected into a scintillator ball via an optical fiber. The scintillator ball is made of an acrylic resin in which BBOT and MgO powders are uniformly mixed. The BBOT and MgO are used as a wavelength shifter and a light diffuser, respectively. The intensity of the U.V. light is monitored by a separate scintillator monitor which gives a trigger signal(see Fig.4.1).

With this system, the measurements are done at various positions in the Super-Kamiokande detector. The high voltage value of each PMT are adjusted, after corrections including light attenuation in the detector water, uniformity of the scintillator ball, acceptance and intensity of

the Xe light. In Fig.4.2, the gain distributions of barrel PMTs are shown. From these figures, the relative gain spread is estimated to be 7%(1 σ).

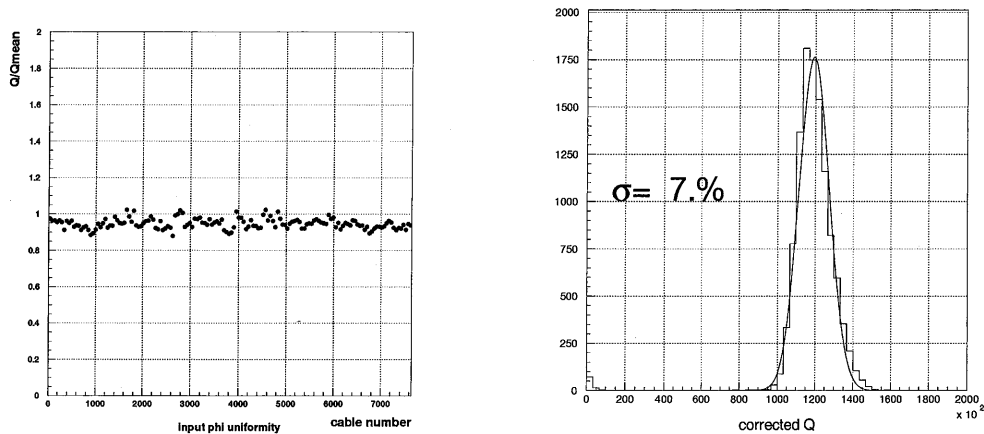


Figure 4.2: The left figure shows a relative gain distribution of PMTs labeled by their cable number. Gain spread from the central value is shown in the right figure. In the right figure, the horizontal axis is Q(charge) after correction for detector geometry and water transparency in unit of pC·m².

4.1.2 Single p.e. distribution

The relative gain was adjusted at a high charge ($Q \approx 300 \sim 500$ pC) region where the number of photons is large. In this region, the output charge from a PMT is in proportion to the number of photons. However, for a low-energy event such as produced by a ⁸B solar neutrino, most hit PMTs detect single-photon signal. Therefore, understanding the gain of each PMT at a small charge region is very important to analyze ⁸B solar neutrinos.

The electronics system measures only charge output of each PMT. A conversion coefficient from the charge to the number of photoelectrons is needed. Nickel calibration data to be described in Section.4.5.2 is used to obtain the coefficient. In Fig.4.3, the single p.e. charge distribution of a typical PMT is shown in unit of pico coulomb. From this figure, we can get the coefficient; 2.055 pC is equivalent to 1p.e.

Next, one check uniformity of “occupancy” which is defined to be a ratio $\frac{\text{number of hits}}{\text{total number of events}}$ for each PMT at one p.e. light level. Uniformity of “occupancy” is important in the low energy region, to reduce the position and direction dependence of the energy scale. The data taken in the Nickel calibration runs(described in Section.4.5.2) are also used to measure the occupancy. In Fig.4.4, the distribution of the average occupancy of barrel PMTs is shown. Some PMTs at the barrel have higher occupancy than the others. The difference comes from different single photoelectron detection efficiency of the PMTs. The variation of efficiency depends on the production time of PMTs. The PMTs with higher occupancy were made earlier than the others. The difference is 20% on the average. The non-uniformity is considered in the energy determination which is described in Appendix.F. Except for them, the occupancy near the upper and lower layers looks higher than that at the central layers. This apparent difference comes from the photon reflection at the surface of PMT, which is confirmed by a M.C. simulation. Uniformity

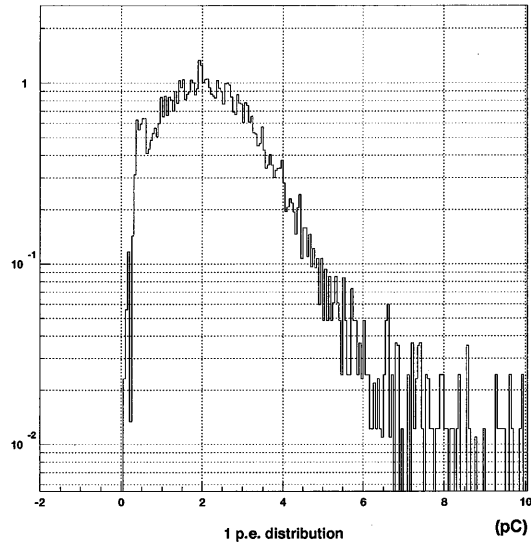


Figure 4.3: Single charge distribution. The horizontal axis is charge in unit of pC, and the vertical axis is an arbitrary unit. The slump in the lower charge region is due to threshold effect of discriminator.

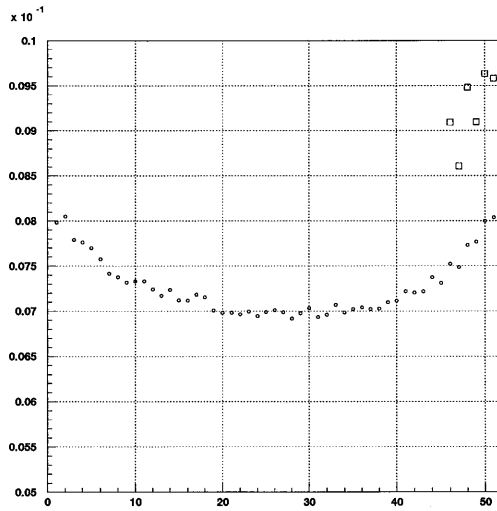


Figure 4.4: Occupancy distribution for barrel PMTs. The vertical axis is the occupancy of barrel PMTs, and the horizontal axis is the layer number of super-module(see Section.3.2). Circles and squares correspond to new and old lot of PMTs, respectively

of occupancy on the top and bottom PMTs is also checked. The occupancy distribution averaged over PMTs along a concentric ring is shown in Fig.4.5 as a function of ring radius. The apparent

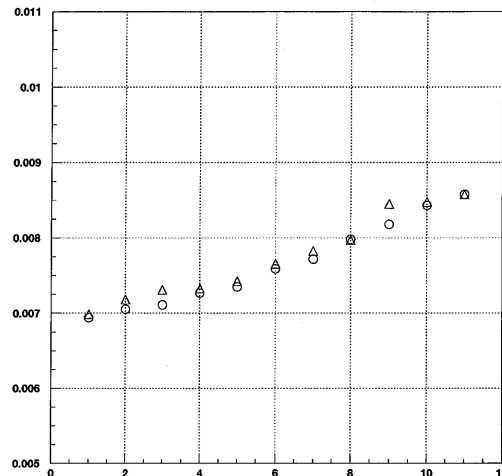


Figure 4.5: Occupancy for top/bottom PMTs. The horizontal axis is distance in unit of meter, from the center of the top/bottom planes. Circles and triangles correspond to top and bottom PMTs, respectively.

non-uniformity is also caused the photon reflection on the surface of PMT.

4.2 Relative Timing of PMTs

The resolution of reconstructed vertex point of a low-energy event depends on relative hit time of each PMT. Because of slewing effect of a discriminator, the relative hit time becomes a function of observed charge(pulse height).

A system illustrated in Fig.4.6 is used to measure the correlation. Here, a N_2 laser is used as a light source. The pulse width of the light is typically 3 nsec. The wavelength of the N_2 laser light is 337 nm and is converted to 384 nm by a dye laser module, which is similar to Čerenkov light spectrum. Also, a set of optical filters are used to change the light intensity in order to measure the hit PMT time at various pulse heights. The light is split into two, one is guided to a diffuser ball in the tank via optical fiber cable, and the other is used to monitor the light intensity and to make a trigger signal.

In Fig.4.7, a typical correlation of hit time(T) versus charge(Q) is plotted. This distribution is called "TQ-map". The TQ-map is made for each PMT, and it is used for real data to correct the slewing effect.

At the same time, dependence of the timing resolution on pulse height is measured and is shown in Fig.4.8. The timing resolution is approximately 3nsec at single p.e. The timing resolution is incorporated into our MC simulation.

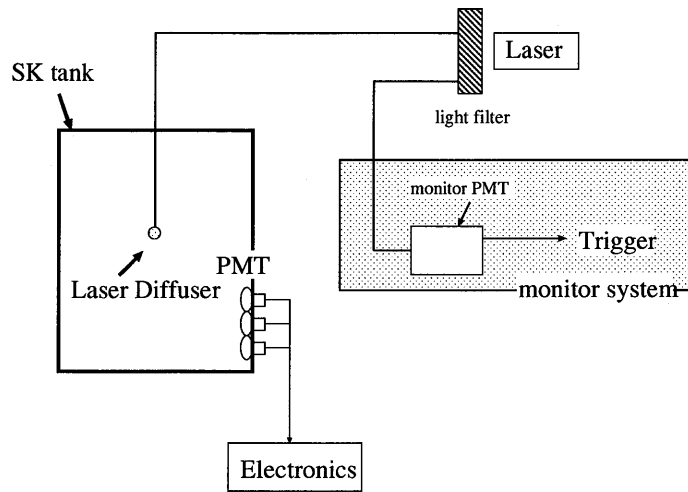


Figure 4.6: Timing calibration system

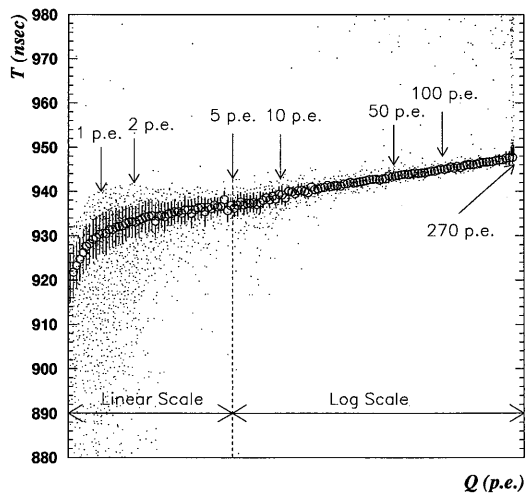


Figure 4.7: Typical TQ-map distribution. Dots represent measured data and circles represent the mean value.

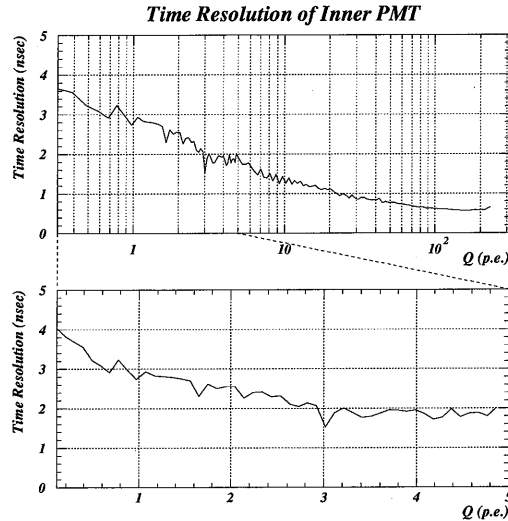


Figure 4.8: Timing resolution of inner-detector PMTs as a function of charge(p.e.).

4.3 Consideration of PMT response in Monte Carlo simulation(MC)

When the PMT response is simulated, one considers the quantum efficiency and dynode collection efficiency, noise, charge and timing resolution.

The quantum efficiency of the PMT is measured at Hamamatsu Photonics as shown in Fig.3.2. In our MC simulation, this measured value is used.

The dynode collection efficiency is treated as a tunable parameter when one compares our MC simulation with Nickel calibration data. It is set at 0.88.

There are two types of noise belonging to PMT; one is the dark current and the other is after-pulse. The dark noise rate is about 3.1 kHz and stable. Our PMT have an the after-pulse which typically arrives 100 nsec after a signal. In our MC simulation, the after-pulse is generated with 2% probability distributed in a Gaussian shape with a width of 10 nsec.

The charge and timing resolutions of the PMT are calibrated using a method described in Sections.4.1, and 4.2. Furthermore, heterogeneous occupancy is considered in our MC simulation to simulate the PMT response. The measurement of occupancy is done with Ni calibration data.(see Section.4.1.2)

4.4 Water Transparency measurement

In Super-Kamiokande, Čerenkov photons are used to reconstruct an event. Since Čerenkov photons travel a long distance(detector linear dimension $\sim 30\text{m}$) before being detected by PMTs mounted on the tank wall, attenuation of them in water is considered. Two methods are employed to measure the transparency; 1) a laser and CCD camera system, and 2) electrons from μ decay. The first one does a direct measurement, and the other uses real data taken in Super-Kamiokande.

With the laser system, one can measure the water transparency for various wavelength which is used to tune up our Monte Carlo(MC) simulation.

As one can't measure the transparency continuously, one also employs real data to monitor water transparency in the detector and its long-term stability.

4.4.1 Direct Measurement with laser

The direct measurement is done with a system which consists of laser, diffuser ball, CCD camera and control system. A schematic view is described in Fig.4.9. In this system, a N_2 laser

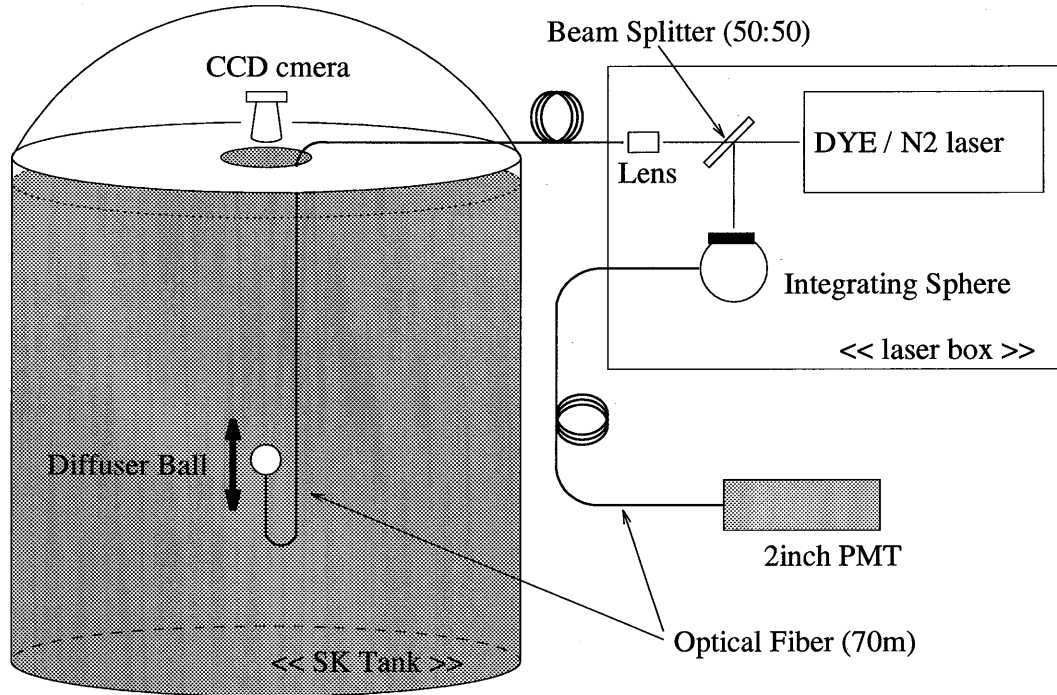


Figure 4.9: Schematic view of direct measurement of water transparency

and a dye module are used as the light source. As the N_2 laser produces only monochromatic light(337nm), it is converted to a diffuse light with a different wavelength by the dye module.

Passing through the dye module, the light is split into two by a half mirror. One is led to 2-inch-in-diameter PMT for monitoring the light intensity, and the other is guided to an acrylic diffuser ball via optical fiber cable. This diffuser ball is set up in the water tank and the light from the ball is measured by a CCD camera. Measurements are done at several distances between the ball and the camera. After correction with data taken by the monitoring PMT, the water transparency is calculated. The measurement is carried out at various wavelengths and the result is shown in Table.4.1 and Fig.4.14. This result is taken into account in our MC tuning (Sub-Section.4.4.3).

wavelength(nm)	water transparency(m)	error(%)
337	40.90	2.52
400	99.74	6.04
500	33.47	2.09
580	10.17	0.64

Table 4.1: Water transparency measured by laser system.

4.4.2 Measurement with μ -decay electrons

In Super-Kamiokande, cosmic-ray muons hit the detector at a rate of 2.2 Hz, among which 3 ~ 4% stop in the detector. The stopping muon decays in water and emits an electron. In Fig.4.10, a typical stopping muon event is shown, together with an accompanied μ -decay electron.

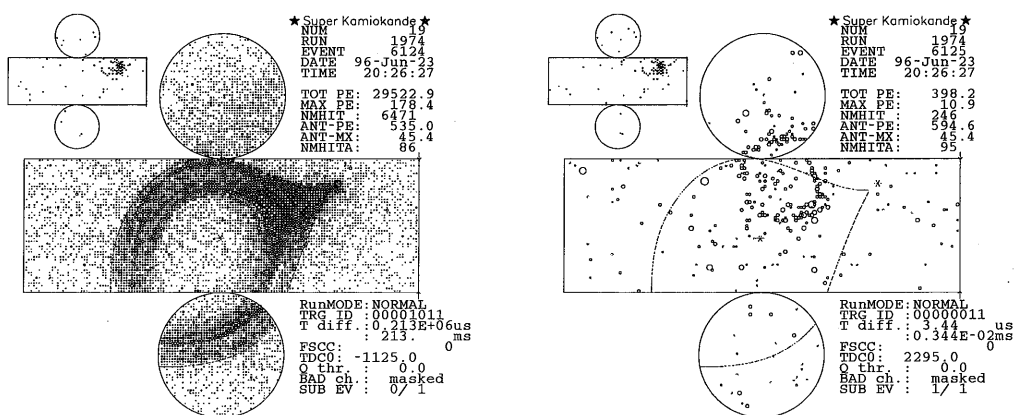


Figure 4.10: A typical stopping muon(left) and an accompanied μ -decay electron(right).

The water transparency measured by μ -decay electrons represents an average value integrated over the Čerenkov light spectrum at single-photoelectron light level. A μ -decay electron is tagged by a selection criterion that time difference between the preceding event and the electron candidate is 1.5~8.0 μ sec. The range of μ -decay electrons in water is less than the vertex position resolution($1 \sigma \approx 70$ cm at 10MeV). Therefore, their track length is short enough to be approximated as a point. Reconstruction method of their vertex point and direction are described in Appendix.A and Appendix.B, respectively.

Then, one selects hit PMTs in the electron event which satisfy the following conditions:

- 1) the detected photon lies within a 50-nsec time window from the expected arrival time as calculated from the photon flight path.
- 2) The PMTs should lie in a cone with a half opening angle of 32-52 degrees measured from the electron direction(Fig.4.11). After the selection, one considers a virtual sphere with a radius of R and with its center at the vertex position of the event. The selected PMTs are projected back onto this sphere. They should form a ring on the sphere. Then, they are divided into 36 azimuthal 10-degree bins as shown in Fig.4.11. On the sphere, the effective charge in the i-th

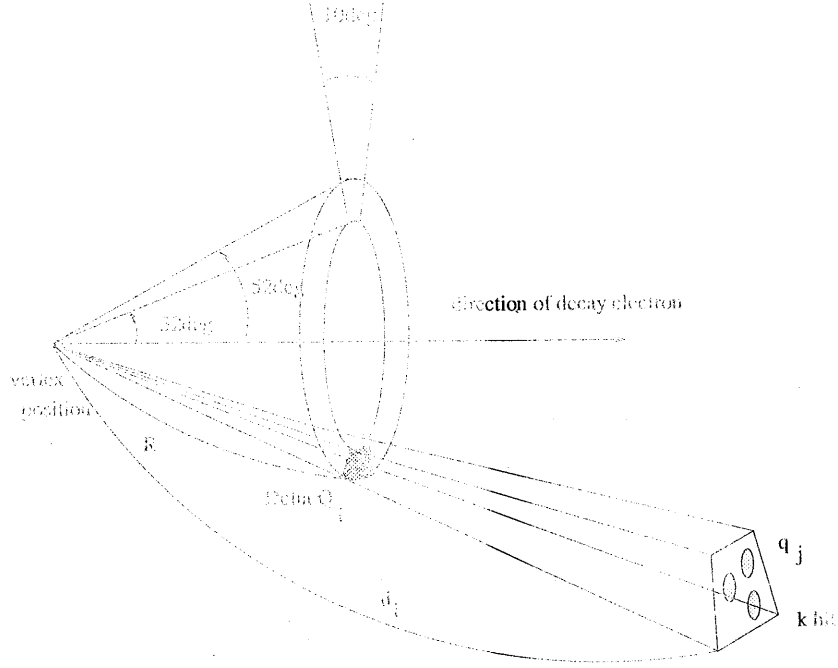


Figure 4.11: Schematic view of hit PMT selection for calculation of water transparency

bin is

$$\Delta Q_i = \sum_{j=1}^k q_j \exp\left(\frac{d_j - R}{\lambda}\right), \quad (4.1)$$

$$\approx \exp\left(\frac{\bar{d}_i - R}{\lambda}\right) \sum_{j=1}^k q_j, \quad (4.2)$$

where d_j is the distance from the vertex point of the electron to the j -th PMT in the i -th bin, λ is the attenuation length of water, k is the number of **hit** PMTs in the i -th bin, q_j is the number of photons detected by the j -th PMT after PMT acceptance correction and \bar{d}_i is the average of the distances d_j . Ideally, ΔQ_i would satisfy the following relation,

$$\Delta Q_1 = \Delta Q_2 = \dots = \Delta Q_{36} \equiv \Delta Q. \quad (4.3)$$

Then, one can set $R \rightarrow 0$ without any change, and ΔQ can be described as

$$\Delta Q = \exp\left(\frac{r}{\lambda}\right) q(r), \quad (4.4)$$

where \bar{d}_i is replaced by r , and $q(r) = \sum_{j=1}^k q_j$.

Then, every T days, one collects μ -decay electrons and fit them assuming

$$\bar{q}(r) = \exp\left(\frac{-r}{\lambda}\right) \Delta Q \quad (4.5)$$

Then,

$$\lambda = r \cdot \log \left(\frac{\overline{q(r)}}{\overline{\Delta Q}} \right), \quad (4.6)$$

where $\overline{q(r)}$ and $\overline{\Delta Q}$ are the average of $q(r)$ and ΔQ over 7 days, respectively.

The water transparency and its long-term stability measured by the μ -decay electron data is shown in Fig.4.12.

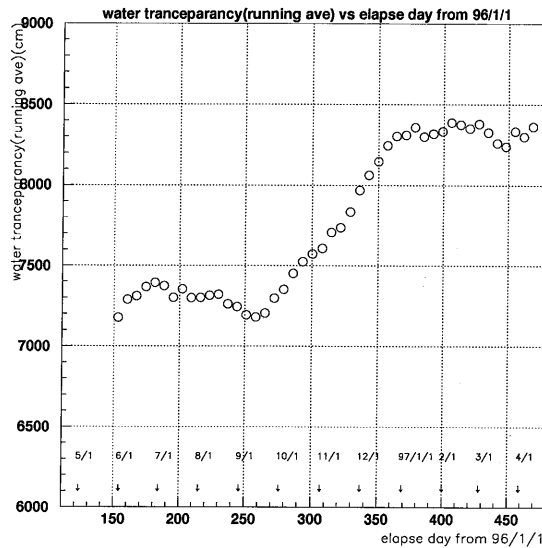


Figure 4.12: Variation of the detector water transparency measured by μ -decay electrons as a function of elapsed time since January 1, 1996. One circle corresponds to 7-day data. The rapid change after 250 days is caused by replacement of ULTRA FILTER in the water purification system(Section.3.3.1).

4.4.3 Input parameters of our MC simulation

Čerenkov photon propagation

General conditions to generate Čerenkov photons and their spectrum have been already described in Section.3.1. Hence, in this section, a method to propagate photons in the simulator is described.

The PMTs detect not only direct photons but also reflected photons. Especially, the reflectivity and its incident angle dependence is important.

Components of the Super-Kamiokande detector, relevant to the photon propagation, are water in the tank, and reflection at black sheets on the wall of the water tank, and at the surface of PMTs. To simulate the photon propagation in the Super-Kamiokande detector, scattering and absorption at these components are separately considered .

propagation in water

When a medium matter is dispersive as water, one should take into account the dispersion relation of the refraction index for calculation of the velocity of the light propagation. This velocity is not the phase velocity, but the group velocity which is approximated by:

$$v_g = \frac{c}{n(\lambda) - \lambda \frac{\partial n(\lambda)}{\partial \lambda}}, \quad (4.7)$$

where v_g is the group velocity, λ is wavelength of photons and $n(\lambda)$ is the refraction index dependent on wavelength. $n(\lambda)$ is given by the following formula[28],

$$n(\lambda) = \sqrt{\frac{a_1}{\lambda^2 - \lambda_a^2} + a_2 + a_3 \cdot \lambda^2 + a_4 \cdot \lambda^4 + a_5 \cdot \lambda^6} \quad (4.8)$$

where λ is wavelength in unit of μm , $\lambda_a^2 = 0.018085$, $a_1 = 5.743534 \times 10^{-3}$, $a_2 = 1.769238$, $a_3 = -2.797222 \times 10^{-2}$, $a_4 = 8.715348 \times 10^{-3}$, and $a_5 = -1.413942 \times 10^{-3}$. Its spectral dependence in water is shown in Fig.4.13.

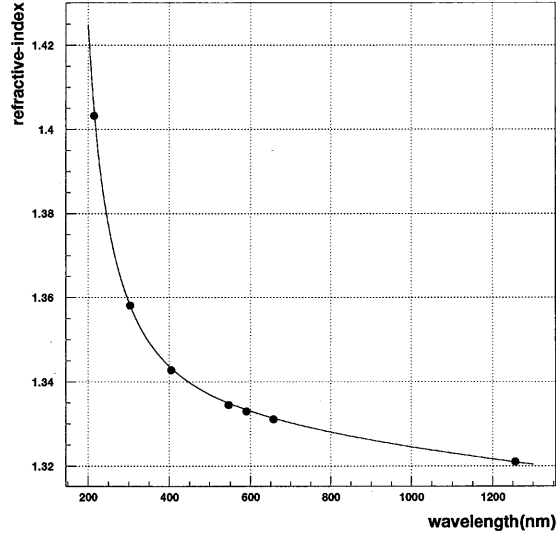


Figure 4.13: The refraction index of water dependent on wavelength. Dots represent the data listed in [29] and solid line stands for Eq.4.8.

Next, one considers probability of scattering and absorption of Čerenkov light photons in water.

For a short-wavelength region, Rayleigh scattering is dominant, because the size of particles with which Čerenkov photon interacts is small enough compared with the wavelength. For a long-wavelength region, the photons are scattered isotropically. The data are given by a reference [30].

Then, one determines the ratio of scattering to absorption of photons in water. The ratio is not a measurable value at the Super-Kamiokande experiment. Therefore, in our MC tuning,

it is treated as a free parameter. After tuning, the spectral dependence of water transparency employed in our MC simulation is shown in Fig.4.14.

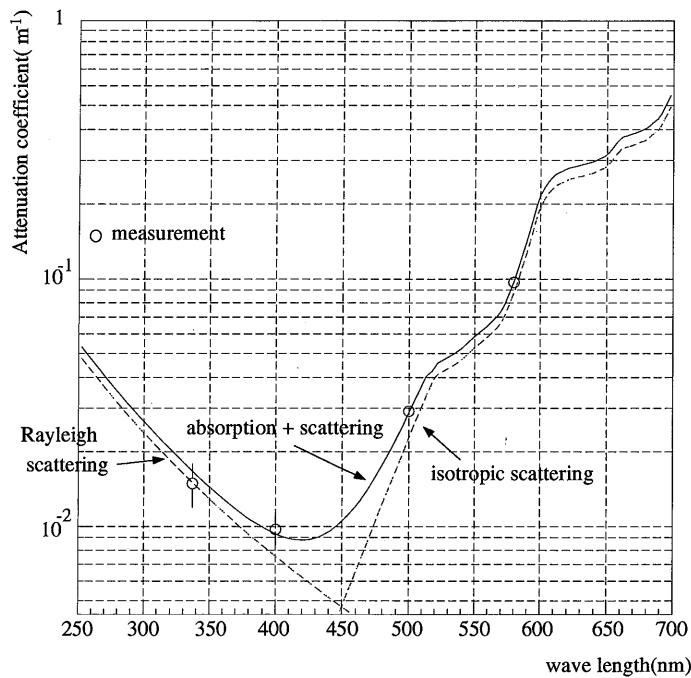


Figure 4.14: Water transparency. Attenuation coefficient is a reciprocal of attenuation length. Dashed line represents a theoretical prediction. Solid line represents our tuning result. The measurement is described in Section.4.4.1.

scattering and absorption at black sheets and surface of PMT

Reflectivity of black sheet was measured in the air and is converted to that in water (see Fig.4.15). In this calculation, the refractive index of black sheet is assumed to be 1.6, and polarization dependence of reflectivity is also considered[31]. In our MC simulation, reflectivity averaged over S-wave and P-wave is used.

Reflection at the surface of PMT is calculated with the standard electro-magnetic law, where the polarization of light is considered. The calculated reflectivity is shown in Fig.4.16 together with measured values at 7 incident angles in water.

4.5 Absolute Energy Scale and Energy resolution Calibrations

In a low-energy($\sim 10\text{MeV}$) region, number of hit PMTs is used to calculate the energy of an event. A recoil electron scattered by a ^8B solar neutrino gives typically an energy deposit of 10MeV in the Super-Kamiokande detector. The hit PMTs (45 hits at 10MeV at the center of detector) detects mostly a single photoelectron signal. Therefore, the energy is approximately proportional to the number of hit PMTs. On the other hand, total number of photoelectrons is not a good measure of energy around 10MeV , as it is affected by the fluctuation in the electron

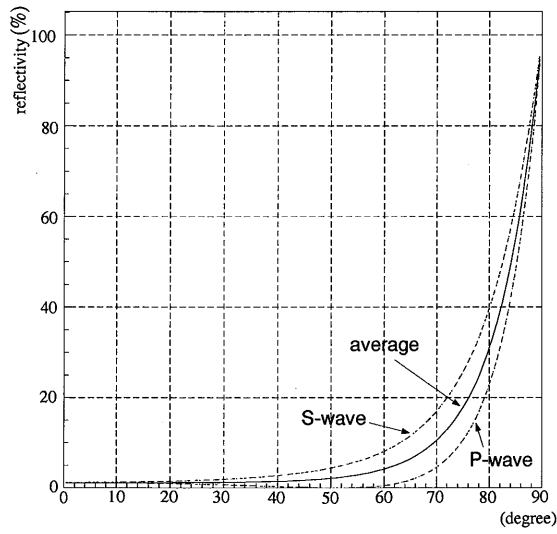


Figure 4.15: Reflectivity of black sheet. The horizontal axis is incident angle in unit of degree, and the vertical axis is reflectivity.

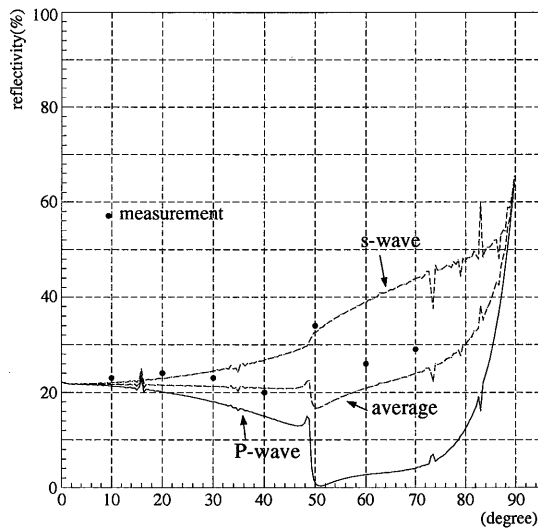


Figure 4.16: Reflectivity of PMT surface. The horizontal axis is incident angle in unit of degree, and the vertical axis is reflectivity. Black dots represents data point.

multiplication process in PMT[32],[33],[34],[35],[36]. Three calibration sources are employed to calibrate the energy scale in the low-energy region; One is a radioactive source(γ -rays from Ni), the second is an electron linear accelerator(LINAC), and the third μ -decay electrons. As data can be quickly taken with the radioactive source at several points in the detector, the results are used to pre-tune the energy scale and to calibrate the position dependence of the energy scale. To fine-tune the absolute energy scale and to measure the energy resolution, the most reliable LINAC data which has become available just recently are used. The energy spectrum of μ -decay electrons is also used to check the long-term stability of the energy scale.

4.5.1 Definition of Energy Scale

The simplest idea to determine the energy scale is to count the number of “on-time” PMT hits. N_{50} is defined as the maximum number of PMT hits in 50ns time window after suitable photon TOF¹ subtraction, based on the reconstructed vertex position and direction (see Appendix.A, and B) of an event. However, N_{50} depends on the vertex position, due to light attenuation by the detector water transparency, solid-angle dependence of PMT photo coverage, light reflection, and so on. Then, the effective number of PMT hits (N_{eff}) is employed in the calculation of the energy scale. N_{eff} is a corrected N_{50} and its definition is described in Eq.F.1(Appendix.F).

4.5.2 Energy Scale Pre-tuning and its Position dependence by Radioactive source

In Super-Kamiokande, gamma-rays emitted from a thermal neutron capture reaction in nickel is used as a calibration source of low-energy events. ^{252}Cf decays via α emission(96.9%) and spontaneous fission (3.1%) with a half life of 2.65 years. At a spontaneous fission, it emits 3.76 neutrons per 1 fission. Average energy of these is about 2MeV. The neutrons emitted by the ^{252}Cf source are thermalized in the water between the source and the nickel target.

Natural nickel mainly contains ^{58}Ni , ^{60}Ni , ^{62}Ni , and ^{64}Ni . When they are irradiated by the thermal neutrons from spontaneous fissions of ^{252}Cf , they emit γ -rays via the following reactions; $^{58}\text{Ni}(n,\gamma)^{59}\text{Ni}^*$, $^{60}\text{Ni}(n,\gamma)^{61}\text{Ni}^*$, $^{62}\text{Ni}(n,\gamma)^{63}\text{Ni}^*$, and $^{64}\text{Ni}(n,\gamma)^{65}\text{Ni}^*$. Furthermore the $\text{Ni}(n,\gamma)\text{Ni}^*$ reactions have many transition schemes. In Fig.4.17, an example is illustrated. In Table 4.2, the natural abundance of Ni isotopes and relevant radiative reactions are summarized. When

Reaction	Natural abundance (%)	energy (MeV)	cross section (barn)	relative intensity (%)
$^{58}\text{Ni}(n,\gamma)^{59}\text{Ni}^*$	67.88	9.000	4.4 ± 0.3	65
$^{60}\text{Ni}(n,\gamma)^{61}\text{Ni}^*$	26.23	7.820	2.6 ± 0.2	15
$^{62}\text{Ni}(n,\gamma)^{63}\text{Ni}^*$	3.66	6.838	15 ± 0.3	12
$^{64}\text{Ni}(n,\gamma)^{65}\text{Ni}^*$	1.08	6.098	1.52 ± 2	0.4

Table 4.2: Thermal neutron capture information

the fission neutrons from ^{252}Cf are not captured by the nickel target, they are captured instead by protons in water, and 2.2MeV(monochromatic) γ -rays are emitted via the $\text{H}(n,\gamma)\text{D}$ reaction.

¹Time Of Flight

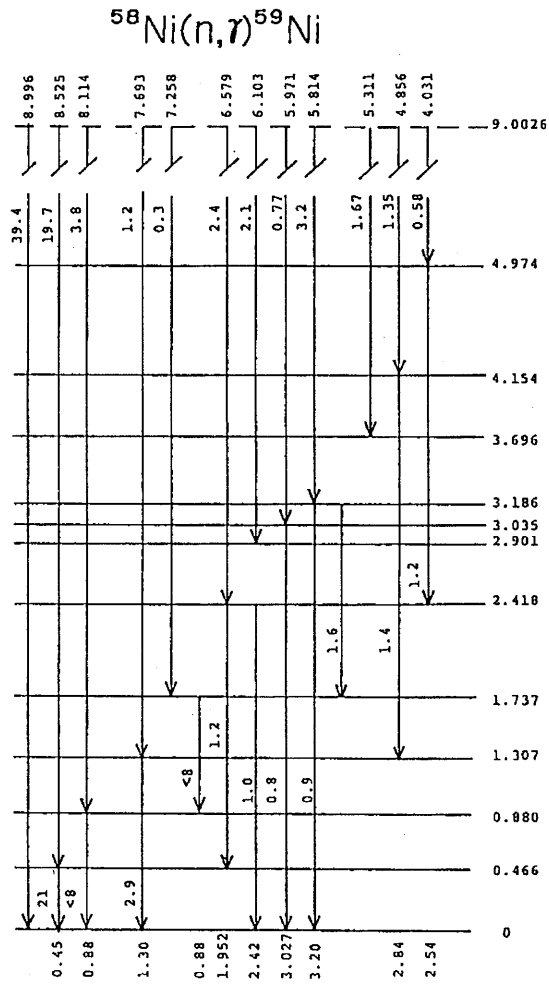


Figure 4.17: The transition diagram of $^{58}\text{Ni}(n,\gamma)^{59}\text{Ni}^*$

The γ -rays from this reaction are a main background in this calibration scheme. The cross section of this capture process is 0.332 barn, and the neutron mean life in the water is 205 μ sec.

The energy scale is calibrated by comparing the Ni γ -ray data with our Monte Carlo simulation incorporating the detector response.

A schematic view of the whole calibration system is shown in Fig. 4.18. The Ni wire and

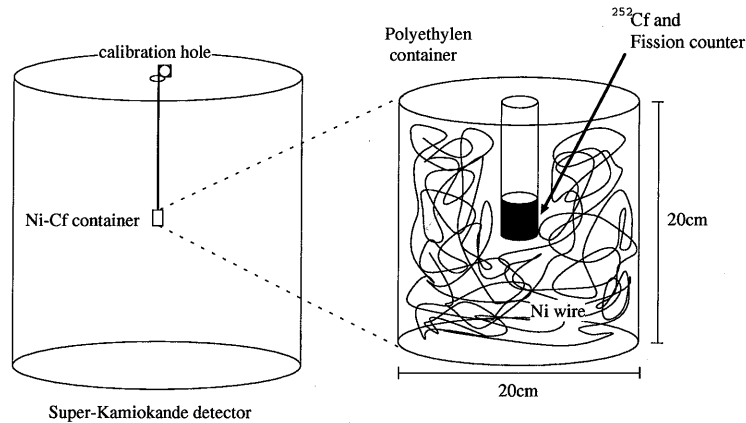


Figure 4.18: Schematic view of the calibration system with the radioactive Ni+²⁵²Cf source

²⁵²Cf source are packed in a cylindrical container(see Fig.4.18) which is made of polyethylene. This container is 20cm in height and 20cm in diameter. The ²⁵²Cf source(1.7 μ Ci) is located at the center of the container on which an electrode is painted to be used as a part of a proportional counter . The ²⁵²Cf source is surrounded by pure water and bundles of 0.1mm ϕ Ni wires with gross weight of 2.84 kg and pure water. This container is easily set up in the Super-Kamiokande water tank through calibration holes on the detector top and data are taken at various positions.

When one take data for energy calibration with Ni(n, γ)Ni* reactions, one use the preceding ²⁵²Cf fission as a trigger, which is called "fission trigger". The proportional counter is located inside of the container to detect ²⁵²Cf fission products. Its signal is used as the trigger. Data-taking processes are active only within 500 μ sec after each fission trigger. The distribution of time intervals(T_{diff}) measured from the fission trigger is shown in Fig.4.19. In order to subtract backgrounds in the energy spectrum, for example, 2.2 MeV γ -rays from the H(n, γ)D reaction, off-timing data($300 < T_{diff} < 500$) are subtracted from on-timing data ($10 < T_{diff} < 210$). After the background subtraction, the resultant energy spectrum is shown in Fig.4.20 As is seen in Fig.4.20, the width of the N_{eff} distribution is not well reproduced by our MC simulation. This difference will be treated as a systematic error. Then, Ni data have been taken at several positions(Fig.4.21) in the detector. With the data, our Monte Carlo simulation is pre-tuned. The position dependence of the energy scale is summarized in Table.4.3. The position dependence is measured only in the Ni calibration run Averaging the results given in Table.4.3, the possible difference in energy scale between the data and our MC simulation is estimated to be +0.3% for ⁸B solar neutrinos in the fiducial volume(22.5kton).

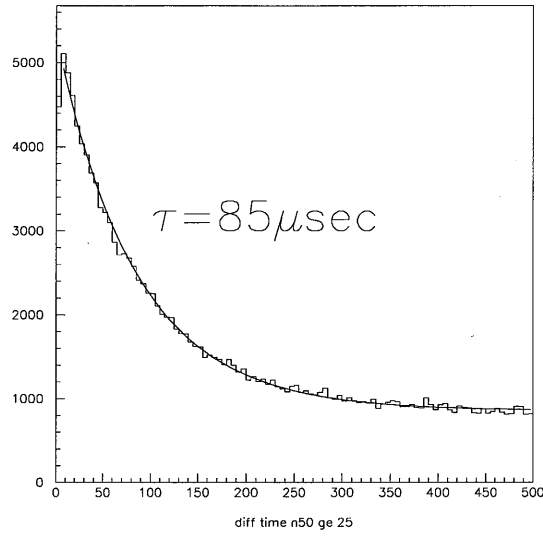


Figure 4.19: Event time distribution measured from the fission trigger. The time constant $\tau=85\mu\text{sec}$ corresponds to the neutron thermalization time in water.

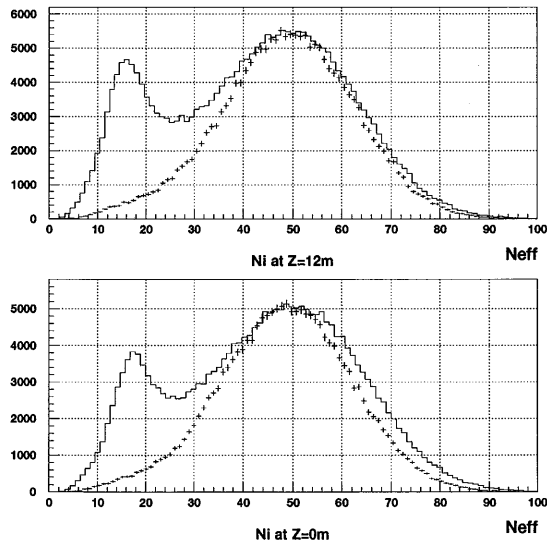


Figure 4.20: N_{eff} distribution for Ni data taken at $z=12\text{m}$ (upper) and at $z=0\text{m}$ (lower). In both figures, the solid histograms represent data and the crosses represent our MC simulation. One MeV is approximately equivalent to $7N_{eff}$.

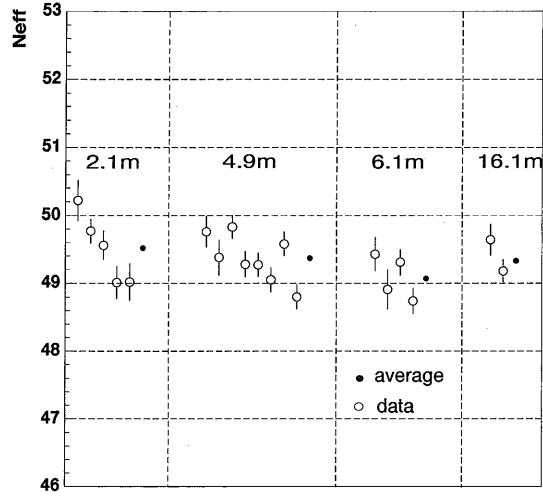


Figure 4.21: Position dependence of energy scale as measured by Ni data. Vertical axis is N_{eff} . Number inside of the graph indicate distance(D_{wall}) between the Ni position and the nearest detector wall. An open circle represents a peak position in the N_{eff} distribution obtained by a Ni data, and a filled circle indicates an averaged value at corresponding D_{wall} . These averaged values are summarized in Table.4.3

distance from wall[m]	N_{eff} of Ni data	N_{eff} of M.C.	M.C. - data Ni data
2.1	49.52	48.80	-1.4%
4.9	49.37	48.85	-1.1%
6.1	49.07	49.01	-0.1%
16.2	49.33	49.96	+1.0%
Position(x,y,z)[m]	N_{eff} (data)	N_{eff} (MC)	M.C. - data
(-12,0,+12)	49.49	49.49	$\pm 0.0\%$
(-12,0,+0)	50.33	49.19	+2.3%

Table 4.3: Position dependence of the energy scale obtained by Ni calibration runs

4.5.3 LINAC

In the calibration runs with γ -rays from the $\text{Ni}(n,\gamma)\text{Ni}^*$ reactions, the main one is the $^{58}\text{Ni}(n,\gamma)^{59}\text{Ni}^*$ reaction. For example, the individual branching ratios of a fraction(8.9%) of γ -rays from the reaction have not been measured. Therefore, it is difficult to deal with the fraction 8.9% in our MC simulation. Moreover, there are uncertainties in the γ -ray attenuation by material effect of the Ni wire as well as uncertainties in the cross section and branching ratios of $\text{Ni}(n,\gamma)\text{Ni}^*$. On the other hand, uncertainty in LINAC beam energy is only $\pm 0.3\%$ as will be explained in this section. Hence, we adopt LINAC calibration for the absolute energy scale and energy resolution determination.

A schematic view of LINAC is shown in Fig.4.22 and the whole calibration system is illustrated in Fig.4.23 LINAC emits electrons with kinetic energies of $5\text{MeV} \sim 15\text{MeV}$. Electrons

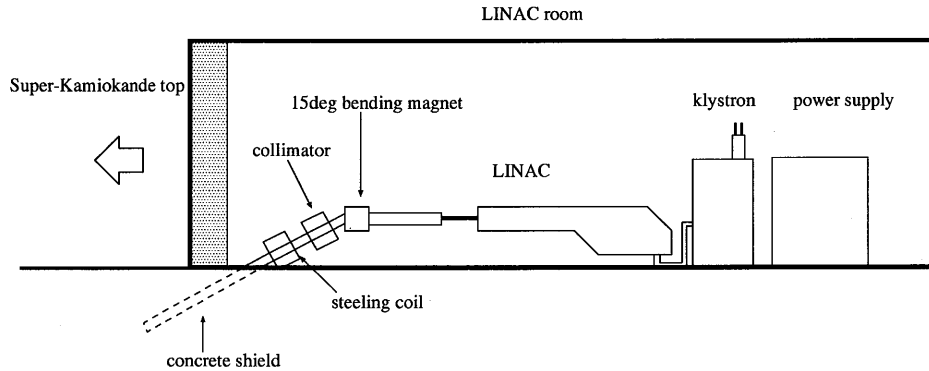


Figure 4.22: Schematic view of LINAC

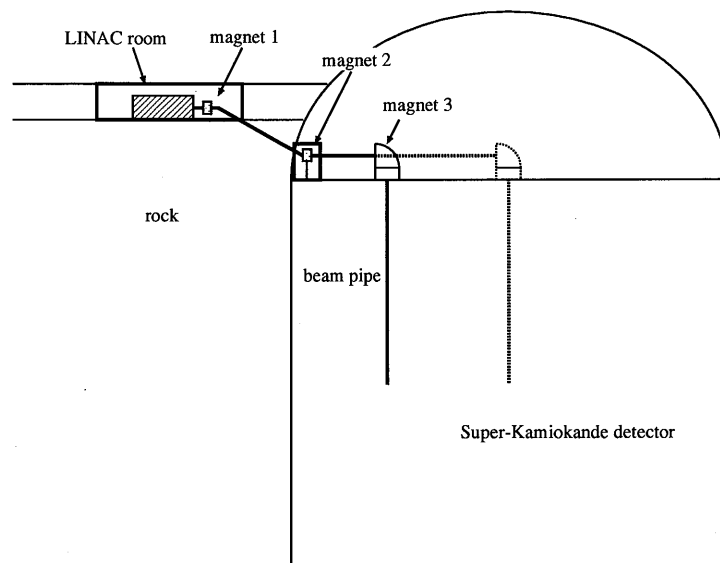


Figure 4.23: The whole LINAC calibration system

from LINAC are fed into the Super-Kamiokande water tank via beam pipe through 4 collimators and 3 bending magnets. After all the collimators, the intensity of the electron beam is reduced to a level of 1 electron/bunch. A schematic view around the beam pipe end is shown in Fig.4.24. Around the pipe end, there is a plastic scintillator with thickness of 1mm. By a signal detected

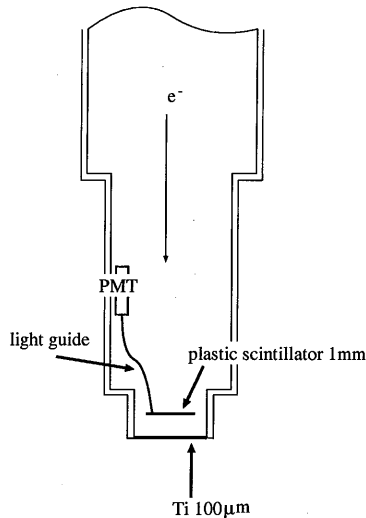


Figure 4.24: Around the end point of the LINAC beam pipe

by the scintillator together with a micro-wave beam timing signal from LINAC, a trigger signal is made. The end cap is a thin Ti window with thickness of $100\mu\text{m}$. It prevents water from sneaking into the beam pipe.

A Ge detector is used to calibrate the absolute energy scale of the LINAC beam momentum. A schematic view of this Ge calibration system is shown in Fig.4.25. Using this system, the beam momentum was measured in May and June, 1997. The deviation of the measured (by Ge) beam momentum from the expectation by the magnetic field of analyzing magnet ($d1$) is less than $\pm 0.3\%$ at various energies. The result is summarized in Table.4.4 and in Fig.4.26.

$d1[\text{A}]$	May		June	
	$B[\text{gauss}]$	$P_{beam}[\text{MeV}/c]$	$B[\text{gauss}]$	$P_{beam}[\text{MeV}/c]$
1.8	-371	5.120	-371	5.123
2.15	-437	6.054	-437	6.048
2.5	-504	6.964	-505	6.969
3.2	-637	8.811	-637	8.852
4.0	-789	10.949	-790	10.979
5.0	-980	13.630	-979	13.667
6.0	-1168	16.283	-1169	16.299

Table 4.4: LINAC electron Momentum vs Magnetic field

LINAC data have been taken at 2 positions; $(x,y,z)=(-1237,70.7,1228)[\text{cm}]$ and $(x,y,z)=(-1237,70.7,27)[\text{cm}]$ position (see Fig.4.23). Energy distributions of the real data and Ni-tuned

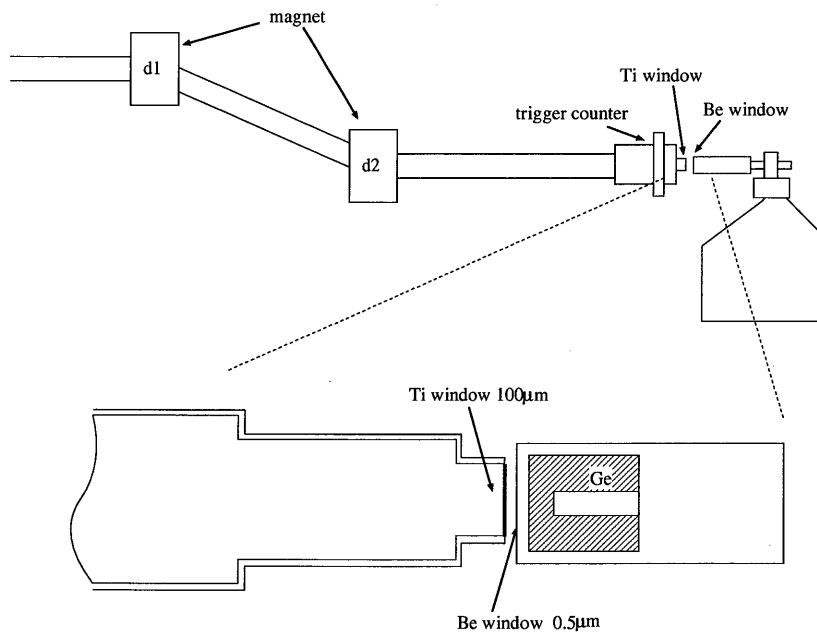


Figure 4.25: Schematic view of the Ge calibration system for the LINAC beam momentum

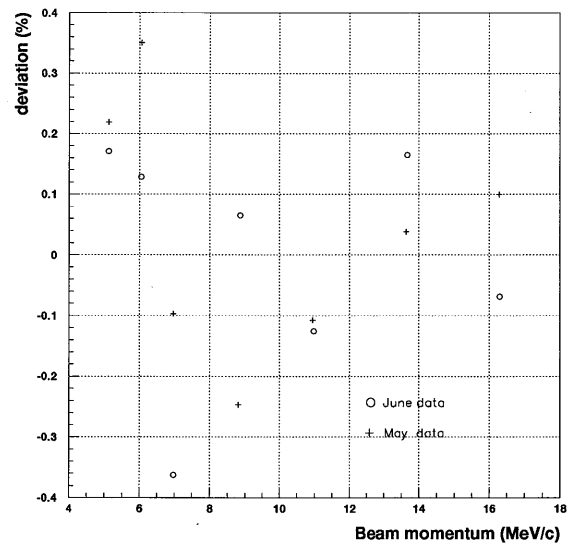


Figure 4.26: Deviation of the LINAC beam momentum from the momentum measured by the Ge calibration system.

MC at each position are shown in Fig.4.27. Comparisons are summarized in Fig.4.28. The

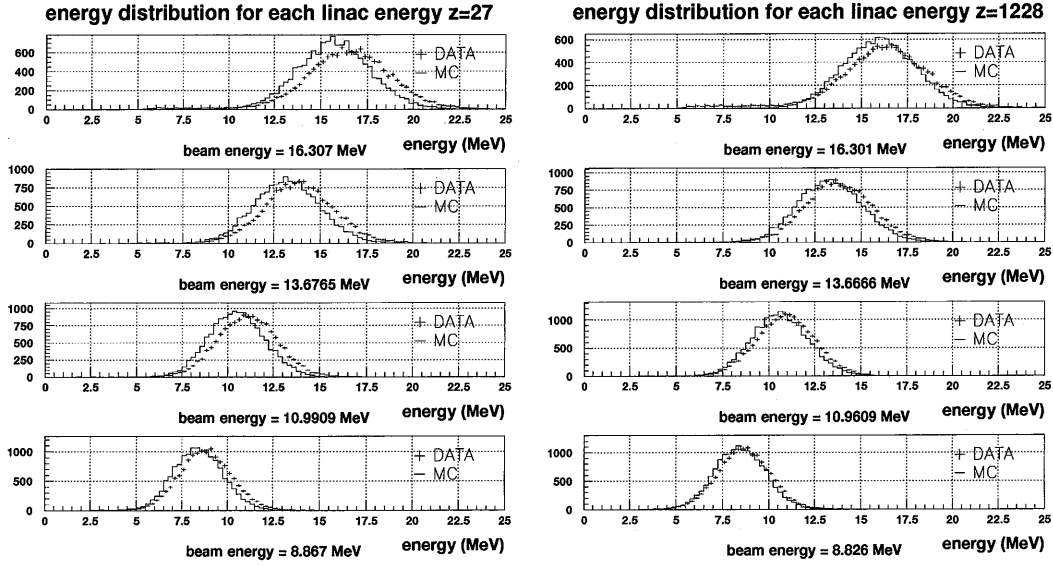


Figure 4.27: Energy distributions of LINAC data at Z=0m and 12m. Left(right) figures are energy distributions of LINAC data at $(x,y,z)=(-1237,70.7,1228)[\text{cm}]$ ($(-1237,70.7,27)[\text{cm}]$) together with Ni-tuned MC distribution.

average differences between the data and Ni-tuned MC in the absolute energy scale are +2.6% at $(x,y,z)=(-1237,70.7,1228)[\text{cm}]$ and +4.2% at $(x,y,z)=(-1237,70.7,27)[\text{cm}]$, respectively. On the other hand, the average differences of energy resolution between the LINAC data and Ni-tuned MC are 4.7% at $(x,y,z)=(-1237,70.7,27)[\text{cm}]$, and 2.6% at $(-1237,70.7,1228)[\text{cm}]$, respectively.

4.5.4 Comparison between Ni and LINAC

Absolute energy scale

Our MC simulation has already been pre-tuned with Ni calibration data. Therefore, a correction has to be made to our MC simulation, based on the LINAC energy scale calibration.

In this comparison, Ni data taken at the same position as LINAC data are used. The peak positions of the N_{eff} distributions of real data and MC are summarized in the lower two rows of Table.4.3. The differences between Ni data and Ni-tuned MC at the LINAC position are written in the third column, in the lower two rows of Table.4.3. Now, LINAC data are directly compared with Ni data at the same position. The result is

$$\left(\frac{data - MC}{MC}\right)_{LINAC} - \left(\frac{data - MC}{MC}\right)_{Ni} = \begin{cases} +2.6\% \pm 0.5\% & (\text{at } Z = +12m) \\ +1.9\% \pm 0.5\% & (\text{at } Z = 0m). \end{cases} \quad (4.9)$$

The average difference is +2.3% which should be a correction factor to Ni-tuned MC.

Position dependence

As is described in Section.4.5.2, the position dependence of energy scale is estimated to be +0.3% which should be included in Ni-tuned MC.

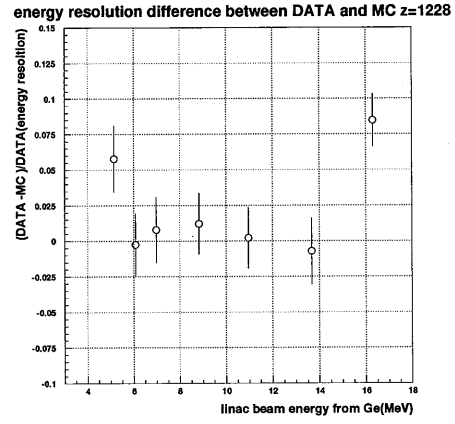
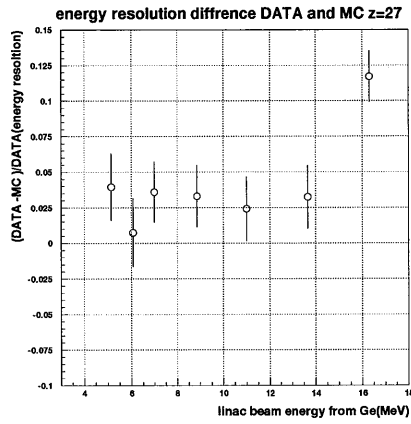
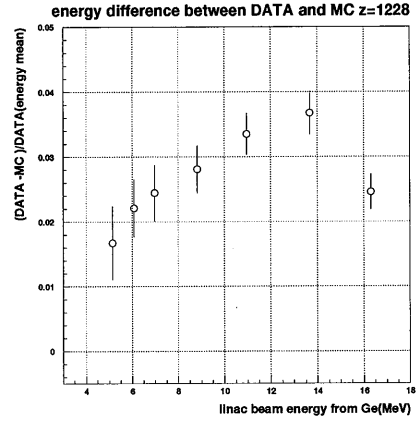
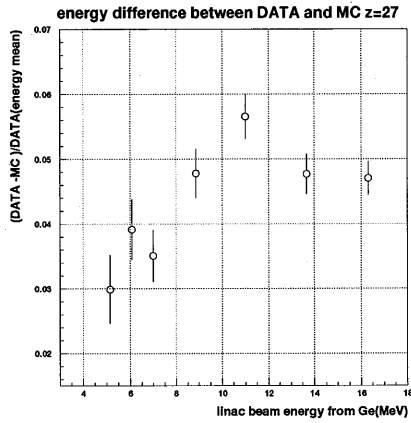


Figure 4.28: Comparison between LINAC data and Ni-tuned MC. $(\text{Data} - \text{Ni-tuned MC})/\text{Data}$ is plotted, as a function of LINAC beam energy calibrated by the Ge energy calibration system. Upper figures for the energy scale, and lower ones for the energy resolution. Left figures are for data at $(x,y,z)=(-1237,70.7,27)[\text{cm}]$, and right ones are for data at $(x,y,z)=(-1237,70.7,1228)[\text{cm}]$. The energy scale in LINAC data is calibrated by the Ge measurement. (Ni scale)

Summary

In summary, total systematic shift energy scale in Ni-tuned MC is estimated to be $+2.6\%$ ($= +2.3\%$ (Ni/LINAC difference) $+ 0.3\%$ (position dependence)). After this energy scale shift, the energy spectra obtained by LINAC data are shown in Fig.4.29. The deviation from MC is

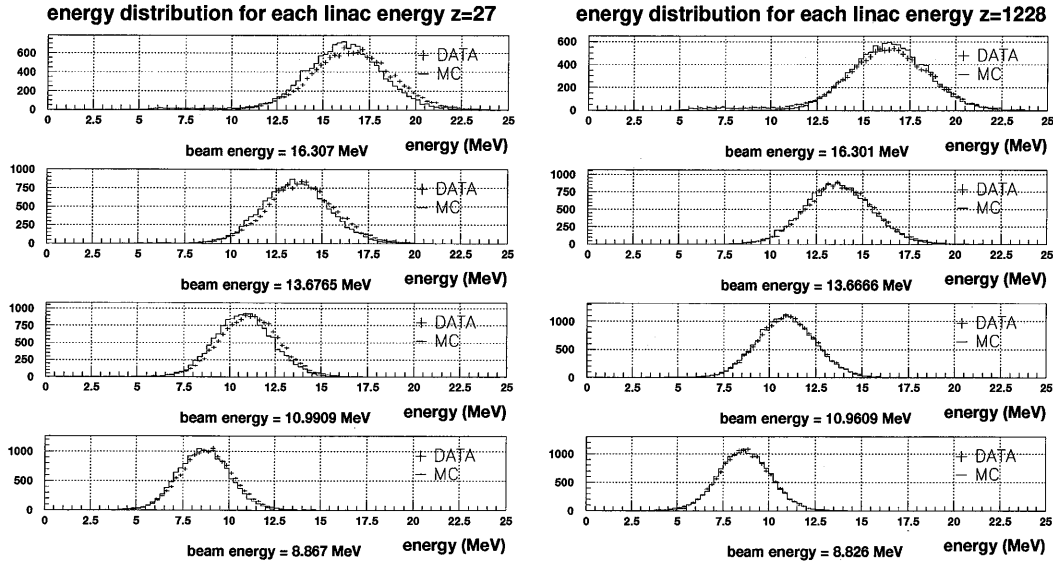


Figure 4.29: Energy distribution of LINAC at $Z=0\text{m}$ and 12m . Left(right) figures are energy distributions of LINAC data at $(x,y,z)=(-1237,70.7,1228)\text{[cm]}$ ($(-1237,70.7,27)\text{[cm]}$) together with LINAC-tuned MC distribution.

demonstrated in Fig.4.30. From now on, MC indicates the LINAC tuned MC if not specified. The systematic errors in absolute energy scale are summarized in Table.4.5. As described in

Error source	Error(%)
LINAC beam energy determination	0.3
variation of LINAC data	1.3
Position average	0.5
Ni vs LINAC comparison	0.3
total	1.5

Table 4.5: Possible sources of systematic errors in absolute energy scale. The total error is estimated by individual errors added in quadrature.

Table.4.5, the total systematic error is $\pm 1.5\%$. However, LINAC data have been taken only at two positions, so far while Ni data are taken at several positions. Hence, in this analysis, the systematic error in absolute energy scale is conservatively enlarged to cover the energy scale shift($+2.6\%$) from Ni-tuned MC the Ni data. Finally, the systematic error in energy scale becomes

$$\begin{array}{l} +4.1\% \\ -1.5\% \end{array} (\text{energy scale}) \implies \begin{array}{l} +9.9\% \\ -3.1\% \end{array} (\text{flux of } {}^8\text{B solar neutrino})$$

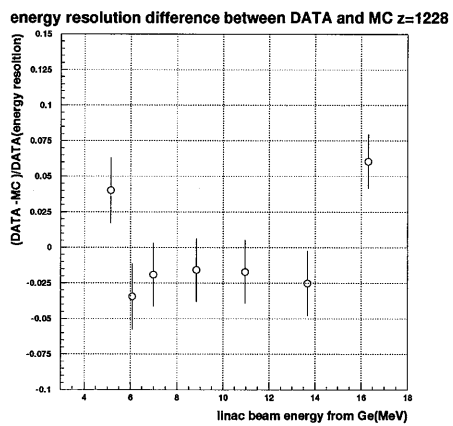
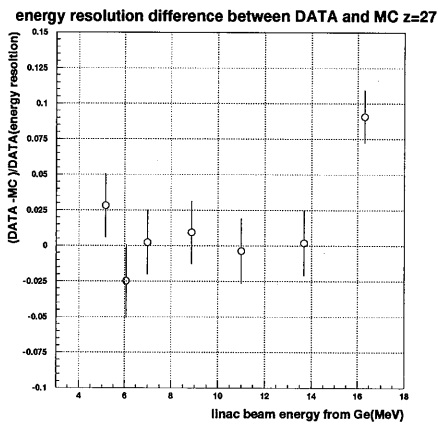
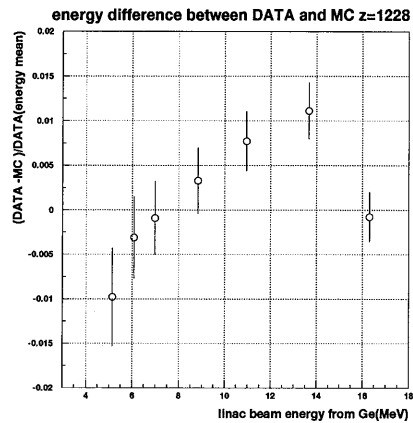
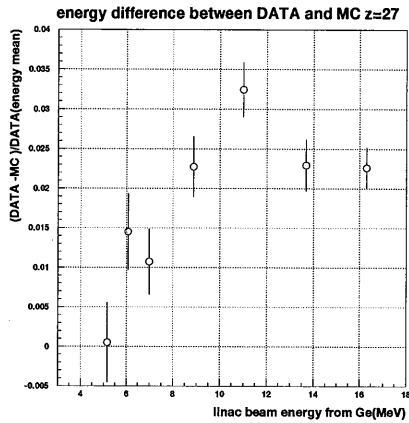


Figure 4.30: Comparison between LINAC data and MC after correcting the energy scale shift. $(Data - MC)/Data$ is plotted, as a function of LINAC beam energy calibrated by the Ge energy calibration system. Upper figures for the energy scale, and lower ones for the energy resolution. Left figures are for data at $(x,y,z)=(-1237,70.7,27)[cm]$ and right ones are for data at $(x,y,z)=(-1237,70.7,1228)[cm]$. The energy scale in LINAC data is calibrated by the Ge measurement.

The maximum deviation of energy resolution is 4.7%. It is conservatively employed in the systematic error. It should be noted this deviation is not corrected in our MC.

4.5.5 Long-term stability in energy scale measured by μ -decay electrons

The maximum energy of μ -decay electrons is about 53 MeV and the shape of the energy spectrum(Michel spectrum) is given by

$$\frac{dN}{dE_e} = \frac{G^2}{12\pi^3} m_\mu^2 E_e^2 \left(3 - \frac{4E_e}{m_\mu} \right), \quad \left(E_e \leq \frac{m_\mu}{2} \right) \quad (4.10)$$

In water, however approximately 20% of μ^- s are captured by ^{16}O nucleus. Hence, the visible mean life time of stopping μ^- decreases to 1.8 μsec [37]. Observed mean life time of muon in Super-Kamiokande is 2.02 μsec . Hence, the μ^+/μ^- ratio becomes 1.1 in Super-Kamiokande. Furthermore, the energy spectrum of μ^- decay electrons bound by ^{16}O is distorted [38]. With this effect taken into considerations, data of μ -decay electrons and MC events are compared.

In Fig.4.31, the N_{eff} distributions for data and MC are shown. The two spectra are con-

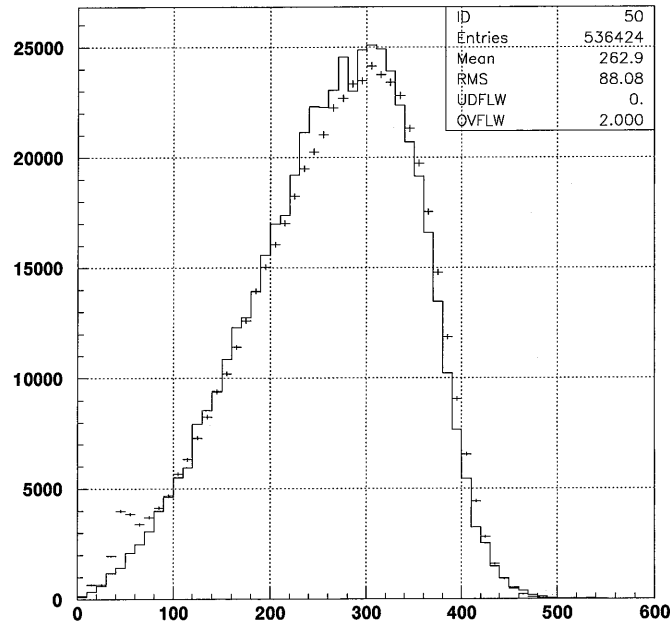


Figure 4.31: N_{eff} distributions of μ -decay electrons for data(crosses) and MC(solid histogram). The horizontal axis is N_{eff} and the vertical axis is number of events.

sistent with each other, excepting at a low-energy region. This difference is caused by γ -rays emitted from radioactive nuclei such as ^{16}N generated by μ^- capture by ^{16}O in water. The difference in peak position between the two spectra is

$$\frac{Data - MC}{MC} = +1.5\% \pm 0.2\% \quad (22.5kton \text{ fiducial volume })$$

The comparison is in good agreement with the LINAC calibration result within errors.

The long-term stability of energy scale is shown in Fig.4.32. Each point corresponds to 30-day data. The stability in energy scale is estimated to be $\sim \pm 0.5\%$.

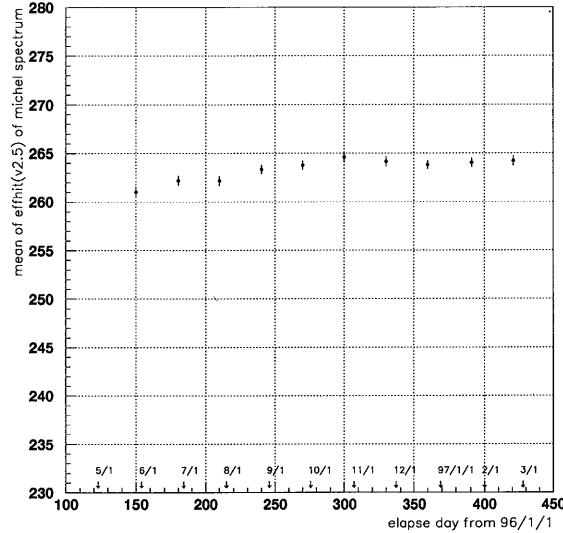


Figure 4.32: Long-term stability of energy scale. Each point corresponds to 30-day data.

4.5.6 Summary

The methods to calibrate the absolute energy scale and the energy resolution are summarized in Table.4.6. Then, the total systematic error is summarized as

Parameter	calibration source
Absolute energy scale	LINAC
Energy resolution	LINAC
Position variation	average of Ni
Time variation	decay electron

Table 4.6: Summary of the energy scale calibration methods

$$\text{energy scale} = \begin{matrix} +4.1\% \\ -1.5\% \end{matrix} \quad (4.11)$$

$$\text{energy resolution} = \begin{matrix} +4.7\% \\ -0\% \end{matrix} \quad (4.12)$$

Chapter 5

Data Reduction and Analysis

5.1 Data Set

Super-Kamiokande started taking data on the 1st of April in 1996. It took a while before the operating conditions have stabilized. In this thesis, the data taken from May 31, 1996 to Jun 23, 1997 are analyzed.

Prior to event reduction, bad-quality data sets are thrown away. For example, a PMT was continuously flashing, some data included noisy runs, and so on.

After good run selection, the detector live time in this analysis amounts to 306.3 days during which a total of 3×10^8 events are recorded.

5.2 Event Reduction

5.2.1 First reduction

After good run selection, the following selection criteria are applied to the data to reject background events, for example, cosmic-ray muons.

1. ID(Inner Detector) Total charge < 1000 p.e. – selected
:This is to reject high-energy events such as cosmic-ray muons.
2. ID Time difference from the preceding event $> 20 \mu\text{sec}$ – selected
:This is to reject electrons from μ -decay.
3. Event status cut
:This is to reject bad events due to bad hard-ware behavior like broken online system.
4. OD(Outer Detector) triggered event cut
:This is to reject events triggered by particles which come from outside of the detector.
5. OD hit < 20 hits – selected
:This is same as(but tighter than) 4
6. Noise event cut 1
:This is to reject noise events caused by PMT or electronics troubles.

7. Flasher PMT event cut

:This is to reject events caused by self-flashing PMTs.

Criterion 1 is to reject high-energy events. In Super-Kamiokande, almost all the high-energy events are cosmic-ray muons and they come into the inner detector at a rate of 2.2 Hz. As these events emit many Čerenkov photons, these events can be easily rejected (Fig.5.1). In this

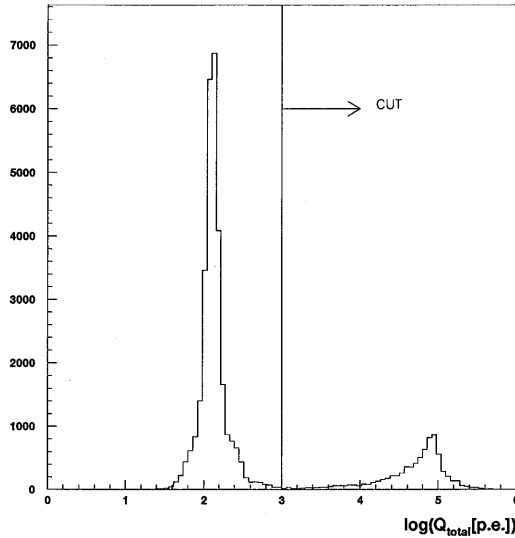


Figure 5.1: Total ID charge(in unit of photoelectrons)distribution of a typical raw data. The events of which ID charge are rejected.

analysis, threshold of total ID charge in an event is set to 1000 p.e. which is equivalent to about 200 MeV for electron events. Therefore this cut affects real ^8B solar neutrino events negligibly.

Criterion 2 is to reject electrons from μ -decay. This cut introduces a dead time of about $1.6 \times 10^{-4}\%$.

Criterion 3 is to reject pedestal events and ones which lacks in some DAQ information. The pedestal event was explained in Section.3.4.2. These events are rejected in this analysis. The dead time is calculated in an off-line conversion process “TQreal”(see Section.3.7) and it is subtracted in calculation of the detector live time.

Criteria 4 and 5 are to reject events caused by cosmic-ray invisible muons which come from outside of the detector, but leave a very small amount of energy deposit in the inner detector. Criterion 6 is to reject noise events. In this cut, a parameter NS-ratio defined by Eq.5.1 is introduced and the event which satisfies NS-ratio ≥ 0.4 is rejected.

$$NSratio \equiv \frac{N_{PMT}(-0.49 < Q_{PMT}[p.e.] < 0.49)}{N_{hit-PMT}} \quad (5.1)$$

Criterion 7 is to reject events caused by flasher PMTs. If there exist many hit PMTs around the largest-charged(hottest) PMT in an event, the event is cut as flasher PMT event. After these 7 criteria, the total number of events is reduced to 1.648×10^8 (reduction factor is

$1.648 \times 10^6 / 3 \times 10^6 = 55\%$). On the other hand, the detection efficiency for ^8B solar neutrino is 95%.

5.2.2 Second reduction

After the first reduction, vertex position and energy of each event is reconstructed. The method of vertex position reconstruction and of energy determination are described in Appendix.A and Appendix.F, respectively. If number of PMTs that are used in the vertex position reconstruction is too few, the result is not reliable. Therefore, in this analysis, one requires the following conditions;

8. Number of PMT used in the vertex position reconstruction ≥ 10 ($\sim 2\text{MeV}$) - selected
9. Goodness > 0.4 - selected

where the goodness is an estimator of the vertex position reconstruction. It is basically similar to χ^2 which is modified and bound from 0 to 1 as Eq.A.7 in Appendix.A. A typical *goodness* distribution is shown in Fig.5.2.

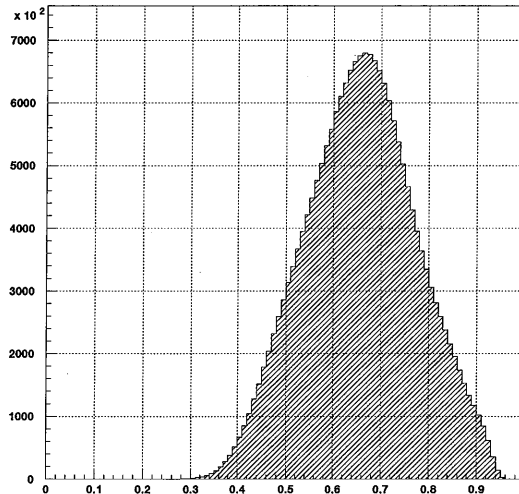


Figure 5.2: *goodness* distribution for raw data. The horizontal axis is *goodness*, and the vertical axis is the number of event in each bin.

After the 2 cuts above reduction, we apply pre-fiducial volume cut and pre-energy cut:

10. Distance between the vertex position and the nearest detector surface(D_{wall}) of $\text{ID} \geq 150$ cm & $N_{\text{eff}} \geq 36.46$ hits($\sim 5.3\text{MeV}$) - selected

where N_{eff} is a number of hit PMTs after corrections which are detailed in Appendix.F. The water transparency is fixed to 70m in this calculation. To the events satisfying the criterion 10, one applies:

11. Noise cut 2

This selection criterion uses 2 methods to reject noise events. One is to reject events with misfit vertex position. The other is to reject events with misfit direction. These methods are explained in Appendix.C.1 and C.2.

5.3 Final Sample

5.3.1 Spallation and γ -ray cuts

Spallation cut

After the 2nd reduction, “spallation cut” is applied. In Super-Kamiokande, cosmic-ray muons hit the detector at a rate of 2.2Hz. Some of them which are energetic enough to spall oxygen nuclei in water of the inner detector(ID), and occasionally generate radioactive isotopes. The events originating from their decays are called “spallation” event. The energy range of spallation events is up to 16MeV as listed in Table.5.1.

Isotope	$T_{1/2}$ (sec)	Decay mode	Kinetic energy(MeV)
${}^8_2\text{He}$	0.122	β^-	10.66+0.99(γ)
		β^-n	(11%)
${}^8_3\text{Li}$	0.84	β^-	12.5~13
${}^8_5\text{B}$	0.77	β^+	13.73
${}^9_3\text{Li}$	0.178	β^-	13.5(75%)
			11.0+2.5(γ)(25%)
		β^-n	~10(35%)
${}^9_6\text{C}$	0.127	β^+p	3~13
${}^{11}_3\text{Li}$	0.0085	β^-	20.77(31%)
		β^-n	~16(61%)
${}^{11}_4\text{Be}$	13.8	β^-	11.48(61%)
			9.32+2.1(γ)(29%)
${}^{12}_4\text{Be}$	0.0114	β^-	11.66
${}^{12}_5\text{B}$	0.0203	β^-	13.37
${}^{12}_7\text{N}$	0.0110	β^+	16.38
${}^{13}_5\text{B}$	0.0173	β^-	13.42
${}^{13}_8\text{O}$	0.0090	β^+p	8~14
${}^{14}_5\text{B}$	0.0161	β^-	14.07+6.09(γ)
${}^{15}_6\text{C}$	2.449	β^-	9.82(32%)
			4.51+5.30(γ)(68%)
${}^{16}_6\text{C}$	0.7478	β^-n	~4
${}^{16}_7\text{N}$	7.134	β^-	10.44(26%)
			4.27+6.13(γ)(68%)

Table 5.1: List of radioactive isotopes which decay accompanied with β and/or γ -rays of with energies greater than 6.5MeV

A spallation event has a strong spatial and time correlation with the parent muon. Therefore, a likelihood function is introduced as a product of 3 probability functions: 1) time difference

between muon and low-energy event, 2) distance between muon track and low-energy event and 3) extra charge¹ of muon. The method to determine these probability functions is described in Appendix.E.

The cut value in the likelihood function is determined by comparing the low-energy events before the spallation cut with very low energy events($\sim 5\text{MeV}$) sample which are supposed to be β -rays from ^{214}Bi decay uncorrelated with cosmic-ray muons. Then, the dead time due to the spallation cut for ^8B solar neutrinos is estimated to be 20%. The reduction factor of this cut is $743517/1.298 \times 10^6 = 76\%$. The detail of the spallation cut is described in Appendix.E.

Fiducial volume and energy cut

After the spallation cut, then one applies fiducial volume cut and energy cut. The requirement for fiducial volume cut:

Distance between the vertex position and the nearest detector surface(D_{wall}) ≥ 200 cm - selected

The final fiducial volume is about 22.5kton. The requirement for energy cut is :

$$"6.5 \leq E_{e,\text{recoil}} \leq 20 \text{ MeV}"$$

The events satisfying the criteria above are selected. The lower energy threshold of 6.5MeV is employed, because the number of events rapidly increases below 6.5MeV. And the trigger efficiency curve(Fig.3.20) is well reproduced between data and our MC simulation above 6.5MeV. Therefore, the events with energies $\geq 6.5\text{MeV}$ are analyzed. The higher energy bound depends on the end point energy of ^8B solar neutrinos ($\sim 16\text{MeV}$) and the finite detector energy resolution(13% at 16MeV). Therefore, some margin from 16MeV being taken into account, it is set at 20 MeV.

γ -ray cut

Finally, " γ -ray cut" is applied. A characteristic of γ -ray events is their direction. As their source is supposed to be detector materials(the PMTs) and/or the rock surrounding the detector, their direction has a tendency to point inward in the detector(as shown in Fig.5.3, the z-direction distribution is distorted.) Hence, in order to cut them, "*effective distance*" from the inner surface of the detector(D_{eff}) is introduced. The definition of "*effective distance*" is shown in Fig.5.4, where the method to reconstruct event direction is described in Appendix.B. The D_{eff} distributions for the events before γ -ray cut and ^8B solar neutrino MC events are shown in Fig.5.5. Then, in this analysis, events with "*effective distance*" < 4.5 m are rejected. After this rejection, the vertex and direction distribution become flat in the detector coordinates as shown in Fig.5.6.

Subsequently, the reduction factor is estimated for the data as well as for ^8B solar neutrino MC events, as summarized in Table.5.2. From this result, it turns out that the S/N in the data is improved, while the signal loss caused by the γ -ray cut is small.

¹standard ionization loss subtracted

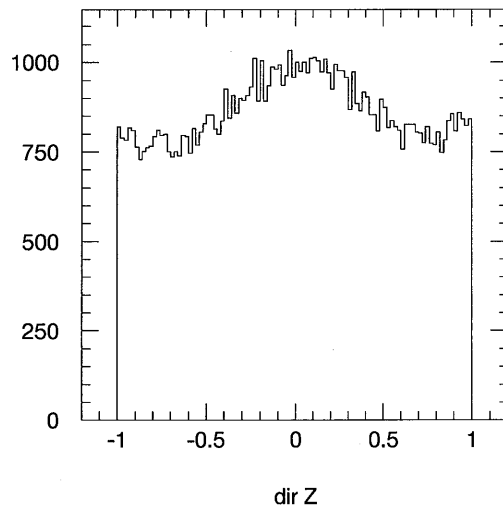


Figure 5.3: Zenith angle distribution of the events before γ -ray cut

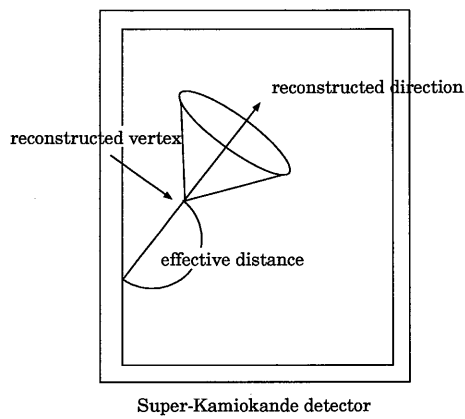


Figure 5.4: Definition of effective distance

Energy region	Real data	$^8\text{B } \nu$ MC
6.5 - 7.0 MeV	56%	92.2 %
6.5 - 20.0 MeV	70%	92.2 %

Table 5.2: Reduction factor of γ -ray cut

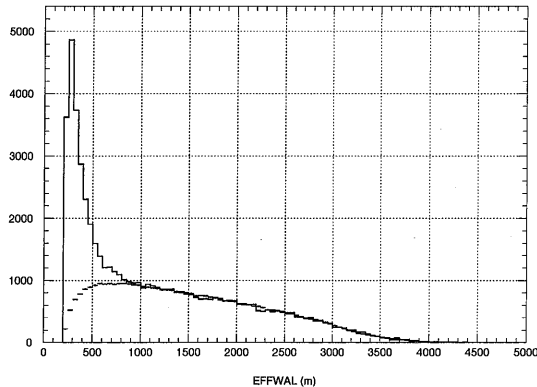


Figure 5.5: D_{eff} distributions for the events before γ -ray cut(solid histograms) and for ^8B solar neutrino MC events(crosses).

Final sample

Finally, a data set of 59953 events which survive after the γ -ray cut will be hereafter called the final sample.

5.3.2 Summary

The whole event reduction steps are summarized in Fig.5.7. In order to estimate the reduction factors for ^8B solar neutrino events, the same event reduction programs are applied to MC-generated ^8B solar neutrino events. In Fig.5.7, remaining number of events is shown at each reduction step for both data and MC in parenthesis. In our MC simulation, neutrinos are generated, assuming the ^8B β -decay energy spectrum(Fig.2.3)[9]. To reduce time-dependent systematic uncertainties(such as change in water transparency), events are generated in the same conditions that the real data are taken. Finally, 59953 events remain in the final sample, and study of ^8B solar neutrinos is done with this final sample.

The detection efficiency for ^8B solar neutrino events above 6.5MeV in the fiducial volume(22.5kton) is estimated to be 70% by our MC simulation.

5.4 Remaining Background

In Fig.5.8, the energy spectrum at each reduction step , together with a theoretical prediction by the SSM(BP95[9])is shown. As shown in this figure, there are many background events in the final sample. The remaining backgrounds are estimated to be; the radioactivities in the detector water, remaining spallation events, and remaining γ -rays from the PMTs and the rock surrounding the detector. The method to extract the ^8B solar neutrino signal will be explained in Section.6.1

In Fig.5.8, the number of events increases rapidly below 6.5MeV. This is caused by a low-energy background source. The radioactivities in the water dominate below 6.5MeV. In Super-Kamiokande, the dominant radioactivities are caused by β -decay of ^{214}Bi (end point energy = 3.26MeV) originating from ^{222}Rn which somehow sneaks into the detector water. The end

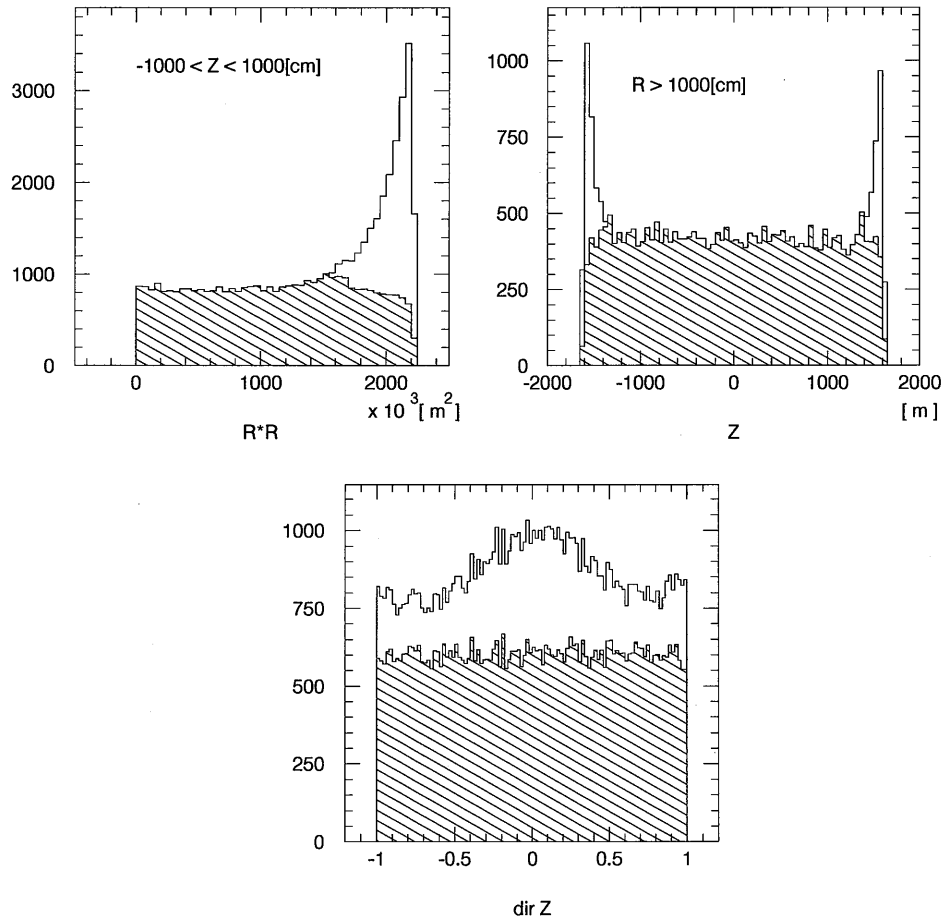


Figure 5.6: Vertex and direction distribution of the events before and after γ -ray cut. Solid figures represent the distributions before γ -ray cut and hatched ones represent the distributions after γ -ray cut. Upper figures are vertex distributions for $R \cdot R = x^2 + y^2$ and for z measured in the detector coordinates. Lower figure is a zenith angle distribution before and after γ -ray cut.

Data: May 31, 1996 ~ June 23, 1997

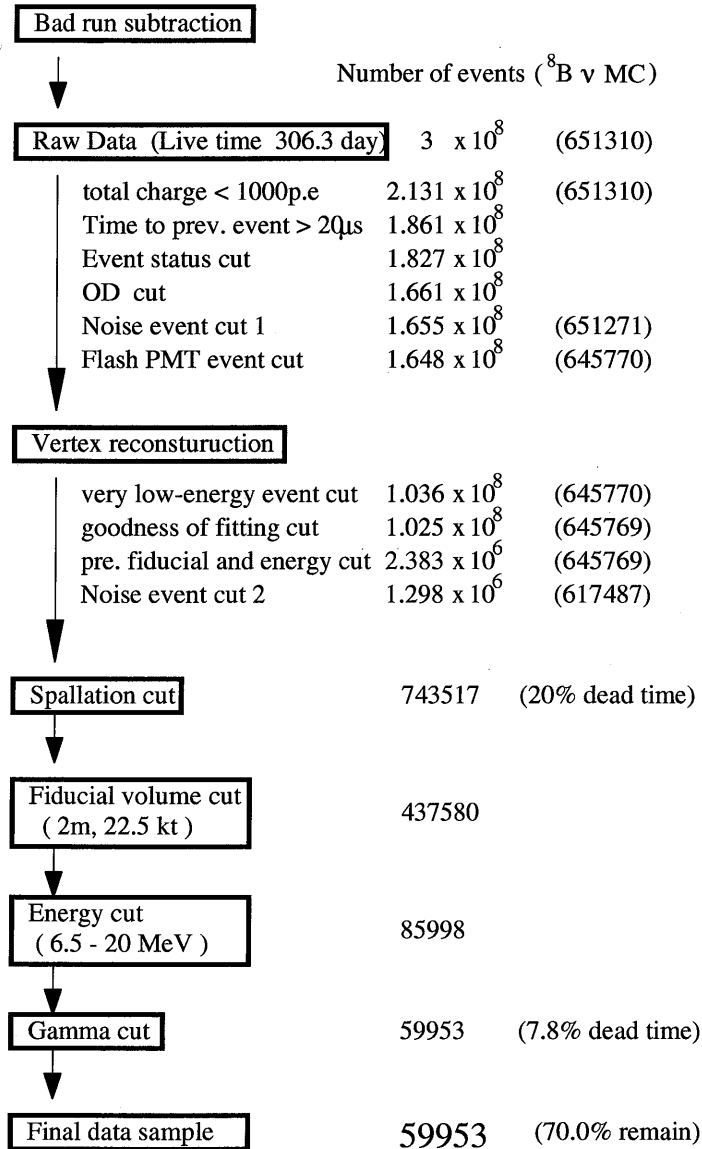


Figure 5.7: Summary of event reduction. The numbers in the parenthesis are for MC ⁸B solar neutrino events(~ 5year) which have survived after fiducial volume and energy cuts.

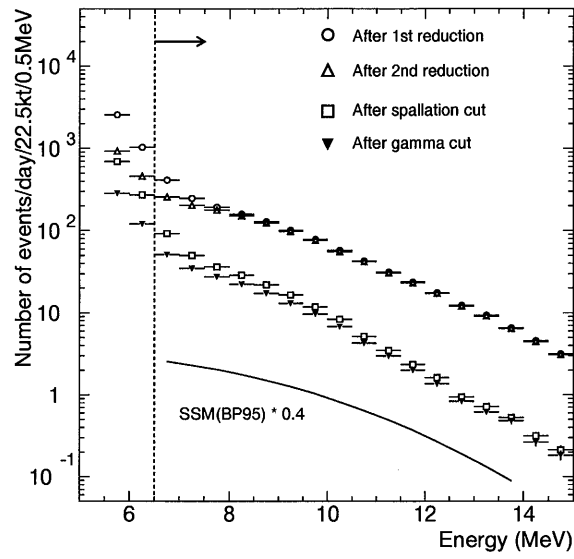


Figure 5.8: Energy Spectrum at each reduction step. The solid line represents the expected from the $SSM(BP95[9]) \times 0.4$.

point energy is actually lower than the energy threshold, however, it is smeared due to the finite detector energy resolution.

Chapter 6

Results

6.1 Extraction of Solar Neutrino Signal

After data reduction which is explained in Chapter.5, there still remain many background events. The next step is to extract a solar neutrino signal from the final data sample.

In Super-Kamiokande, recoil electrons from $\nu e \rightarrow \nu e$ elastic scattering is detected as described in Section 2.4. The direction of the recoil electron has a strong directional correlation with incident direction of the parent ${}^8\text{B}$ solar neutrino. The angle between the solar direction and the scattered electron direction is defined as " θ_{sun} " (Fig.6.1), and the expected $\cos \theta_{sun}$ distribution of ${}^8\text{B}$ solar neutrino events is shown in Fig.6.2.

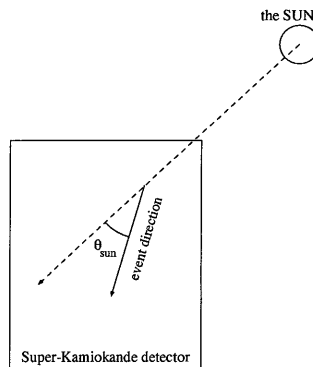


Figure 6.1: Definition of θ_{sun}

As the background events in the final sample come from radioactivities in the detector water, radioactive spallation products, and γ -rays from the rock surrounding the detector, their $\cos \theta_{sun}$ distribution are expected to be isotropic in the first approximation. .

In order to extract ${}^8\text{B}$ solar neutrino events from the final data sample, this difference in a $\cos \theta_{sun}$ distribution is used. Figure 6.3 shows a $\cos \theta_{sun}$ distribution of the final data sample. A clear peak is observed in the direction of the Sun ($\cos \theta_{sun} = 1$), while the background events distribute uniformly. Thus, one can obtain number of ${}^8\text{B}$ solar neutrino events by fitting the data, assuming signal(Fig.6.2) plus background.

In this fitting, a maximum likelihood method is used. The probability function for the likeli-

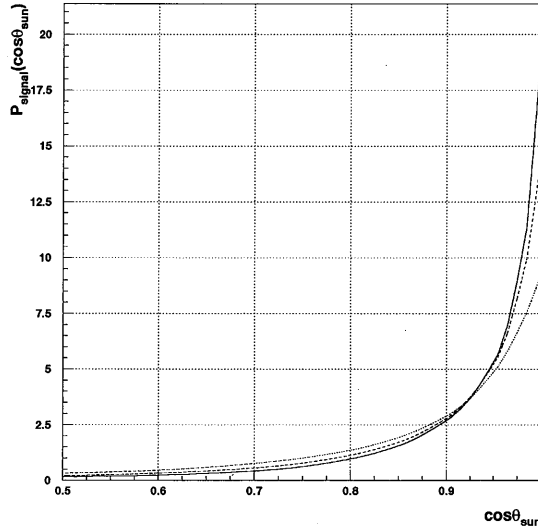


Figure 6.2: Expected $\cos \theta_{sun}$ distribution ($P_{s.g.}(E_e, \cos \theta_{sun})$) of recoil electron. The solid, dashed, and dotted lines represent 14, 10 and 7 MeV electrons, respectively. Each function is normalized to one when integrated over $-1 < \cos \theta_{sun} < 1$.

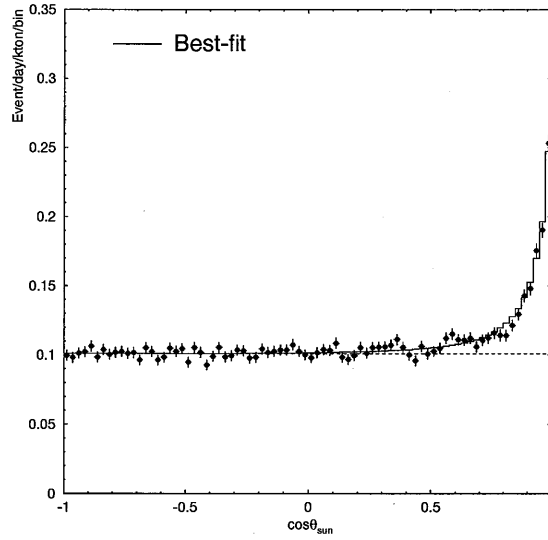


Figure 6.3: $\cos \theta_{sun}$ distribution of the final data(dots) sample with the best fit solid histograms($6.5 \leq E_e \leq 20$ MeV). The dashed line indicates the background level.

hood consists of both signal and background parts, which are functions of recoil electron energy E_e and $\cos \theta_{sun}$. The probability function for the signal part shown in Fig.6.2, $P_{s.g.}(E_e, \cos \theta_{sun})$, is derived from our MC simulation based on the standard solar model(SSM) of Bahcall and Pinsonneault(BP95)[9]. The MC simulator also includes detector response as well as propagation of the recoil electron in the water and of the resultant Čerenkov photons.

Probability function for the background part, $P_{b.g.}(E_e, \cos \theta_{sun})$ depends on the shape of background distribution. If the distribution of the background is perfectly isotropic, the $\cos \theta_{sun}$ distribution for the background part should be flat. Yet, there might be possible anisotropy in the background shape. Hence, one adopts a more conservative approach. The background shape is fit in the off-signal region with a 4th-degree polynomial in 3 different energy regions separately : 6 to 7 MeV, 7 to 10 MeV and 10 to 20 MeV. Systematic errors originating from the non-flat background estimation are summarized in Table.6.1.

In order to obtain the number of 8B solar neutrino events, the final sample is fit with a combination of these probability functions;

$$P(E_e, \cos \theta_{sun}, \alpha) = \alpha \times P_{s.g.}(E_e, \cos \theta_{sun}) + (1 - \alpha) \times P_{b.g.}(E_e, \cos \theta_{sun}) \quad (6.1)$$

where α is the fraction of 8B solar neutrino events in the final data sample which is to be derived by the maximum likelihood method.

It should be noted that the parameter α depends on E_e , because the ratio of signal to background(S/N ratio) is a function of E_e . Hence, the probability function is calculated for the 16 E_e regions, where the bin size is 0.5MeV in the 6.5~14MeV region and 6MeV in the 14~20MeV region. Then, the definition of the probability function in Eq.6.1 is modified as

$$P_i(\cos \theta_{sun}, \alpha) = \alpha_i \times P_{s.g.,i}(\cos \theta_{sun}) + (1 - \alpha_i) \times P_{b.g.,i}(\cos \theta_{sun}) \quad (6.2)$$

$$\alpha_i = \alpha \times \frac{N_{all}^{Data}}{N_i^{Data}} \times \frac{N_i^{MC}}{N_{all}^{MC}} \quad (6.3)$$

where N_i is the number of events in the i -th E_e bin, N_{all} is the total number of events(= $\sum_i^{N_{ene}} N_i$), N_{ene} (=16 in this analysis) is the number of E_e bins, and superscript Data and MC represent the final sample and 8B solar neutrino Monte Carlo events, respectively.

The likelihood function is defined by

$$L(\alpha) = \prod_i^{N_{ene}} \prod_j^{N_i} P_{j,i}(\cos \theta_{sun}, \alpha) \quad (6.4)$$

Figure 6.4 shows the $L(\alpha)$ distribution of the final sample. A value α_{max} which maximizes $L(\alpha)$ is calculated. Then, the number of 8B solar neutrino events($N_{sB\nu}^{Data}$) is:

$$N_{sB\nu}^{Data} = \alpha_{max} \times N_{all}^{Data} = 4395 \quad (6.5)$$

6.2 Solar Neutrino Flux

Based on the method detailed in Section.6.1, the 8B solar neutrino signal is extracted as shown in Fig.6.3. During 306.3 detector live days, the number($N_{sB\nu}^{Data}$) of observed electrons($6.5 \leq E_e \leq 20\text{MeV}$) scattered by 8B solar neutrinos in the 22.5kton fiducial volume is:

$$N_{sB\nu}^{Data} = 4395 \begin{matrix} +114 \\ -108 \end{matrix} (stat.) \begin{matrix} +444 \\ -154 \end{matrix} (syst.) \quad (6.6)$$

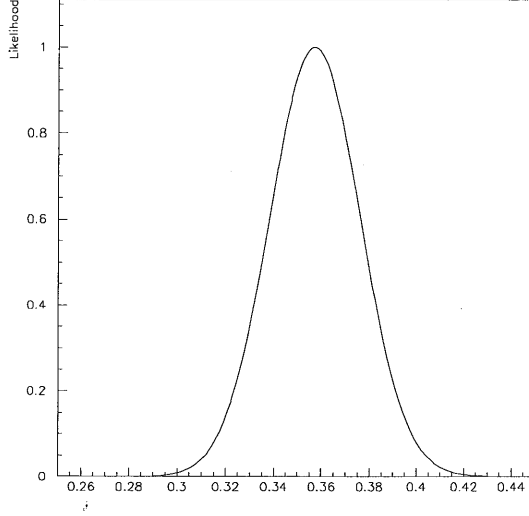


Figure 6.4: The likelihood distribution of final sample. Horizontal axis represents α , and vertical axis represents likelihood.

where *stat.* stands for a statistical error and *syst.* for a total systematic error. Individual systematic errors will be discussed later in Section.6.5.

This number corresponds to ${}^8\text{B}$ solar neutrino flux ($\phi_{8B\nu}^{Data}$) of

$$\phi_{8B\nu}^{Data} = 2.44 \begin{matrix} +0.06 \\ -0.06 \end{matrix} (stat.) \begin{matrix} +0.25 \\ -0.09 \end{matrix} (syst.) [\times 10^6 \text{ cm}^{-2} \text{ s}^{-1}] \quad (6.7)$$

which should be compared with the theoretical flux ($\phi_{8B\nu}^{SSM_{BP95}}$) by SSM[9]

$$\phi_{8B\nu}^{SSM_{BP95}} = 6.62 \begin{matrix} +0.93 \\ -1.12 \end{matrix} (theo.) \quad (6.8)$$

Then, the ratio of the observed flux to SSM prediction[9] is

$$\frac{\phi_{8B\nu}^{Data}}{\phi_{8\nu}^{SSM_{BP95}}} = 0.368 \begin{matrix} +0.010 \\ -0.009 \end{matrix} (stat.) \begin{matrix} +0.037 \\ -0.013 \end{matrix} (syst.) \begin{matrix} +0.062 \\ -0.052 \end{matrix} (theo.) \quad (6.9)$$

If one sets a higher analysis threshold energy, e.g, 7MeV, the results above will change to

$$N_{8B\nu}^{Data} = 3696 \begin{matrix} +102 \\ -97 \end{matrix} (stat.) \begin{matrix} +373 \\ -140 \end{matrix} (syst.) \quad (6.10)$$

$$\phi_{8B\nu}^{Data} = 2.45 \begin{matrix} +0.07 \\ -0.06 \end{matrix} (stat.) \begin{matrix} +0.25 \\ -0.09 \end{matrix} (syst.) \times 10^6 \text{ cm}^{-2} \text{ s}^{-1} \quad (6.11)$$

$$\frac{\phi_{8B\nu}^{Data}}{\phi_{8\nu}^{SSM_{BP95}}} = 0.371 \begin{matrix} +0.010 \\ -0.010 \end{matrix} (stat.) \begin{matrix} +0.037 \\ -0.014 \end{matrix} (syst.) \begin{matrix} +0.062 \\ -0.052 \end{matrix} (theo.) \quad (6.12)$$

They are consistent with those for 6.5 ~ 20.0MeV. The deficit in the ${}^8\text{B}$ solar neutrino flux is confirmed. It should be stressed that the measured ${}^8\text{B}$ solar neutrino flux is consistent with the Kamiokande-II+III result ($E_e \geq 7\text{MeV}$) of $2.80 \pm 0.19(stat.) \pm 0.33(syst.) [\times 10^6 \text{ cm}^{-2} \text{ s}^{-1}]$ within 1σ .

6.3 Day-Night Variation of Solar Neutrino Flux

As described in Section.2.3.2, one of advantages of the Super-Kamiokande detector is real-time measurement of the ^8B solar neutrino signal. Hence, one can investigate time variation of the neutrino flux. When the MSW effect(see Section.2.3.2) is considered, the neutrino oscillation probability of ^8B solar neutrinos depends on path length and electron density profile of the medium which the neutrinos go through. Therefore, regeneration of ^8B solar neutrinos by the MSW effect in the Earth is predicted(see Fig.6.5).

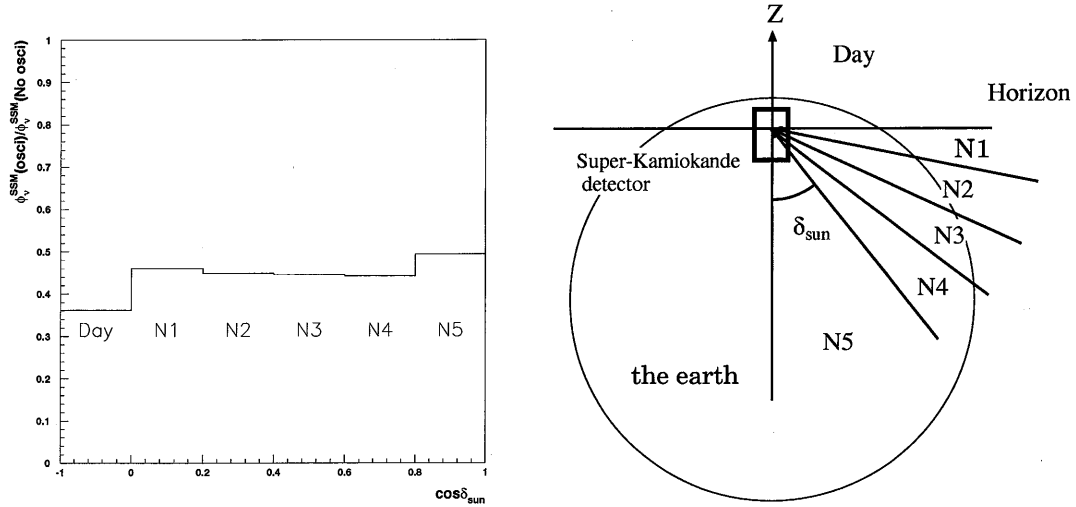


Figure 6.5: Expected day/night ^8B solar neutrino flux variation, assuming $\sin^2 2\theta=0.631$, $\Delta m^2=1.0 \times 10^{-5}$, respectively. The right figure depicts the definition of Day and N₁-N₅ in the left figure. The definition of δ_{sun} is described in Fig.2.17.

A possible day-night variation in the ^8B solar neutrino flux would be free of various systematic errors, e.g., solar model dependence, energy scale ambiguity, long-term gain stability of the detector, etc.

In this analysis, the data are divided into daytime(149.8 days) and nighttime(156.5 days) samples. The daytime or nighttime samples are taken while the Sun is above or below the horizon. In Fig.6.6, $\cos\theta_{sun}$ distributions ($6.5 \leq E_e \leq 20\text{MeV}$) for the daytime and nighttime samples are shown. After the background subtraction (see Section.6.1), the daytime flux ($\phi_{sB\nu}^{Day Data}$) and the nighttime flux ($\phi_{sB\nu}^{Night Data}$) are measured to be;

$$\phi_{sB\nu}^{Day Data} = 2.40 \pm 0.09(stat.) \begin{matrix} +0.24 \\ -0.08 \end{matrix} (sys.) [\times 10^6 cm^{-2}s^{-1}] \quad (6.13)$$

$$\phi_{sB\nu}^{Night Data} = 2.48 \pm 0.09(stat.) \begin{matrix} +0.25 \\ -0.09 \end{matrix} (sys.) [\times 10^6 cm^{-2}s^{-1}] \quad (6.14)$$

The difference between them is:

$$\frac{Day - Night}{Day + Night} = -0.017 \pm 0.026(stat.) \pm 0.017(sys.) \quad (6.15)$$

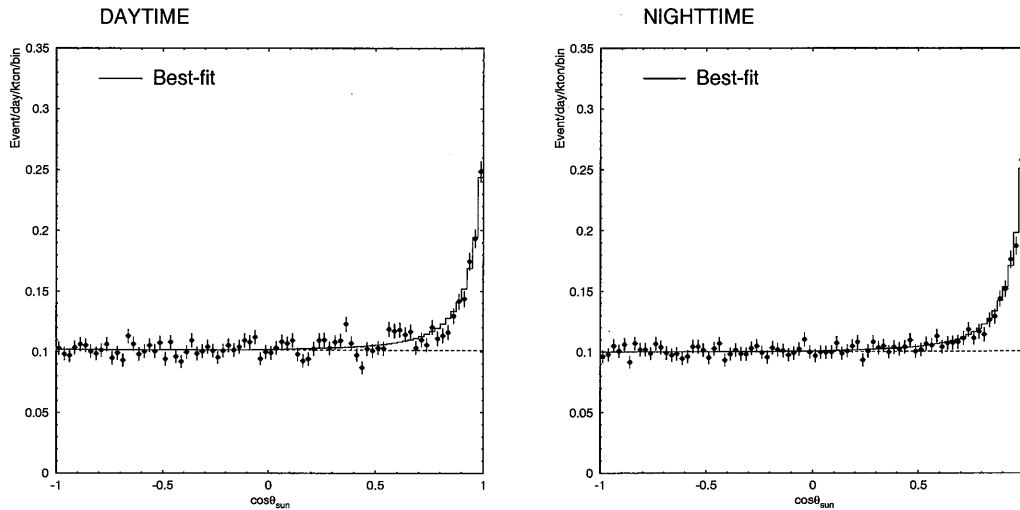


Figure 6.6: $\cos\theta_{sun}$ distribution of daytime data(left) and nighttime data(right) which correspond to 149.8 and 156.5 days, respectively. $6.5 \leq E_e \leq 20 \text{ MeV}$ and the fiducial volume is 22.5kton.

The quoted systematic error in Eq.6.15 specific to the dayh/night flux ratio will be discussed in Section.6.5. This result indicates that there has been no significant Day/Night difference in the ^8B solar neutrino flux so far.

Furthermore, the nighttime sample is divided into 5 sub-samples (N_1 - N_5 , see Fig.6.5 for definition). The $\cos\theta_{sun}$ distributions of N_1 - N_5 sub-sample are shown in Fig.6.7. Then the flux of each sub-sample is shown in Fig.6.8. There is no evidence for a possible day-night variation in the ^8B solar neutrino flux. The implication in Fig.6.8, as regards the MSW effect, will be discussed in the next chapter.

6.4 Energy Spectrum of Solar Neutrinos

Another advantage of Super-Kamiokande is that the energies(E_e) of recoil electrons scattered by ^8B solar neutrinos can be measured, as is described in Section.2.4. Since the MSW effect is dependent on neutrino energies, a possible distortion might be observed in the energy spectrum of recoil electrons scattered by them. A study of energy spectrum shape of recoil electrons provides a good test for the MSW effect independent of solar models. For example, in Fig.6.9, a distorted as well as reduced energy spectrum by the MSW effect is shown.

In this analysis, the final data sample is divided into 16 subsamples in the E_e distribution. The bin size is 0.5 MeV in the 6.5 ~ 14.0 MeV region, and 6 MeV in the 14.0 ~ 20.0 MeV region, respectively. Then, the ^8B solar neutrino is extracted bin by bin and, the measured energy spectrum of recoil electrons is shown in Fig.6.10. The error bars include both statistical and systematic ones, and the black thick bar represents correlated systematic error which comes from uncertainties in absolute energy scale and energy resolution(see Table.6.1). The statistical and systematic errors are still too large to draw any definite conclusion from the figure. The implication of the observed energy spectrum to the MSW effect will be discussed in the next chapter.

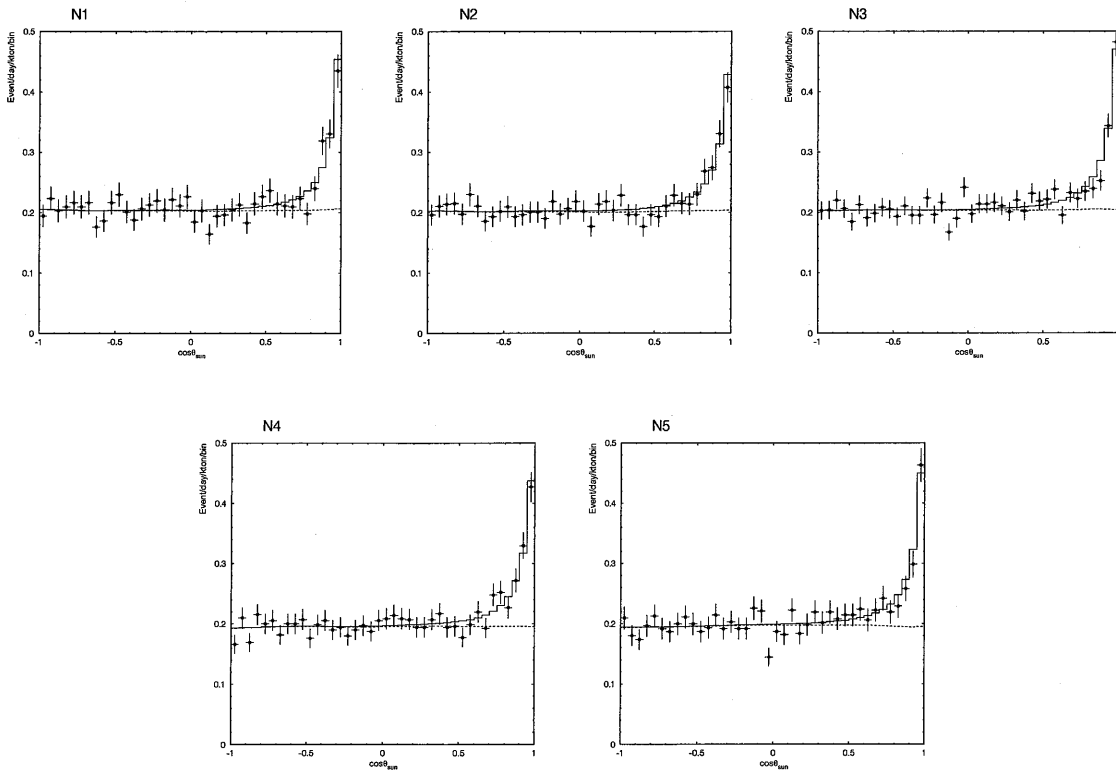


Figure 6.7: $\cos\theta_{sun}$ distributions of 5(N_1 - N_5) nighttime subsamples. $6.5 \leq E_e \leq 20 \text{ MeV}$ and the fiducial volume is 22.5kton.

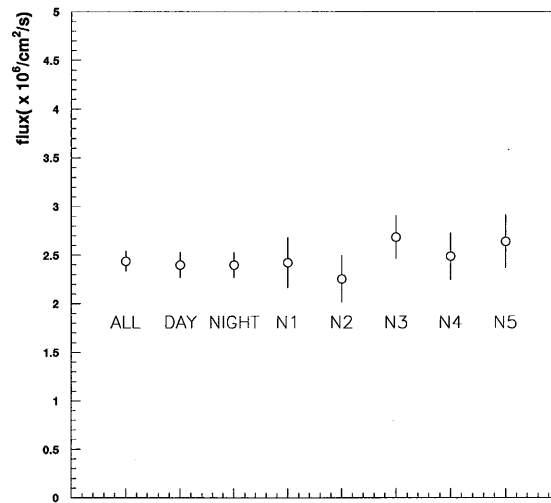


Figure 6.8: Observed ^8B solar neutrino fluxes:all, daytime, nighttime, N1, N2, N3, N4, and N5 data. The error bars include both statistical and systematic ones. $6.5 \leq E_e \leq 20\text{MeV}$ and the fiducial volume is 22.5kton. The null neutrino oscillation case is expected to be a constant line.

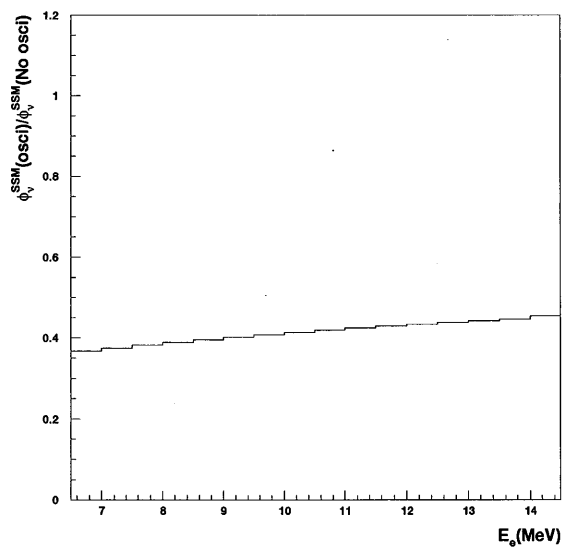


Figure 6.9: Expected energy spectrum distortion of recoil electrons as a function of E_e (MeV), assuming SSM_{BP95} [9] and $(\sin^2 \theta^2, \Delta m^2) = (6.31 \times 10^{-3}, 6.31 \times 10^{-6})$. The vertical axis is normalized by the recoil electron spectrum assuming the null neutrino oscillation case.

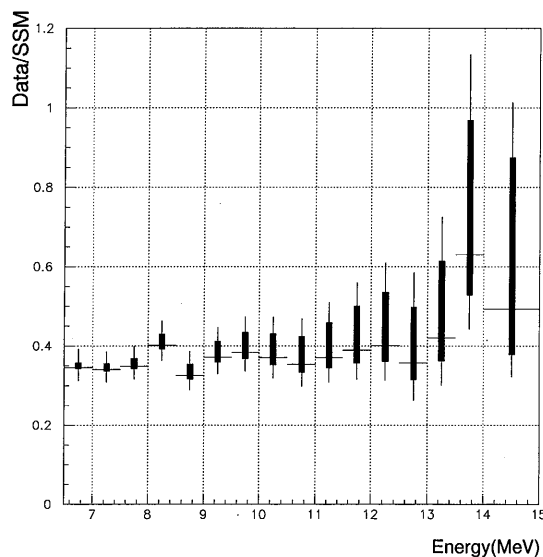


Figure 6.10: Measured energy spectrum of recoil electrons. The horizontal axis is recoil electron energy(MeV), and the vertical axis is the ratio of Data/SSM_{BP95}. The thick line in the error bar represents a correlated error originating from uncertainties in energy scale and resolution. The null oscillation neutrino oscillation case is expected to be a constant line.

6.5 Systematic errors

As possible sources of systematic errors, the following 10 sources are considered for the estimation of the systematic errors.

Energy scale and resolution Systematic uncertainties in energy scale and resolution have been already described in Section.4.5. Errors coming from the uncertainties are estimated by putting artificially the uncertainties in the ^8B solar neutrino MC.

Trigger efficiency The trigger efficiency is estimated by Ni calibration data and the uncertainties are estimated by comparing it with our Ni MC simulation, as described in Subsection.3.8.2. The discrepancy is +1.2% for $E_e=6.5\sim 7.0\text{MeV}$ and $\pm 0\%$ for $E_e > 7\text{MeV}$.

Noise cut “Noise cut” stands for the event reduction criteria described in Appendix.C.1 and C.2. The uncertainty in the reduction criteria is also described in Appendix.C.2. The maximum deviation of the reduction factor between our ^8B solar neutrino MC simulation and the data(typical “spallation” events) which is estimated in Appendix.C.2 and is described in Fig.C.9, is +0.7% above 6.5MeV. It is conservatively employed in the systematic error.

Direction The systematic errors caused by the uncertainty in the direction reconstruction of low-energy event are estimated by comparing our original ^8B solar neutrino MC simulation with ^8B solar neutrino MC simulation artificially distorted with respect to the directional resolution data.

Reduction The uncertainty in reduction efficiency is caused by the flash tube event reduction criteria. The uncertainty is estimated by the difference between Ni calibration data and MC(^8B solar neutrinos and Ni calibration).

Non-flat B.G. Background shape is considered non-flat, i.e. approximated by a 4th-degree polynomial function in the ^8B solar neutrino signal extraction. The uncertainty caused by the background shape is estimated by the difference in signal assuming non-flat and flat background shapes.

Dead time(spallation cut) The systematic error caused by the spallation cut for Day/Night variation study is estimated using “random-timing sample”(see Appendix.E).

Cross section The uncertainty of the neutrino-electron scattering cross section comes from the uncertainties of the Weinberg angle and the radiative-correction.

Live time As described in Subsection.5.2.1, the detector live time is calculated by an off-line process(TQreal). Another way to calculate it is to use the cosmic-ray muon or low-energy event triggered time. The uncertainty is estimated by the difference between the two live days.

Then systematic errors related to various analysis are summarized in Table.6.1.

	Flux	Day/Night	Energy Spectrum
Energy Scale & resolution	+9.9 -3.1	+1.2 -1.1	See Fig.6.10
Trigger efficiency	+0.2	-	6.5~7.0MeV: +1.2 other: 0
Noise cut	± 0.7	-	± 0.7
Direction	+1.7	-	± 0.7
Reduction	± 0.2	-	± 0.2
Non-flat B.G.	± 0.5	All,Day-all,Night-all: ± 1.0 Day 1-4, Night 1-4: ± 1.0 D5, N5: ± 1.6	6.5~7.0MeV: ± 3.0 other: 0
Dead time(spallation cut)	<0.1	± 0.6	-
Vertex Shift	-1.3	-	± 1.0
Cross section	± 0.5	-	± 0.5
Live time	± 0.1	± 0.1	± 0.1
Total	+10.1 -3.5	D1-4,N1-4,All,Dall,Nall: ± 1.6 D5,N5: +2.1, -2.0	See Fig.6.10

Table 6.1: Summary of systematic errors. The correlated errors that come from energy scale and resolution uncertainties in the analysis of the recoil electron energy spectrum is shown in Fig.6.10.

Chapter 7

Discussions

As seen in Chapter.6, the deficit in the ^8B solar neutrino flux is confirmed by 300-day Super-Kamiokande data. In this chapter, the experimental status of solar neutrino experiments is summarized first. Then, some key-points, like how MSW effect is incorporated into our MC simulation are briefly described. Subsequently, a possible MSW effect will be studied based on the Super-Kamiokande results described in Chapter.6 including; the day-night variation in the neutrino flux, the energy spectrum shape, and the combination of the two plus the absolute value of the neutrino flux. This thesis will not deal with possible long-term time variation in the neutrino flux and vacuum neutrino oscillation scenarios which will be later studied by other collaborators.

7.1 Interpretation of Results from Solar Neutrino Experiments

The measured solar neutrino fluxes by current solar neutrino experiments are listed in Table.7.1.

Experiment	Observed flux	SSM _{BP95} prediction	Data/SSM _{BP95}
Homestake	$2.55 \pm 0.14 \pm 0.14^a$	$9.3^{+1.2}_{-1.4}{}^a$	0.273 ± 0.021
Kamiokande-II+III	$2.80 \pm 0.19 \pm 0.33^b$	$6.62^{+0.93}_{-1.12}{}^b$	0.423 ± 0.058
SAGE	$69 \pm 10^{+5}_{-7}{}^a$		0.504 ± 0.089
GALLEX	$69.7 \pm 6.7^{+3.9}_{-4.5}{}^a$	$137^{+8}_{-7}{}^a$	0.509 ± 0.059
Combined	69.5 ± 6.7^a		0.507 ± 0.049
Super-Kamiokande	$2.44 \pm 0.06^{+0.25}_{-0.09}{}^b$	$6.62^{+0.93}_{-1.12}{}^b$	$0.368^{+0.038}_{-0.016}$

^a In unit of SNU

^b In unit of $10^6 \text{cm}^{-2} \text{sec}^{-1}$

Table 7.1: Observed solar neutrino fluxes by current solar neutrino experiments

The ^8B solar neutrino flux obtained by Super-Kamiokande is consistent with that by Kamiokande-II+III within 1σ . The deficit in the solar neutrino flux observed by the five experiments is unaccountable in the framework of the standard solar model(SSM). An alternative solution is the MSW effect. If neutrinos have small finite masses and finite mixing angles, they undergo oscillations from one flavor to another. In such a case, it is well-known that neutrino oscillation

in matter(the MSW effect) seems to be one of natural solutions by which the data of the five experiments can be explained. Several physicists have already studied the MSW effect using the results from the solar neutrino experiments other than the 300-day Super-Kamiokande data. A recent work by Hata et.al[18] has been already shown in Fig.2.18. In this thesis, a possible MSW effect will be tested based on the 300-day Super-Kamiokande data.

7.2 How to incorporate MSW effect

One numerically calculates the two flavor oscillation of neutrinos from the center of the Sun to the Super-Kamiokande detector for different neutrino oscillation parameters($\sin^2 2\theta, \Delta m^2$). The parameter region of $10^{-5} \leq \sin^2 2\theta \leq 1$ and $10^3 \leq E/\Delta m \leq 10^{10}$ is divided into 51×71 points. In order to deal with resonance near the core of the Sun, different 80 points in the core region($R/R_\odot \leq 0.31$) are used as the production points of ν_e in the case of the parameters of $10^{-4} \leq \sin^2 2\theta \leq 1$ and $10^{4.6} \leq E/\Delta m^2 \leq 10^{5.1}$. The distribution of the production points of neutrinos in the Sun is taken from Ref.[9]. The propagation of neutrinos in the Sun is obtained from numerical integration of Eq.2.29 considering the electron density distribution in the Sun. The electron density profile(Fig.2.2) in the Sun is take from Ref.[9].

Upon exiting the surface of the Sun, neutrino oscillations in vacuum are calculated. Here , the electron density is regarded as zero, and the propagation of the neutrino wave functions are given by

$$\begin{pmatrix} \nu_e(R_\odot + L) \\ \nu_\mu(R_\odot + L) \end{pmatrix} = \begin{pmatrix} \cos \frac{\pi L}{L_\nu} + i \cos 2\theta \sin \frac{\pi L}{L_\nu} & -i \sin 2\theta \sin \frac{\pi L}{L_\nu} \\ -i \sin 2\theta \sin \frac{\pi L}{L_\nu} & \cos \frac{\pi L}{L_\nu} - i \cos 2\theta \sin \frac{\pi L}{L_\nu} \end{pmatrix} \begin{pmatrix} \nu_e(R_\odot) \\ \nu_\mu(R_\odot) \end{pmatrix} \quad (7.1)$$

where R_\odot is the solar radius = 6.96×10^{10} cm, L is neutrino travel distance from the solar surface, and L_ν is vacuum oscillation length(see Eq.2.26). To take account of seasonal variation in the neutrino flux due to the orbital eccentricity of the Earth, which contributes to randomization of the phase, the wave functions of neutrinos are calculated at $L = 0.10L_\nu, 0.20L_\nu, 0.30L_\nu, \dots, 1.0L_\nu$ (10 points). The neutrino oscillation probability in the Earth is also numerically calculated using Eq.2.29 at each L (10 points). The oscillation probability in the Earth is calculated at $\cos \delta_{sun} = 0.00, 0.05, 0.10, \dots, 1.00$ (21 points), and then averaged according to the detector live time for each $\cos \delta_{sun}$. And then, the average of the oscillation probabilities of ν_e at Super-Kamiokande is taken. It should be noted that the oscillation probabilities for the analysis of the day/night effect are not averaged over $\cos \delta_{sun}$.

7.2.1 Day/Night effect

To make a quantitative comparison between the data and an expected signal from possible Day-Night variation in ^8B solar neutrino flux assuming the MSW solution , the following χ^2 is calculated at each ($\sin^2 2\theta, \Delta m^2$) using the ^8B solar neutrino flux observed in the daytime sample and 5 nighttime sub-samples shown in Fig.6.8.

$$\chi_{dn}^2 = \sum_{i=1}^{N_{dn}} \left(\frac{R_i - R_{\text{MSW},i} \times \alpha}{\sigma_{dn,i}} \right)^2 \quad (7.2)$$

where N_{dn} is the number of the day/night bins(equal to 6), R_i is the measured flux ratio in the i -th day/night bin, $R_{\text{MSW},i}$ is the expected flux ratio in the i -th day/night bin for a set of

$(\sin^2 2\theta, \Delta m^2)$, $\sigma_{dn,i}$ is the quadratic sum of the statistical error of R_i and the systematic error, and α is a normalization factor. The parameter α is determined so as to give the minimum χ_{dn}^2 . The χ^2 values obtained from Eq.7.2 obey the normal χ^2 distribution with two free parameters. Hence, the regions in the oscillation parameter plane with $\chi^2 \geq \chi_{min}^2 + 2.28, 4.61,$ and 5.99 are excluded at 68%, 90% and 95% C.L., respectively. Figure 7.1 shows a contour of the 95% C.L. excluded region(Day/Night) obtained by the 306.3-day Super-Kamiokande data. The minimum

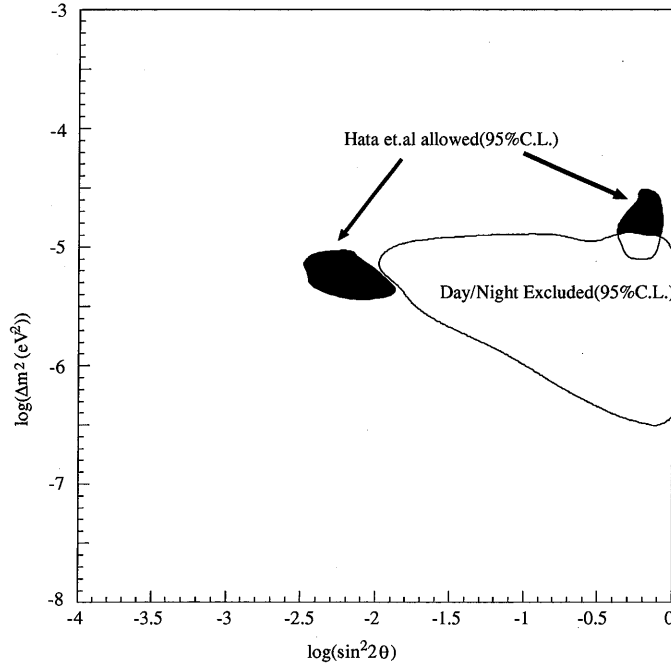


Figure 7.1: Excluded region at 95% C.L.(inside of the contour) on $(\sin^2 2\theta, \Delta m^2)$ plane obtained by the day/night effect analysis in Super-Kamiokande. Also shown is the allowed region presented by Hata et.al[18].

χ_{dn}^2 value is equal to 1.84 at $(\sin^2 2\theta, \Delta m^2) = (3.55 \times 10^{-2}, 1.51 \times 10^{-6})$ for the 306.3-day Super-Kamiokande data.

As seen in this figure, approximately a half of the large mixing angle solution(the filled allowed region in the right) presented by Hata et.al[18] is newly excluded by the analysis.

7.2.2 Spectral shape

Using the energy spectrum of the observed recoil electrons shown in Fig.6.10, another quantitative estimation of the MSW solution is examined. In this case, the χ^2 is defined by

$$\chi_{ene}^2 = \sum_{i=1}^{N_{ene}} \left(\frac{R_i - R_{MSW,i} \times \alpha \times f(\epsilon_r, \epsilon_s)}{\sigma_{ene,i}} \right)^2 + \left(\frac{\epsilon_r}{\sigma_r} \right)^2 + \left(\frac{\epsilon_s}{\sigma_s} \right)^2 \quad (7.3)$$

where N_{ene} is the number of the energy bins(equal to 16), R_i is the measured flux ratio in the i -th energy bin, $R_{MSW,i}$ is the expected flux ratio in the i -th energy bin for a set of $(\sin^2 2\theta, \Delta m^2)$, $\sigma_{ene,i}$ is the quadratic sum of the statistical error of R_i and the systematic error except for

that from the energy scale and resolution, α is a free normalization parameter, ϵ_r and ϵ_s are uncertainties in energy resolution and scale which are assumed to obey Gaussian distributions with $\sigma_r = {}^{+4.7\%}_{-0.0\%}$ and $\sigma_s = {}^{+4.1\%}_{-1.5\%}$, respectively, and $f(\epsilon_r, \epsilon_s)$ is a response function for the bin-to-bin correlated error from uncertainties in energy resolution(ϵ_r) and scale(ϵ_s). In calculation, ϵ_r and ϵ_s are varied by ± 3 standard deviations to obtain the minimum χ_{ene}^2 . The result is shown in Fig.7.2. The minimum $\chi_{ene}^2 = 7.500$ occurs at $(\sin^2 2\theta, \Delta m^2) = (0.166, 6.03 \times 10^{-6})$. The

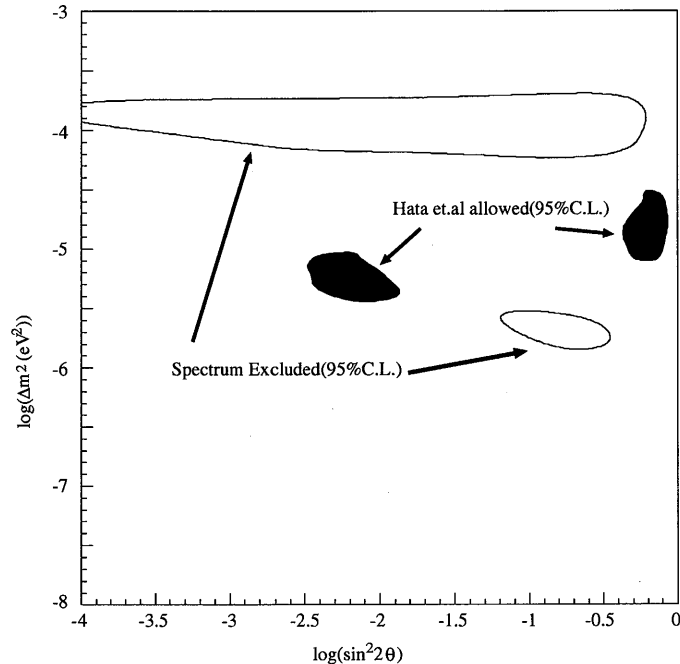


Figure 7.2: Excluded region at 95%(inside of the contour) on $(\sin^2 2\theta, \Delta m^2)$ plane obtained by the energy spectrum shape measurement in Super-Kamiokande. Also shown is the allowed region presented by Hata et.al[18]

regions in the oscillation parameter plane with $\chi_{ene}^2 \geq \chi_{ene,min}^2 + 2.28, 4.61, \text{ and } 5.99$ are excluded at 68%, 90%, and 95% C.L., respectively. No new constraint is obtained by the analysis of the spectral shape only.

7.2.3 Combined result

Combining the observed Day-Night variation and spectral shape in the ${}^8\text{B}$ solar neutrino flux with a constraint of the absolute flux normalization, the MSW solution is also examined. In this case, the χ^2 is defined by

$$\chi_{comb}^2 = \sum_j^{N_{dn}} \sum_i^{N_{ene}} \left(\frac{R_{i,j} - R_{MSW,i,j} \times \alpha \times f(\epsilon_r, \epsilon_s)}{\sigma_{i,j}} \right)^2 + \left(\frac{\epsilon_r}{\sigma_r} \right)^2 + \left(\frac{\epsilon_s}{\sigma_s} \right)^2 + \left(\frac{1 - \alpha}{\sigma_\alpha} \right)^2 \quad (7.4)$$

where N_{ene} is the number of energy bins(equal to 16), N_{dn} is the number of the daytime and nighttime samples(equal to 2), $R_{i,j}$ is the measured flux ratio in the i -th energy bin in

daytime($j=1$) or in nighttime($j=2$), $R_{\text{MSW},i,j}$ is the expected flux ratio for a set of $(\sin^2 2\theta, \Delta m^2)$, $\sigma_{i,j}$ is the quadratic sum of the statistical error of $R_{i,j}$ and the systematic error except for that from the energy scale and resolution, and $\alpha, \epsilon_r, \epsilon_s$ are uncertainties in flux normalization, energy resolution, energy scale respectively which are assumed to obey Gaussian distributions with $\sigma_\alpha = \begin{smallmatrix} +14\% \\ -17\% \end{smallmatrix}$, $\sigma_r = \begin{smallmatrix} +4.7\% \\ -0.0\% \end{smallmatrix}$, $\sigma_s = \begin{smallmatrix} +4.1\% \\ -1.5\% \end{smallmatrix}$ and $f(\epsilon_r, \epsilon_s)$ is a response function for the bin-to-bin correlated error from uncertainties in energy resolution(ϵ_r) and scale(ϵ_s). In calculating the minimum χ^2_{comb} , α is varied from 0 to 5, and ϵ_r and ϵ_s are varied by ± 3 standard deviations.

The minimum $\chi^2_{\text{comb}} = 34.03$ occurs at $(\sin^2 2\theta, \Delta m^2) = (0.646, 1.38 \times 10^{-7})$. The regions in the oscillation parameter plane with $\chi^2_{\text{comb}} \leq \chi^2_{\text{comb},\text{min}} + 2.28, 4.61, \text{ and } 5.99$ are allowed at 68%, 90% and 95% C.L., respectively. The allowed region is shown in Fig.7.3. Looking into Fig.7.3,

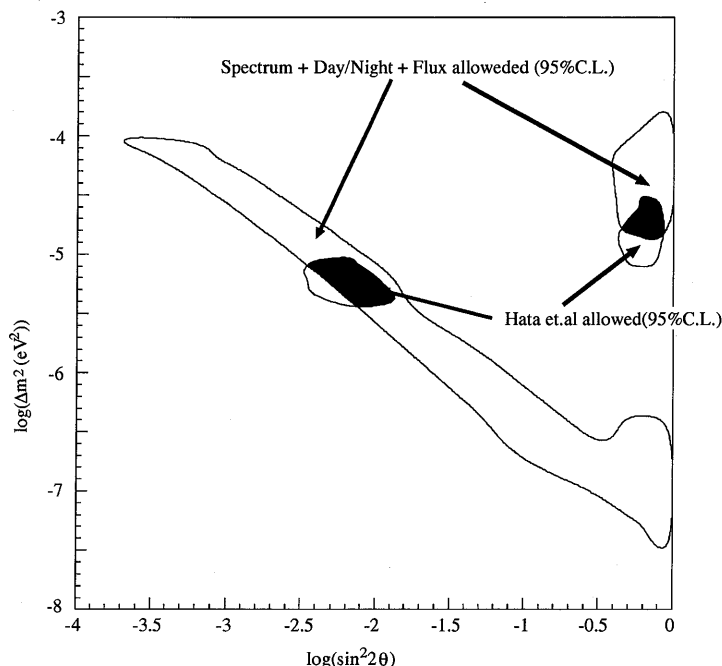


Figure 7.3: Allowed region at 95% C.L. (inside of contour) on the $(\sin^2 2\theta, \Delta m^2)$ plane by Super-Kamiokande. The contour is obtained by combining the observed Day-Night time variation and spectral shape in the ${}^8\text{B}$ solar neutrino flux, with an absolute normalization constraint to the ${}^8\text{B}$ solar neutrino flux. Also shown is the allowed region presented by Hata et.al[18].

a small region in the non-adiabatic solution($\sin^2 2\theta \approx 0.01$) is further excluded in addition to approximately a half of the large angle solution(around $\sin^2 2\theta \approx 0.6$).

7.3 Future Prospect

Some of the allowed region by the four solar neutrino experiments other than Super-Kamiokande is newly excluded by this analysis. However, the problem of the solar neutrino deficit has been still unsolved. In this section, a future prospect is presented.

In this thesis, the Super-Kamiokande sensitivity to possible neutrino oscillations has been limited due to large statistical error and also a large systematic error coming mainly from energy

determination uncertainties. Therefore, it will be re-examined in terms of the energy spectrum shape and the day/night effect assuming a null experimental systematic error and 4-year detector operation of Super-Kamiokande.

The expected excluded region on the $(\sin^2 2\theta, \Delta m^2)$ plane is shown in Fig.7.4 on the assumption that the parent function in the χ^2 obeys the null neutrino oscillation case.

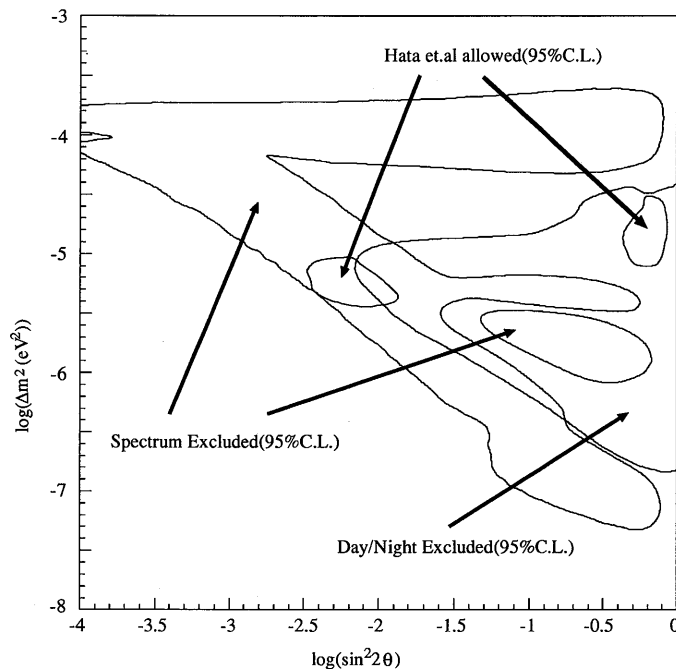


Figure 7.4: Expected excluded region on the $(\sin^2 2\theta, \Delta m^2)$ plane assuming 4-year detector operation of Super-Kamiokande and null experimental systematic error.

Either of the currently allowed region presented by Hata et.al[18] can be excluded at more than 95%C.L., in other words, be explorable. Therefore, further efforts to reduce the experimental systematic errors, especially one from the energy scale uncertainties, will lead us to a critical result to unequivocally conclude the existence or the non-existence of the neutrino oscillation.

Another promising experiment is Sudbury Neutrino Observatory(SNO)[39][40] which is under construction and will start its observation in 1998. In the SNO detector, 1000 tons of pure D₂O and 7300 tons of pure H₂O are used, and the solar neutrinos are detected by the following reactions:

$$\begin{aligned}
 1. \nu_e + d &\rightarrow p + p + e^- \\
 2. \nu_x + d &\rightarrow \nu_x + p + n \\
 3. \nu_x + d &\rightarrow \nu_x + e^- \\
 4. \bar{\nu}_e + d &\rightarrow n + n + e^-
 \end{aligned}
 \tag{7.5}$$

where ν_x means $\nu_e, \nu_\mu,$ and ν_τ . The most interesting part of the SNO detector is that the detector can measure the total flux of solar neutrinos using the neutral current(NC) reaction(2),

even if the electron neutrinos produced at the solar core transform into neutrinos of another flavor. This NC reaction rate can be used to normalize the charged current(CC) reaction(1) rate independent of the solar models, and the CC/NC ratio is used to examine the neutrino oscillation. Another unique capability of the SNO detector is its ability to measure the energy spectrum of the electron neutrino precisely in the reaction(1).

O

O

Chapter 8

Conclusions

The ${}^8\text{B}$ solar neutrino flux($E_{\text{recoil electron}} \geq 6.5\text{MeV}$) is measured by Super-Kamiokande based on 306.3-day data from May 31, 1996 to June 23, 1997.

The total number of recoil electrons scattered by ${}^8\text{B}$ solar neutrinos detected during the detector live days amounts to :

$$4395_{-108}^{+114}(\text{stat.})_{-154}^{+444}(\text{syst.}) \text{ events.} \quad (8.1)$$

The observed ${}^8\text{B}$ neutrino flux is :

$$2.44 \pm 0.06(\text{stat.})_{-0.09}^{+0.25}(\text{syst.})[\times 10^6 \text{ cm}^{-2} \text{ s}^{-1}], \quad (8.2)$$

which should be compared with the standard solar model prediction(BP95)[9]:

$$6.62_{-1.12}^{+0.93}(\text{theo.})[\times 10^6 \text{ cm}^{-2} \text{ s}^{-1}], \quad (8.3)$$

The ratio of the observed ${}^8\text{B}$ solar neutrino flux to the expected flux (BP95) is :

$$0.368_{-0.009}^{+0.010}(\text{stat.})_{-0.013}^{+0.037}(\text{syst.})_{-0.052}^{+0.062}(\text{theo.}) \quad (8.4)$$

The measured ${}^8\text{B}$ solar neutrino flux is consistent with the Kamiokande-II+III results($2.80 \pm 0.19(\text{stat.}) \pm 0.33(\text{syst.})[\times 10^6 \text{ cm}^{-2} \text{ s}^{-1}]$) within 1σ , and the deficit in the ${}^8\text{B}$ solar neutrino flux(solar neutrino puzzle) is confirmed.

The data sample is divided into the daytime and nighttime sub-samples, and the difference is examined. No significant difference has been observed. Based on the difference, the neutrino oscillation hypothesis incorporating the MSW effect is tested and some new region is excluded from the currently allowed region on the $(\sin^2 2\theta, \Delta m^2)$ plane presented by Hata et al.[18]. A more precise recoil-electron energy spectrum than in Kamiokande is also obtained. However, it alone, does not lead to a new constraint to the MSW solution. The combined analysis excludes another new region.

The problem of the solar neutrino puzzle is still unsolved. However, with efforts to reduce the experimental systematic errors, it is expected to be clarified by analyzing 4-year Super-Kamiokande solar neutrino data whether solar neutrino puzzle is due to possible neutrino oscillations or not.

Appendix A

Vertex Point Reconstruction(Low-energy Events)

In this section, a vertex position reconstruction method is described for low-energy(typically $\sim 10\text{MeV}$) electron events. The description consists of the following 2 steps; 1) hit PMT selection, 2) vertex point search. Quality of the vertex fitting is studied as well.

A.1 Hit PMT selection

The reconstruction method uses position and relative timing information of hit PMTs. A typical timing distribution of hit PMTs in a low-energy event is shown in Fig.A.1, where one sees random off-timing noise as well as a signal peak made by Čerenkov photons. The noises

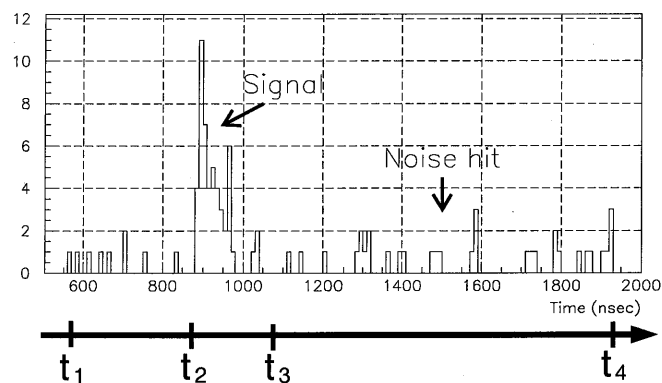


Figure A.1: A typical timing distribution of hit PMTs by a low-energy event(Data). t_1 is the time of the first hit PMT after 500 nsec, and t_4 is the time of the last hit PMT. $t_2 \sim t_3$ is a signal region described in the 1st selection criteria of hit PMTs. Therefore, hits in $t_1 \sim t_2$ and $t_3 \sim t_4$ are regarded as noise hits.

are generated by dark current of PMTs. In order to minimize the noises, one selects hit PMTs

so as to maximize an estimator “*significance*”. The definition of “*significance*” is as follows;

$$significance = \frac{N_{sig}}{\sqrt{N_{noise}}}, \quad (A.1)$$

where N_{noise} is the number of noise hits in a signal region(see Fig.A.2), and N_{sig} is the number of hits in the signal region after noise subtraction(Fig.A.2).

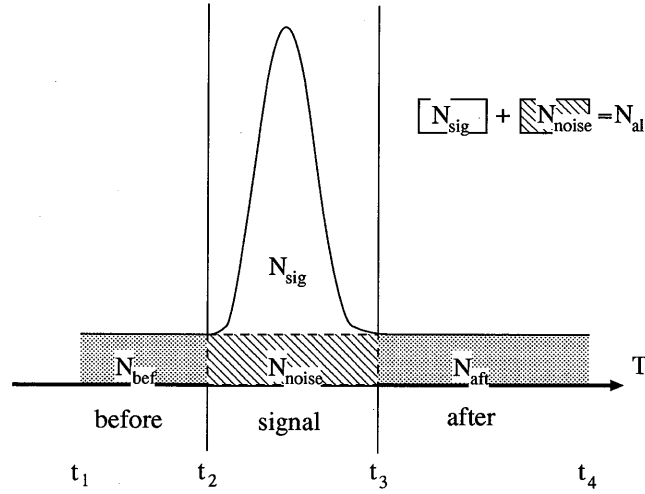


Figure A.2: The definition of signal and noise hits. t_1 , t_2 , t_3 and t_4 are the same as in Fig.A.1

The actual selection criteria are detailed below:

1. Select a 200 nsec time window which includes the maximum number of hit PMTs(see Fig.A.1 and Fig.A.2).
2. Estimate the number of noise hit PMTs in the selected time window. In the estimation, the following equation is used.

$$N_{noise} = (t_2 - t_3) \times \frac{N_{bef} + N_{aft}}{(t_2 - t_1) + (t_4 - t_3)}, \quad (A.2)$$

where N_{bef} and N_{aft} are the number of hit PMTs in $t_1 \sim t_2$ and in $t_3 \sim t_4$, respectively(Fig.A.1 and Fig.A.2).

3. 11 time sub-windows with size of $200 \times n/11$ ($n= 1,2,\dots,11$) are considered. Then a time sub-window which includes the maximum number of hit PMTs is searched in the selected 200-nsec time window for each sub-window size. After this, “*significance*” which is defined in Eq.A.1 is calculated for each sub-window size.
4. Select a sub-timing window which maximize the “*significance*”. However if there is a wider time sub-window which satisfies

$$(significance) > (significance)_{max} \times 0.8, \quad (A.3)$$

the wider time sub-window is employed.

Then, vertex position reconstruction is done with PMTs in the selected time window.

A.2 Reconstruction method

The path length of an electron from a solar neutrino interaction is less than 10cm. The spread of the region where Čerenkov photons are emitted is negligible in comparison with the vertex resolution of about 70cm(1σ at 10MeV). Therefore, one treats the vertex as a point in the reconstruction.

In an ideal case, the principle of vertex position reconstruction is to find a position which minimizes an estimator

$$T^2 = \sum_{i=1}^{N_{hit}} t_{res,i}^2 \quad (\text{A.4})$$

where N_{hit} is the number of hit PMT selected in Section.A.1 and $t_{res,i}$ is the residual time of the i -th hit PMT after subtraction of photon TOF¹. $t_{res,i}$ is expressed by the following equation.

$$t_{res,i} = t_i - \frac{n}{c} \times \sqrt{(x-x_i)^2 + (y-y_i)^2 + (z-z_i)^2} - t_c \quad (\text{A.5})$$

$$= t_{tof,i} - t_c \quad (\text{A.6})$$

where t_i is arrival time of photons in i -th PMT, n is refraction index of water, c is the light velocity in vacuum, (x, y, z) is the vertex position to be decided, (x_i, y_i, z_i) is the position of the i -th PMT and t_c is the peak in the $t_{tof,i}$ distribution. Eq.A.4, however, does not take into account of a finite timing resolution of the PMT shown in Fig.4.8. Instead of Eq.A.4, a new “goodness” is introduced by

$$goodness = \frac{1}{\sum \frac{1}{\sigma_i^2}} \times \sum_i \frac{1}{\sigma_i^2} \exp\left[-\frac{t_{res,i}^2}{2\sigma_i^2}\right] \quad (\text{A.7})$$

where σ_i is timing resolution of the i -th PMT. Each σ_i is inherently PMT-dependent, however, it is set to $\langle \sigma \rangle = 5\text{nsec}$. The best fit point yields the largest value of “goodness”. The reason can be shown by following expansion at $t_i \approx T$:

$$\begin{aligned} goodness &\approx \frac{1}{\sum \frac{1}{\sigma_i^2}} \times \sum_i \frac{1}{\sigma_i^2} \left(1 - \frac{t_{res,i}^2}{2\sigma_i^2}\right) \\ &= 1 - \frac{1}{\sum \frac{1}{\sigma_i^2}} \times \sum_i \frac{1}{\sigma_i^2} \left(\frac{t_{res,i}^2}{2\sigma_i^2}\right) \end{aligned} \quad (\text{A.8})$$

That is, to maximizing *goodness* is identical to minimize the familiar χ^2 value. On the other hand, t_i 's which are far away from the mean value t_c by more than $2 \times \langle \sigma \rangle$ can only make a small contribution to the *goodness*.

A grid-search method² is used to search for the point where *goodness* becomes maximum. The initial position is given by $(x, y, z) = (-1590, -1590, -1710)[\text{cm}]$. The minimum grid size is 5cm.

¹Time Of Flight from emitted to detection by PMT

²It is one of general method for nonlinear fitting. For example, see “DATA REDUCTION AND ERROR ANALYSIS FOR THE PHYSICAL SCIENCES”, p150,1992, by McGraw-Hill, Inc.

A.3 Quality of reconstruction

To estimate the quality of the vertex point reconstruction mentioned, data taken in Nickel calibration runs described in sec 4.5.2 are used. In Fig.A.3, the vertex position distribution of reconstructed γ -ray events from (Ni+Cf) source are shown together with MC simulation, where (Ni+Cf) source is placed at the center of the detector, i.e. $(x, y, z) = (35.3, -70.7, 0.0)$ [cm]. A

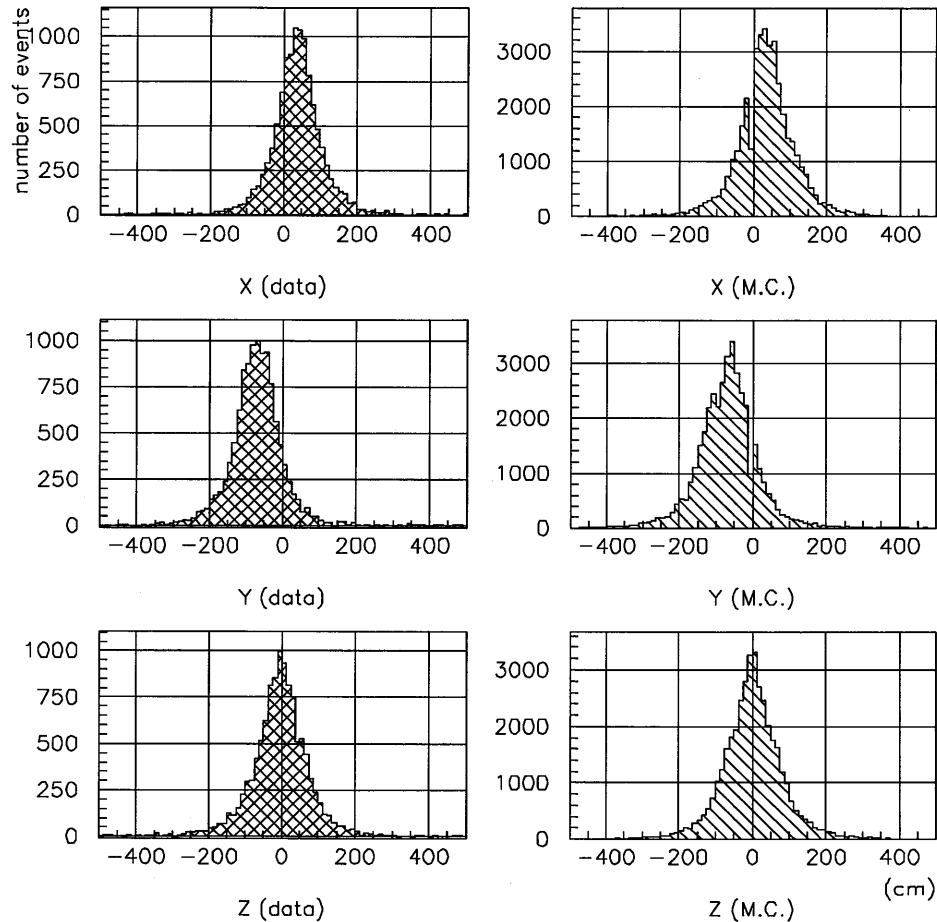


Figure A.3: Vertex position distributions of reconstructed γ -ray events from a Ni calibration run: for data(left) and MC(right)

small systematic shift is observed. Then the possible vertex shift is measured at several positions in the detector, as summarized in Table.A.1, where the vertex point is the mean value of the Gaussian fit and σ is one standard deviation. The systematic shift of the reconstructed vertex point from the real source location is estimated to be 16cm at most and much less than the standard deviation.

From this figure, it is concluded that the vertex position and resolution are well reproduced in then MC simulation.

position(x,y,z)	Δx	Δy	Δz	σ_x	σ_y	σ_z	σ_r
(35.3,-70.7,-1200)	-0.3	-2.7	-3.0	47.98	49.28	47.66	115.8
(35.3,-70.7,0)	0.7	-0.5	-1.9	47.11	49.23	52.80	114.2
(35.3,-70.7,1200)	-1.0	-0.7	-1.0	46.87	48.17	47.88	113.6
(35.3,-70.7,1600)	-0.6	-2.8	-10.0	46.98	46.40	44.67	111.6
(35.3,-1201,-1200)	-3.4	7.0	-7.0	46.91	47.65	47.40	110.7
(35.3,-1201,0)	-1.1	16.0	-1.1	42.70	43.16	50.08	113.0
(35.3,-1201,1200)	0.6	10.0	2.0	43.74	44.92	48.74	109.4

Table A.1: Vertex position shift and resolution(1 standard deviation) in unit of cm measured at several positions in the detector

Appendix B

Reconstruction of track direction(Low-energy Events)

B.1 Reconstruction Method

A maximum likelihood characterized by the Čerenkov ring pattern method is adopted to reconstruct the direction of low-energy electron event. A likelihood function ($L(\vec{d})$) is defined by:

$$L(\vec{d}) = \sum_i \log(f(\cos\theta_{dir,i})) \times \frac{\cos\theta_i}{a(\theta_i)}, \quad (\text{B.1})$$

where the probability function $f(\theta_{dir,i})$, and $\theta_{dir,i}$ are depicted in Fig.B.1, and θ_i is photon incident angle of the i-th PMT, $\frac{a(\theta_i)}{\cos\theta_i}$ is acceptance function of photo-cathode-coverage. The

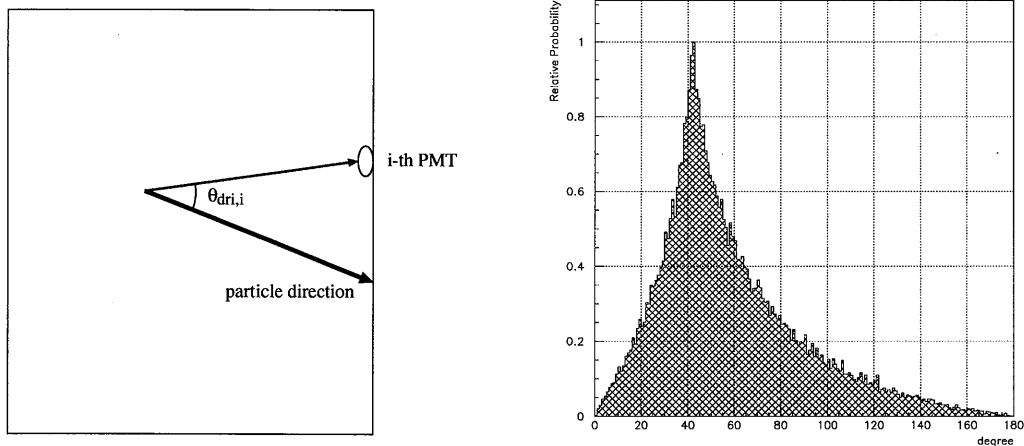


Figure B.1: The left figure illustrates the definition of $\theta_{dir,i}$. The right figure shows a Čerenkov photon detection probability as a function of opening angle of Čerenkov light photons(angle with respect to the particle track direction).

function $f(\theta_{dir,i})$ in Fig.B.1 is obtained by a MC simulation for 10MeV electrons. Ideally, the broad probability function would have a sharp peak at 42° corresponding to the Čerenkov light

emission angle in water by a relativistic charged particle. However, smearing due to the electron multiple Coulomb scatterings and Čerenkov light scatterings in water have to be considered.

The direction is determined by a maximum-likelihood method. To find the maximum-likelihood value, a grid-search method(footnote A.2) is as usual employed, too. The step sizes of the grid-search are $20^\circ, 9^\circ, 4^\circ, 1.6^\circ$. The initial direction is given by a vector sum of hit-PMT direction vectors measured from the reconstructed vertex position.

B.2 Quality of reconstruction

The quality of the direction fitter is estimated by LINAC data taken at four different energies(8.826, 10.9609, 13.6666, 16.301 MeV) with the beam end cap located at $(x, y, z) = (-1237, -70.7, +1228)[\text{cm}]$. Figure B.2 shows the distribution of the angle between the direction of the electron from LINAC and the reconstructed direction, together with a LINAC MC simulation. The difference between real and reconstructed angles is due mainly to electron mul-

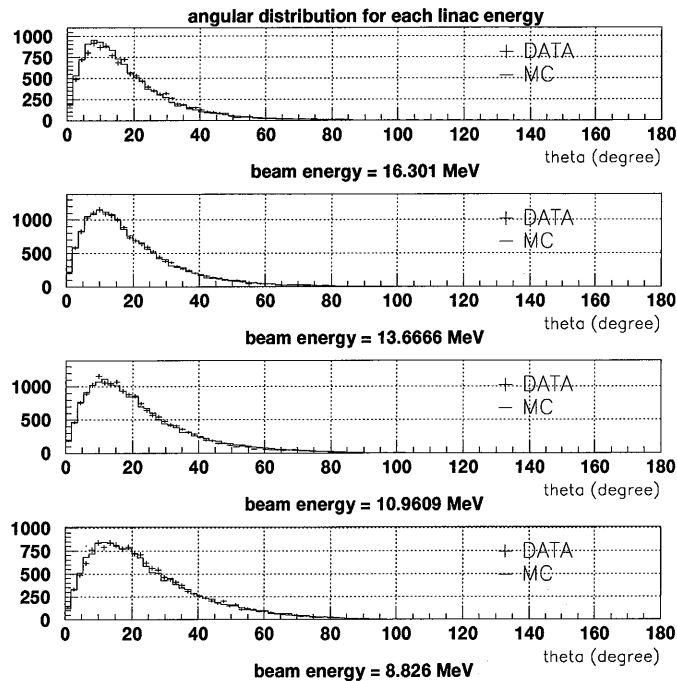


Figure B.2: Distribution of the angle between the direction of the electron from LINAC and the reconstructed direction. The solid lines represent MC and the crosses represent LINAC data.

multiple Coulomb scatterings in water. As seen in this Fig.B.2, the MC reproduces the LINAC data correctly. Using this MC, the directional resolution at various position and energies are estimated, as are shown in Fig.B.3. They demonstrate that the angular resolution becomes worse when the distance from the wall is less than 2m, i.e. outside of the fiducial volume.

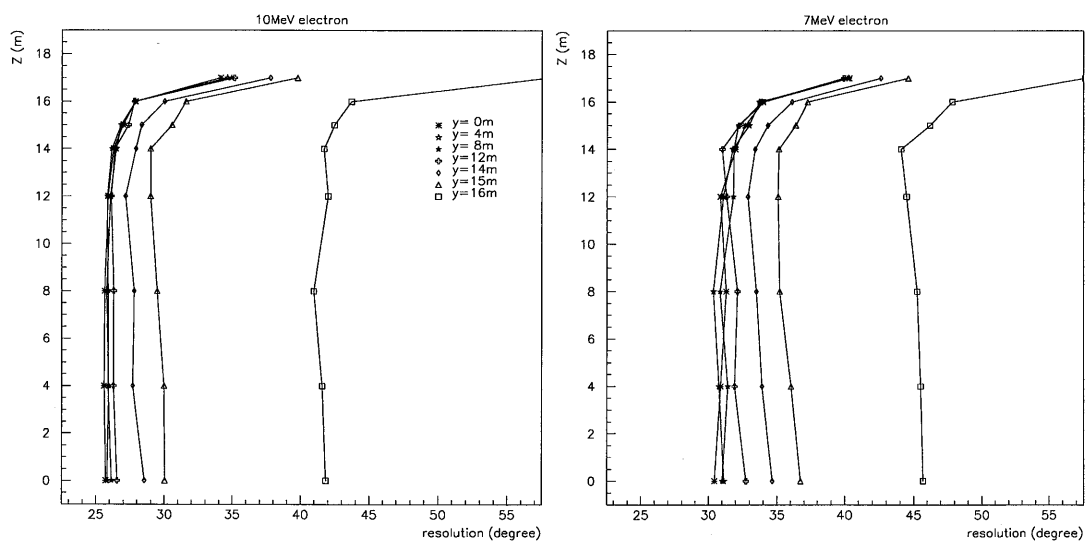


Figure B.3: The angular resolution calculated by the MC simulation at several energies and positions.

Appendix C

Noise cleaner

C.1 Vertex Position Cleaner

In this chapter, a method to eliminate misfit (\equiv wrong vertex position) events is described. The misfit is caused by a random cluster of hit PMTs in the selected time sub-window other than true signal. An example is shown in Fig.C.1. where, a cluster of hit PMTs is produced by

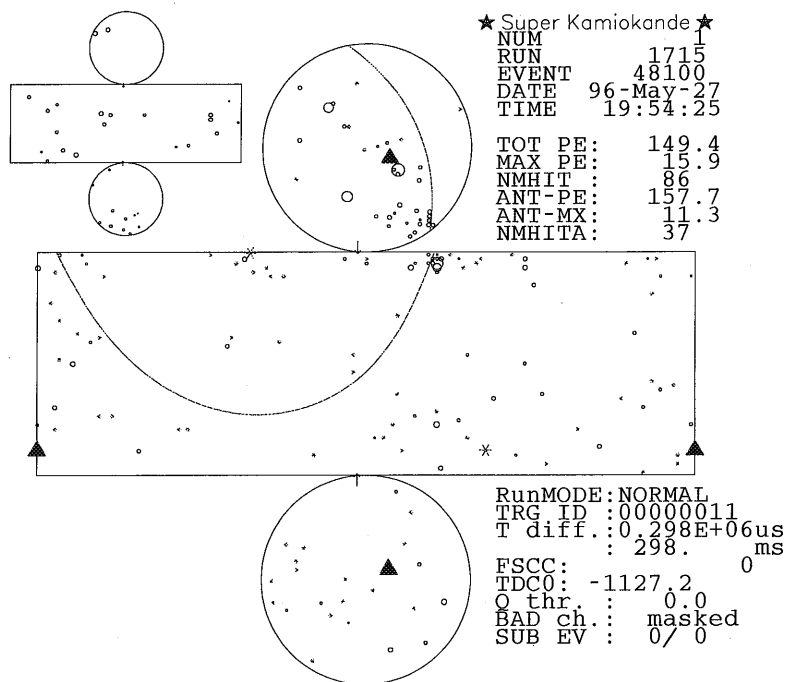


Figure C.1: Typical low-energy event which will be removed by the noise cleaner. Large dotted circle represents the Čerenkov ring reconstructed (wrongly) by the low-energy event fitter.

γ -rays emitted from detector materials, e.g., PMT glass (Fig.C.2).

In this method, 2 parameters, Δl_{ij} and Δt_{ij} are introduced, where Δl_{ij} is distance between

Super-Kamiokande detector

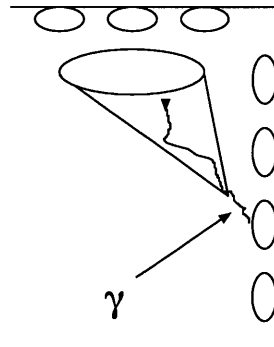


Figure C.2: Cartoon of a typical misfit low-energy event.

the i -th and the j -th hit PMT(Fig.C.3), and Δt_{ij} is time difference between the i -th and the j -th hit PMT. If the i -th PMT doesn't have any neighboring PMTs which satisfy $\Delta l_{ij} \leq l_{limit}$

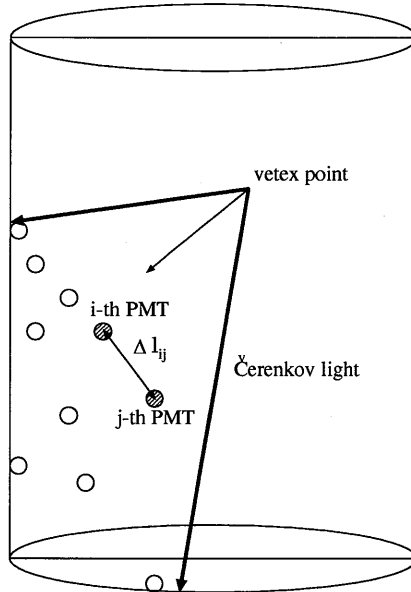


Figure C.3: Definition of $\Delta_{ij}l$

and $\Delta t_{ij} \leq t_{limit}$, the PMT is not used for the vertex position reconstruction, where l_{limit} is set to 700 cm and t_{limit} is set to 35 nsec. These upper limits are determined by using LINAC 5.87-MeV(reconstructed electron energy=5.5~6.5 MeV) data, so that 74% of the hit PMTs may satisfy the above conditions at 5.87MeV.

Then the vertex point($V_{cleaner}$) is reconstructed using only PMTs which satisfy the conditions above. Subsequently the difference(ΔV) between $V_{cleaner}$ and the low-energy reconstructed vertex position by the normal low-energy fitter(V_{fitter}) is plotted Fig.C.4. As is seen in Fig.C.4, ΔV become worse in lower-energy region. Events with ΔV greater than 500cm

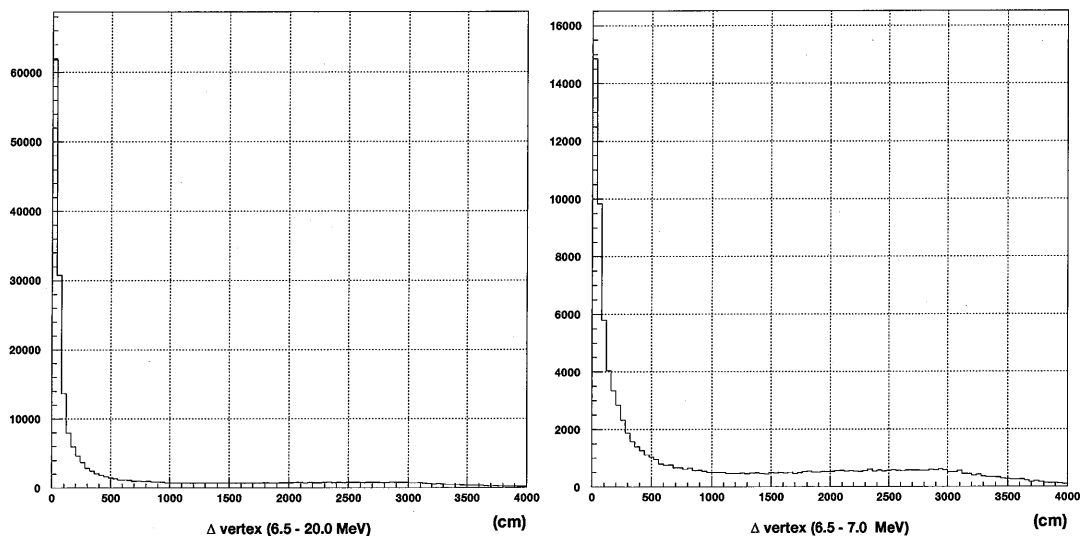


Figure C.4: ΔV distribution of low-energy events before “spallation cut” (cf. Fig.5.7) in the 6.5~20MeV region(left) and in the 6.5~7.0MeV region(right)

are eliminated as misfit. To demonstrate the reduction power of this noise cleaner, $\cos \theta_{sun}$ distributions before and after this noise cleaner are shown in Fig.C.5, which indicate that the background rejection power of noise-cleaner is about a factor of 1.5 ~ 2, and that is more effective in lower-energy region.

C.2 Direction Cleaner

A misfit direction occurs in events with the vertex position near the edge of the fiducial volume, as is shown in Fig.C.6. To reject such misfit events, Kolmogorov-Smirnov(K-S) test is used. The K-S test is a general statistical test which is applicable to unbinned distributions that are functions of a single independent variable, that is, to data sets where each data point can be associated with a single number(for example, lifetime of each lightbulb when it burns out, or declination of each star).

It is assumed that positions of hit PMTs uniformly distribute along the Čerenkov light ring. Under this assumption, hit PMT number is used as the angle φ independent variable and a cumulative distribution as a function of azimuth angle of hit PMTs as shown in Fig.C.7 is used for the test. Ideally, the cumulative distribution function should behave like a dashed straight line in the lower-left-figure in Fig.C.7. Distance between the two solid lines named “*dirks*” illustrated by an arrow in Fig.C.7 is used as estimator of the K-S test. The “*dirks*” distributions of the data(before “spallation cut(cf. Appendix.E)) and MC (^8B solar neutrinos) are shown in Fig.C.8. The events with “*dirks*” >0.4 are thrown away.

Finally, the “*dirks*” cut combined with “Vertex cleaner” described in Section.C.1 is applied to the data before “spallation cut(cf. Appendix.E)” and the MC. The reduction function is estimated for the data(typical “spallation” events) and MC, as is shown in Fig.C.9. The “spallation” events are supposed to have a uniform vertex position distribution over the fiducial

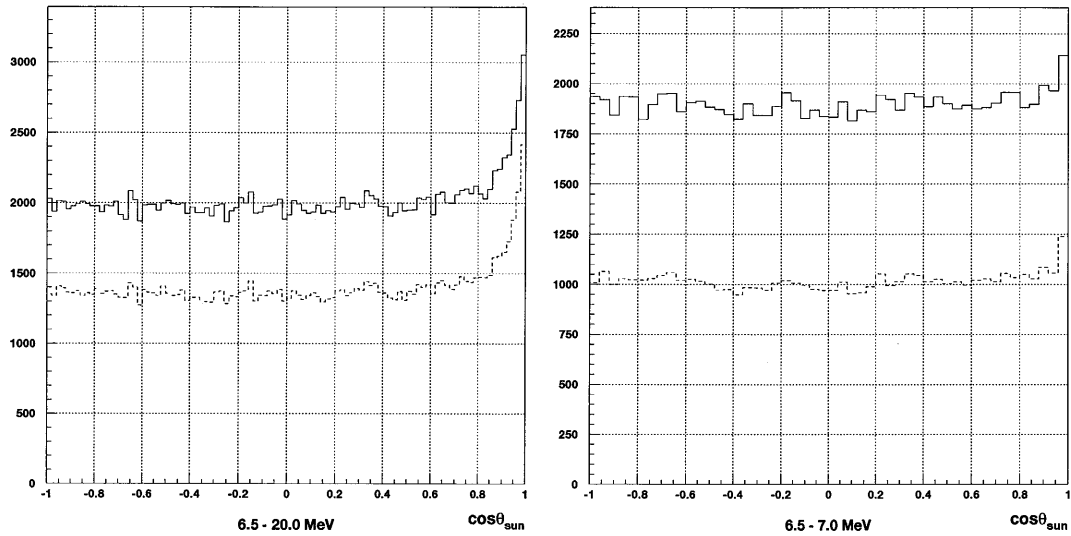


Figure C.5: $\cos\theta_{sun}$ distribution of low-energy events “spallation cut” (cf. Fig.5.7) before and after vertex position cleaner; for 6.5~20MeV(left) and for 6.5~7.0MeV(right), respectively. The solid(dashed) line represents data before(after) vertex position cleaner.

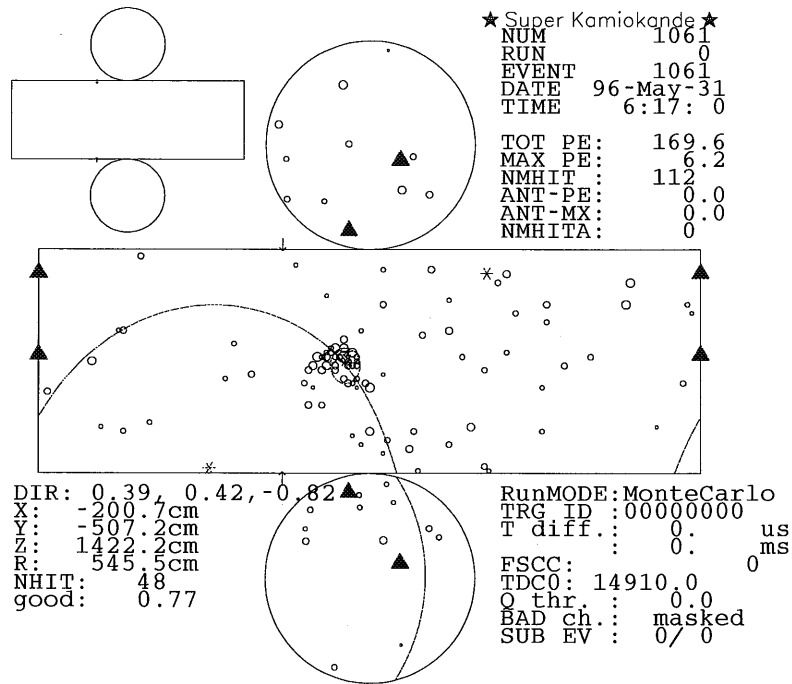


Figure C.6: A typical MC direction-misfit event. Larger circle is the wrongly reconstructed Čerenkov ring, while the smaller one is the Čerenkov light ring expected from the true electron direction.

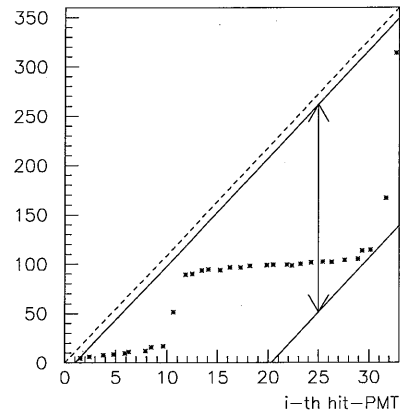
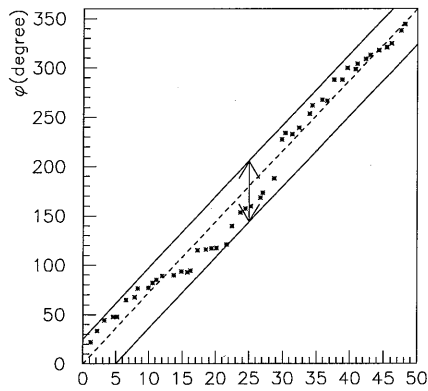
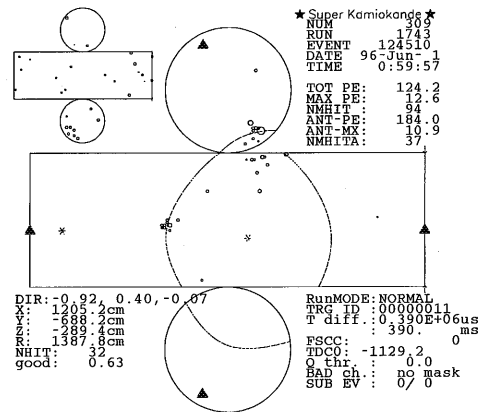
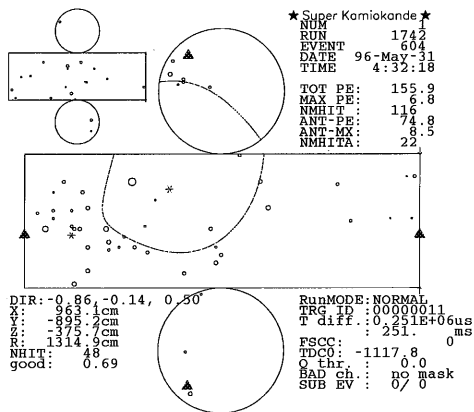


Figure C.7: Typical cumulative distributions of low-energy events. The upper-left(right) figure demonstrates a typical well-fit(misfit) event which give the lower-left(right) cumulative distribution. The dashed line in a lower figure is the expected line, from which the two parallel solid lines pass the farthest data point on either side of the expected line.

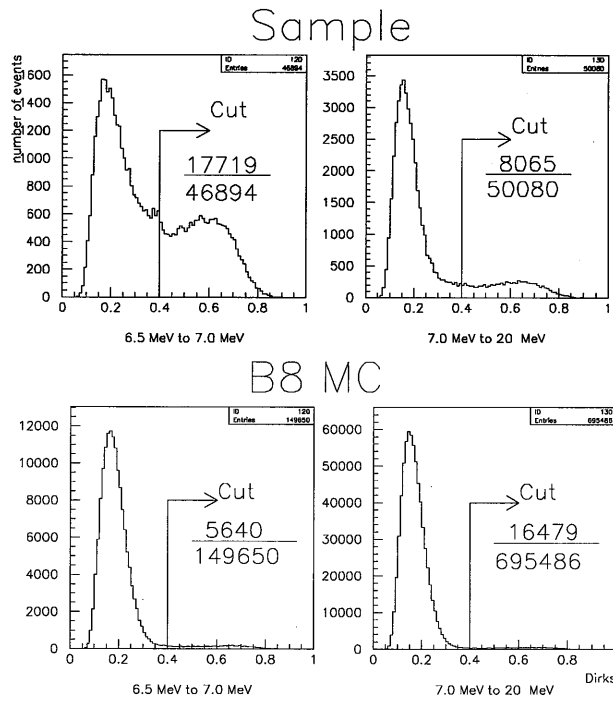


Figure C.8: “*Dirks* distributions of real data(Before “spallation cut”, 200-day data(cf. Appendix.E)) and ^8B solar neutrino MC events. Upper figures are real data, lower ones are MC ^8B solar neutrino data. In the number ratio in these figures, the numerator is the number of rejected events and the denominator is the number of total events.

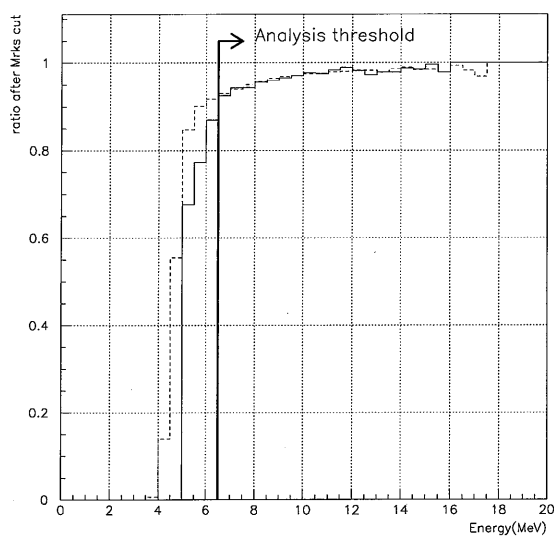


Figure C.9: Reduction factor of the Noise cleaners(vertex + direction) as the function of recoil electron energy, for “spallation” data and MC ^8B solar neutrino events. The solid(dashed) line is the reduction factor for the ^8B solar neutrino data(MC).

volume. The data and MC data keep good consistency above the analysis threshold energy of 6.5MeV. The difference is at most 0.7% and it is taken account in systematic errors.

Appendix D

Muon track fitting

The event rate of cosmic-ray muons in Super Kamiokande is about 2 Hz. They emit a lot of photons in the inner detector(ID), typically greater than 1000 photoelectron(p.e.), and hit the outer detector(OD) as well. In Fig.D.1, a typical cosmic-ray muon which penetrates the detector is shown. They are not direct background against ^8B solar neutrinos, however, some of them, especially, energetic enough induce a serious background named "spallation events". While they

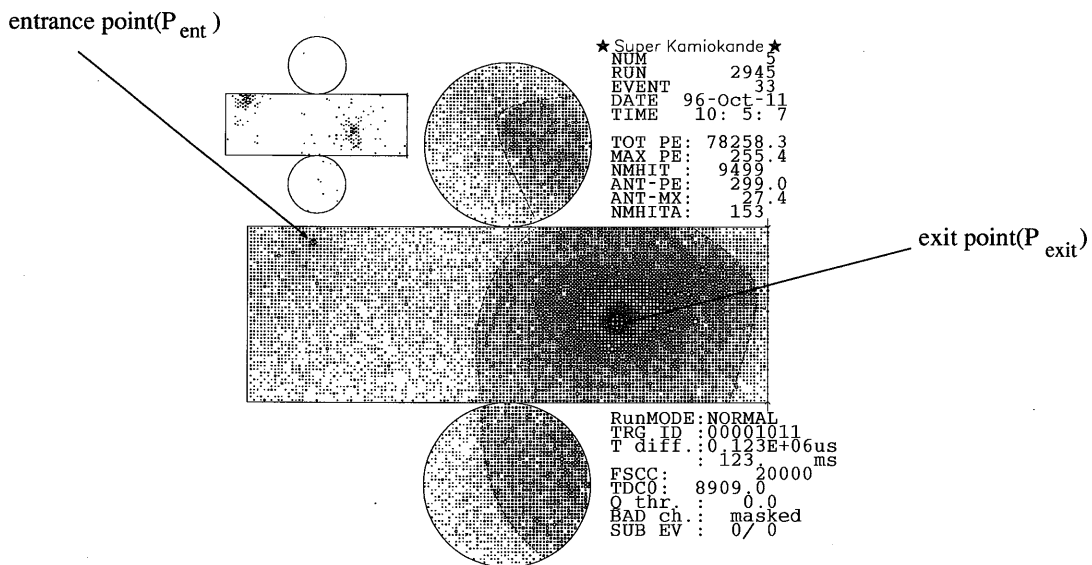


Figure D.1: A typical cosmic-ray single-track muon which goes through the detector. In the event, the entrance point is at the upper-left corner of barrel region, while the exit point is located in right-middle of the barrel region. The large circle indicates the Čerenkov ring edge estimated by the muon-fitter.

are passing the detector, they occasionally spall ^{16}O nuclei in the detector water and produce radioactive isotopes. The low-energy events which originate from these radioactive isotopes are "spallation events". The details of spallation events will be described in Appendix.E, however, they have the following characteristic:

- Their vertex positions are located along the parent muon track.
- The parent muon leave a large energy deposit.
- Time difference between the parent muon and a spallation event are characterized by decay life time of the produced radioactive isotopes.

To reject spallation events, it is necessary to reconstruct the parent muon track as accurately as possible.

In this chapter, a method to reconstruct a muon track will be presented. A method to reject spallation events will be described in the next chapter.

D.1 Reconstruction method

A typical μ hits a large number of PMTs. A brute-force reconstruction method such as described in method described in Appendix.A would spend enormous computer CPU time: It should be noted that the cosmic-ray muon rate is $\sim 2\text{Hz}$. A muon fitter should be much faster than 2Hz. In order to reduce the CPU time, the muon fitter is composed of 2 stages: fast and precise fitter. A flow chart of the muon reconstruction algorithm is shown in Fig.D.2. Muons

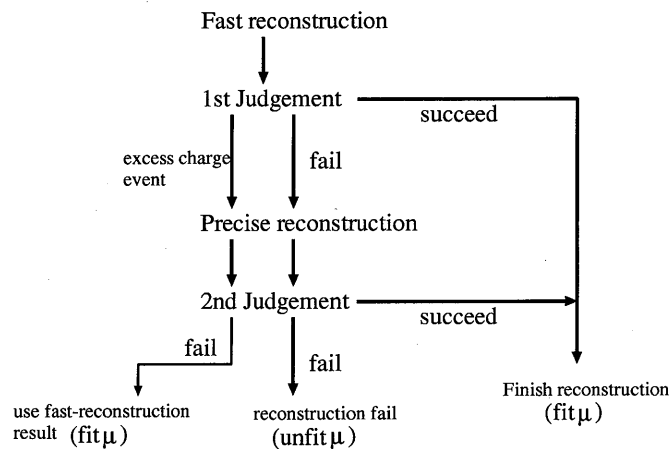


Figure D.2: Schematic view of the μ reconstruction

are then classified into 2 categories: well fit muons and unfit muons. The track information of unfit muons is not, of course, used in the spallation cut. The treatment of fit as well as unfit muons in the spallation cut are given in Appendix.E.

D.1.1 Fast reconstruction method

The entrance position(P_{ent}) is given by the position of the earliest hit-PMT in ID which has more than 2 neighboring PMT hits within 5 nsec.

The PMTs around the exit point detect enormous amount of Čerenkov photons, because the size of Čerenkov ring becomes relatively smaller. Then, the exit point is given by the center of

gravity of charge-saturated PMTs with charge > 231 photoelectron (p.e.). The saturation is due to the limited ADC (analog-to-digital converter) dynamic range.

The direction \vec{c} is accordingly defined by:

$$\vec{c} = \frac{\sum_i^N Q_i \vec{p}_i}{|\sum_i^N Q_i \vec{p}_i|} \quad (D.1)$$

where N is the number of charge-saturated PMTs, Q_i is a charge recorded by the i -th charge-saturated PMT and \vec{p} is a vector from the entrance to the i -th saturated PMT.

D.1.2 1st Judgment

To judge the quality of the fast muon fitter, the following 2 distances are introduced;

- L_{ent} : the distance between the position of each charge-saturated PMT and the entrance position
- L_{exit} : the distance between the position of each charge-saturated PMT and the exit position

Then it is required that at least one charge-saturated PMT which satisfies both $L_{ent} > 300cm$ and $L_{exit} < 300cm$ ("geometrical condition"). These requirements are to reject stopping muons which stop inside the detector and multiple muons as shown in Fig.D.3. If an event doesn't satisfy

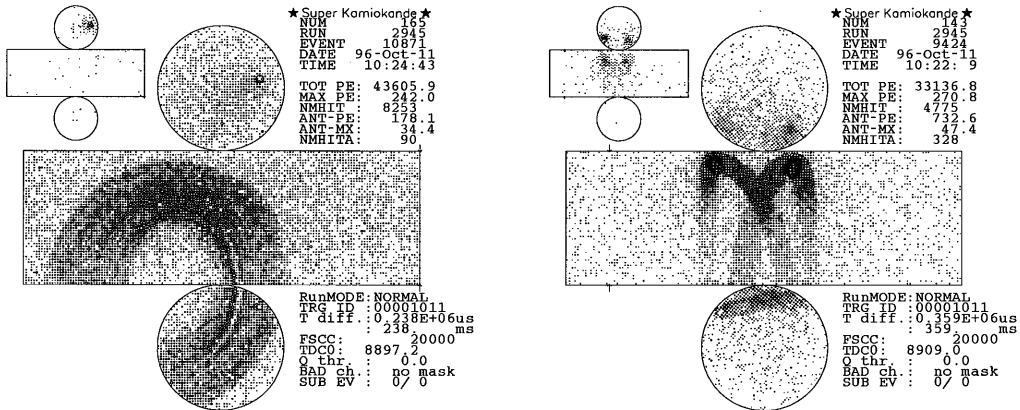


Figure D.3: A typical stopping muon event(left) and multiple-muon event(right). The multiple-muon event has two tracks.

these conditions, the fast reconstruction is judged to have failed, and the event goes to the next step, i.e. the precise muon fitter. When the number of charge-saturated PMTs is large, the fast muon fitter lose its precision. For this reason, muons which emit too many photons are rejected, even if they pass *geometrical condition*. These muons are referred as "excess charge event" which have $ResQ > 25,000[p.e]$, where $ResQ$ is defined by

$$ResQ = Q_{total} - L_{\mu} \times 23, \quad (D.2)$$

in which $Q_{total}(p.e.)$ is total charge of an event, $L_{\mu}(cm)$ is muon track length in the tank, and 23 p.e./cm is the average measured energy deposit by a penetrating muon. They also go to the next step too.

D.1.3 Precise reconstruction

When the fast muon fitter fails to fit an event, the precise reconstruction is applied to the event. It is also applied to *excess charge* event. This method is in principle almost the same as the one employed in the vertex position reconstruction of the low-energy events. The only difference lies that the finite muon track length is taken into account in the muon fitter whereas the low-energy(10MeV) electron track is approximated as point-like in the vertex reconstruction. The precise muon fitter is based on a grid search method using the following *goodness* as an estimator;

$$goodness = \frac{1}{\sum \frac{1}{\sigma_i^2}} \times \sum_i \frac{1}{\sigma_i^2} \exp \left[-\frac{1}{2} \left(\frac{t_i - T}{1.5\sigma_i} \right)^2 \right] \quad (D.3)$$

$$t_i = T_i - \frac{l_\mu(P_{exit})}{c} - \frac{l_{ph}(P_{exit})}{c/n} \quad (D.4)$$

where T is the time when a muon hits ID, σ_i is timing resolution of the i -th PMT set uniformly to 3 nsec, T_i is hit time of the i -th PMT, c is the light velocity in vacuum, n is refraction index of water(1.334), and $l_\mu(P_{exit})$ and $l_{ph}(P_{exit})$ are muon flight distance and Čerenkov photon flight distance which are dependent on the muon exit point(P_{exit}), respectively as shown in Fig.D.4. The muon exit point(P_{exit}) is iterated with the fixed entrance (P_{ent}) already determined by

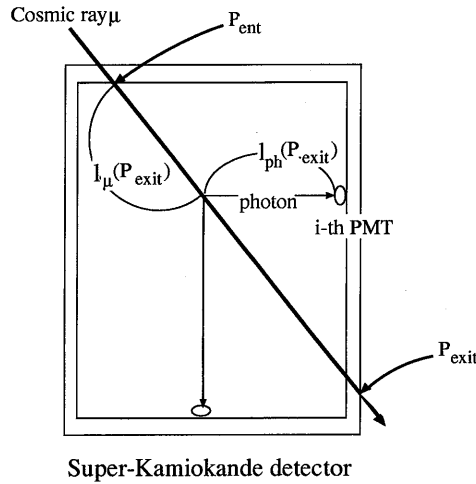


Figure D.4: Definition of l_μ and l_{ph} for precise muon fitter.

the fast muon fitter so as to maximize *goodness*.

D.1.4 2nd Judgment

Events which satisfy the following 3 conditions are defined as fit- μ

- $L_{ent} > 300\text{cm}$
- $L_{exit} < 300\text{cm}$

- $goodness > 0.88$

where L_{ent} is the distance between the position of each charge-saturated PMT and the entrance position, and L_{exit} is the distance between the position of each charge-saturated PMT and the exit position.

Events which don't satisfy the 3 conditions above are classified as unfit μ , other than *excess charge* events. *Excess charge* events which don't satisfy the 3 conditions above are classified as fit μ as well, which use the fast reconstruction result.

D.2 Quality of reconstruction

D.2.1 Event type dependence of the muon fitter

To estimate the quality of the muon track reconstruction, 1000 real events are studied.

These events are classified into 5 categories; clear single-track muon, stopping muon, hard interaction muons, edge clipping and multiple muons. The definitions are as follows;

- stopping muon: muon which stop inside the detector
- hard interaction muons, where ResQ is greater than 25,000 p.e.
- edge clipping : track length is less than 5m
- multiple muons : more than 1 muon are detected in an event.
- clear single-track muon

In Table.D.1, this classification is summarized. The fraction of unfit muon is approximately 6%.

μ type	number of event	number of unfitted event
clear single	835	5
stopping	10	8
hard	41	2
edge clipper	58	19
multi	56	28
total	1000	62

Table D.1: Event type dependence of the μ -fitter

D.2.2 Track reconstruction resolution

The reconstructed $P_{ent}(\text{fitter})$ and $P_{exit}(\text{fitter})$ are compared with those ($P_{ent}(\text{MC})$ and $P_{exit}(\text{MC})$) given by a MC event generation. The difference in center point of the muon track between these 2 methods is taken as track reconstruction resolution, as is shown in Fig.D.5. The track resolution(1σ) is estimated to be 59cm for a typical single-track penetrating muon.

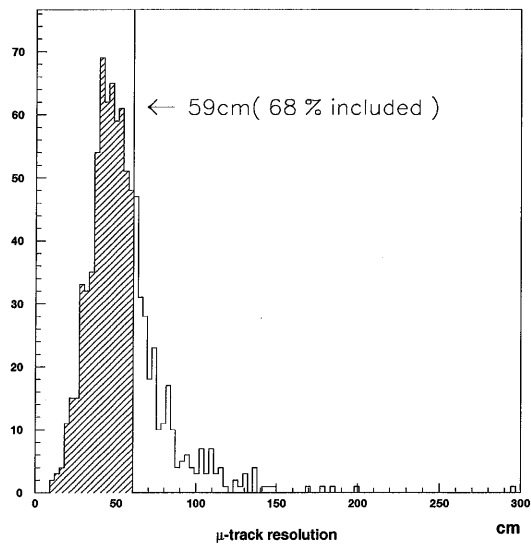


Figure D.5: Track resolution of the muon fitter. For the MC single-track penetrating muon, the resolution is estimated to be 59 cm.

Appendix E

Spallation cut

E.1 Basic Idea

As described in Appendix.D, “spallation events” which originate from long-lived radioactive isotopes induced by an energetic cosmic-ray muon become serious backgrounds against ^8B solar neutrino events. List of spallation radioactive isotopes which decay via β and/or γ decays is summarized in Table.5.1. A spallation event has a strong spatial and time correlation with its preceding parent muon. The parent muon tends to have higher energies than an unbiased muon, as well. On the contrary, non-spallation events, e.g., ^8B solar neutrinos, β -rays from ^{214}Bi decay, γ -rays from outside of the detector, have no such correlation. To judge how a low-energy event looks like a spallation event, a spallation likelihood function is defined. Then the reduction factor of the spallation cut is estimated.

E.2 Likelihood function

First, the following 3 parameters, DT , DL and $ResQ$, related with a parent muon are defined:

DT is time difference between low energy event and the preceding parent muon.

DL is the shortest distance between the muon track and the vertex position of the low energy event.

$ResQ$ is the residual muon charge as defined in Eq.D.2 Then, the spallation likelihood function is expressed by:

$$L_{spa}(DL, DT, ResQ) = L_{spa}^{DL}(DL, ResQ) \cdot L_{spa}^{DT}(DT) \cdot L_{spa}^{ResQ}(ResQ) \quad (\text{E.1})$$

for fit muons which have muon track information

$$= L_{spa}^{DT}(DT) \cdot L_{spa}^{ResQ}(ResQ) \quad (\text{E.2})$$

for unfit muons which have no muon track information

(see Appendix.D)

where $L_{spa}^{DL}(DL, ResQ)$, $L_{spa}^{DT}(DT)$, and $L_{spa}^{ResQ}(ResQ)$ are three likelihood functions described below.

E.2.1 $L_{spa}^{DL}(DL, ResQ)$

Six DL distributions ($L_{i-correlated}^i(DL); i = 1, 6$) are made for pairs of time-correlated ($DT < 0.1sec$) low-energy ($N_{eff} \geq 50 (\sim 8MeV)$) event before the spallation cut and the preceding muon, as is shown in Fig.E.1, where the subscript i represents one of six $ResQ$ regions: 1) $ResQ < 2.5 \times 10^4 [p.e.]$, 2) $2.5 \times 10^4 \leq ResQ < 5.0 \times 10^4 [p.e.]$, 3) $5.0 \times 10^4 \leq ResQ < 1.0 \times 10^5 [p.e.]$, 4) $1.0 \times 10^5 \leq ResQ < 5.0 \times 10^5 [p.e.]$, 5) $5.0 \times 10^5 \leq ResQ < 1.0 \times 10^6 [p.e.]$, and 6) $ResQ \geq 1.0 \times 10^6 [p.e.]$.

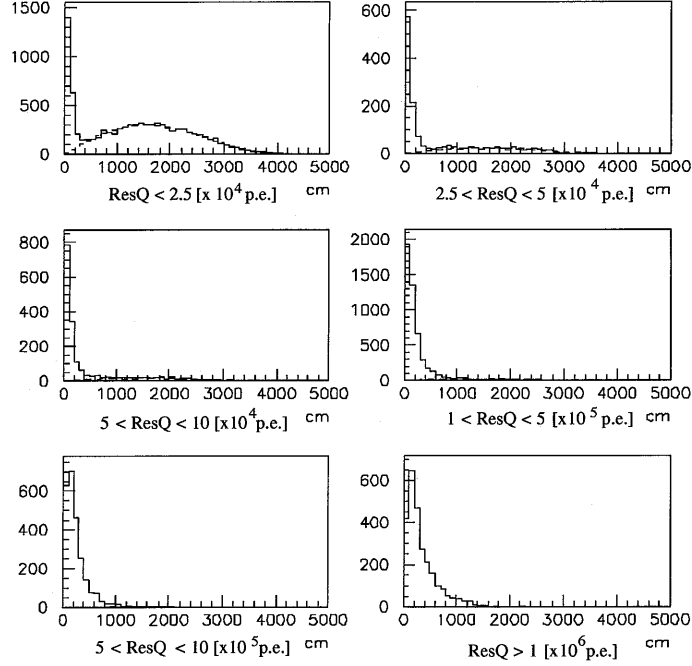


Figure E.1: DL distributions. DL distribution are made in 6 $ResQ$ regions: $\leq 2.5 \times 10^4 [p.e.]$, $2.5 \times 10^4 \sim 5 \times 10^4$, $5 \times 10^4 \sim 1 \times 10^5$, $1 \times 10^5 \sim 5 \times 10^5$, $5 \times 10^5 \sim 1 \times 10^6$, $> 1 \times 10^6$. Solid line represents the time-correlated low-energy events and dashed line stands for the non-spallation event.

Then, six DL distributions ($L_{non-spa}^i(DL); i = 1, 6$) are also made for pairs of fake low-energy event which are generated uniformly in the fiducial volume (22.5kton) by a MC simulation and a real cosmic-ray muon reconstructed by the muon fitter (see Appendix.D), as is shown in Fig.E.1. The time correlated events have a sharp peak in a small DL region, whereas non-spallation events distribute in a smooth phase space. Those peak events are treated as true spallation events. Then, the probability functions $P_{spa}^{DL}(DL)$ and $P_{non-spa}^{DL}(DL)$ are calculated as follows:

$$P_{spa}^{DL}(DL)^i = L_{i-correlated}^i(DL) - L_{non-spa}^i(DL) \quad (E.3)$$

$$P_{non-spa}^{DL}(DL)^i = L_{non-spa}^i(DL) \quad (E.4)$$

And a likelihood function

$$L_{spa}^i(DL) = \frac{P_{spa}^{DL}(DL)^i}{P_{non-spa}^{DL}(DL)^i} \quad (E.5)$$

is defined and shown in Fig.E.2

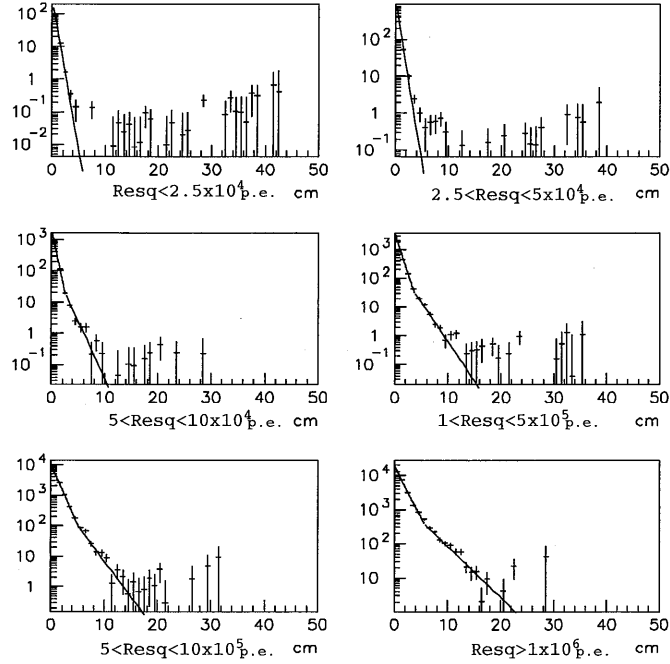


Figure E.2: $L_{spa}^i(DL)$ distributions.

Then as shown in Fig.E.2, a fit is made to $L_{spa}^i(DL, ResQ)$, assuming a function of

$$L_{spa}^{i,fit}(DL) = A_i \cdot e^{(B_i - C_i \cdot DL)} \quad (E.6)$$

where A_i , B_i , and C_i are free parameters:

$$\begin{aligned} A_1 &= 2.836, & B_1 &= 5.594, & C_1 &= 2.107 \\ A_2 &= 5.406 \times 10^{-1}, & B_2 &= 7.176, & C_2 &= 2.087 \\ A_3 &= 2.705 \times 10^{-1}, & B_2 &= 7.608, & C_2 &= 1.850 \text{ (for } DL \leq 2.502\text{m)} \\ A_3 &= 2.705 \times 10^{-1}, & B_2 &= 5.071, & C_2 &= 0.836 \text{ (for } DL \geq 2.502\text{m)} \\ A_4 &= 6.607 \times 10^{-2}, & B_2 &= 8.175, & C_2 &= 1.301 \text{ (for } DL \leq 3.635\text{m)} \\ A_4 &= 6.607 \times 10^{-2}, & B_2 &= 5.706, & C_2 &= 0.622 \text{ (for } DL \geq 3.635\text{m)} \\ A_5 &= 1.075 \times 10^{-2}, & B_2 &= 9.187, & C_2 &= 0.902 \text{ (for } DL \leq 5.201\text{m)} \\ A_5 &= 1.075 \times 10^{-2}, & B_2 &= 7.288, & C_2 &= 0.537 \text{ (for } DL \geq 5.201\text{m)} \\ A_6 &= 2.834 \times 10^{-3}, & B_2 &= 9.843, & C_2 &= 0.713 \text{ (for } DL \leq 5.470\text{m)} \\ A_6 &= 2.834 \times 10^{-3}, & B_2 &= 7.813, & C_2 &= 0.342 \text{ (for } DL \geq 5.470\text{m)} \end{aligned}$$

Finally,

$$L_{spa}^{DL}(DL, ResQ) = \sum_{i=1}^6 L_{spa}^{i,fit} \cdot \Theta(ResQ - ResQ_i) \cdot \Theta(ResQ_{i+1} - ResQ) \quad (E.7)$$

is obtained, where the subscript i represents one of six $ResQ$ regions: $ResQ_1 = 0$, $ResQ_2 = 2.5 \times 10^4[p.e.]$, $ResQ_3 = 5.0 \times 10^4[p.e.]$, $ResQ_4 = 1.0 \times 10^5[p.e.]$, $ResQ_5 = 5.0 \times 10^5[p.e.]$, $ResQ_6 = 1.0 \times 10^6[p.e.]$, $ResQ_7 = 1.0 \times 10^6[p.e.]$.

E.2.2 $L_{spa}(DT)$

A DT distribution ($T_{s-correlated}(DT)$) is made for pairs of spatially-correlated ($DL < 3m$) low-energy ($N_{eff} \geq 50$ ($\approx 8MeV$)) event before the spallation cut and the preceding muon, as are shown Fig.E.3. Then, probability functions $P_{spa}^{DT}(DT)$ and $P_{non-spa}^{DT}(DT)$ becomes:

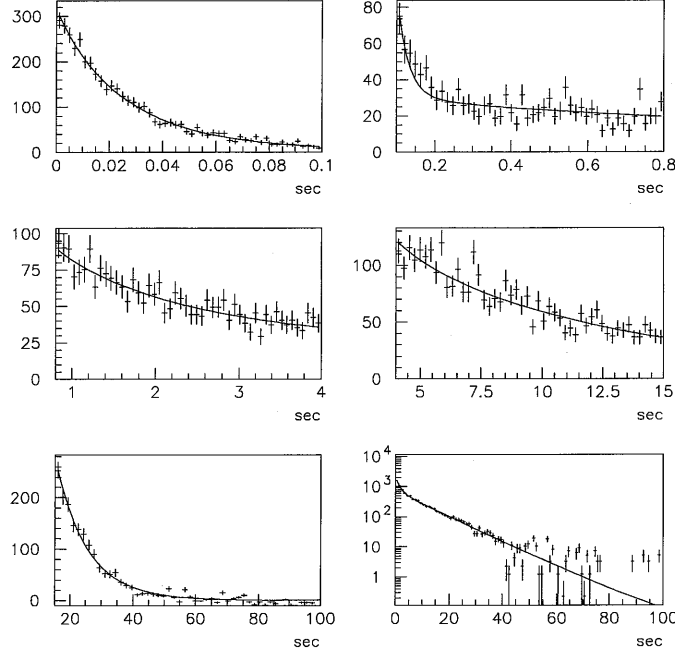


Figure E.3: DT distributions. Typical nucleus lifetime are supposed in each time region; $0 \sim 0.1 \text{sec}$: ${}^5_3\text{B}$ (80%), ${}^{12}_7\text{N}$ (20%), $0.1 \sim 0.8 \text{sec}$: ${}^9_3\text{Li}$ (100%), $0.8 \sim 4 \text{sec}$: ${}^8_3\text{Li}$ (90%), ${}^{15}_6\text{C}$ (10%), $4 \sim 15 \text{sec}$: ${}^{16}_7\text{N}$ (100%), $15 \sim 100 \text{sec}$: ${}^{11}_4\text{Be}$ (100%). Lowest-right-figure represents whole time range

$$P_{spa}^{DT}(DT) = T_{s-correlated}(DT) \quad (\text{E.8})$$

$$P_{non-spa}^{DT}(DT) = 1 \quad (\text{E.9})$$

It should be noted that the $P_{non-spa}^{DT}(DT)$ distribution is supposed to be a constant(=unity). Then, $L_{spa}(DT)$ is obtained by making a fit to the function $\frac{P_{spa}^{DT}(DT)}{P_{non-spa}^{DT}(DT)} = T_{s-correlated}(DT)$, assuming a linear combination of exponential functions of DT

$$L_{spa}(DT) = \sum_{i=1}^7 A_i \left(\frac{1}{2}\right)^{\frac{DT}{T_{1/2,i}}}, \quad (\text{E.10})$$

where A_i is a free parameter and $T_{1/2,i}$ is a fixed half-life of 7 typical radio active isotopes:

$$A_1 = 33900, T_{1/2,1} = 0.0110 \text{sec} \left({}^{12}_7\text{N} \right)$$

$$A_2 = 120100, T_{1/2,2} = 0.0203 \text{sec} \left({}^5_3\text{B} \right)$$

$$\begin{aligned}
A_3 &= 338.6, T_{1/2,3} = 0.178\text{sec} \left({}^9_3\text{Li} \right) \\
A_4 &= 1254, T_{1/2,4} = 0.84\text{sec} \left({}^8_3\text{Li} \right) \\
A_5 &= 134.7, T_{1/2,5} = 2.449\text{sec} \left({}^{15}_6\text{C} \right) \\
A_6 &= 676.1, T_{1/2,6} = 7.134\text{sec} \left({}^{16}_7\text{N} \right) \\
A_7 &= 7.791, T_{1/2,7} = 13.83\text{sec} \left({}^{11}_4\text{Be} \right)
\end{aligned}$$

One notices a characteristic nucleus life time in each DL region, as is shown in Fig.E.3.

E.2.3 $L_{spa}^{ResQ}(ResQ)$

A $ResQ$ distribution($Q_{t\text{-correlation}}(ResQ)$) is made for pairs of time-correlated($DT < 0.1\text{sec}$) low-energy($N_{eff} > 50$ (8 MeV)) events, before the spallation cut and the preceding muon, as is shown in Fig.E.4. Then another $ResQ$ distribution($Q_{non\text{-spa}}(ResQ)$) is made for pairs of

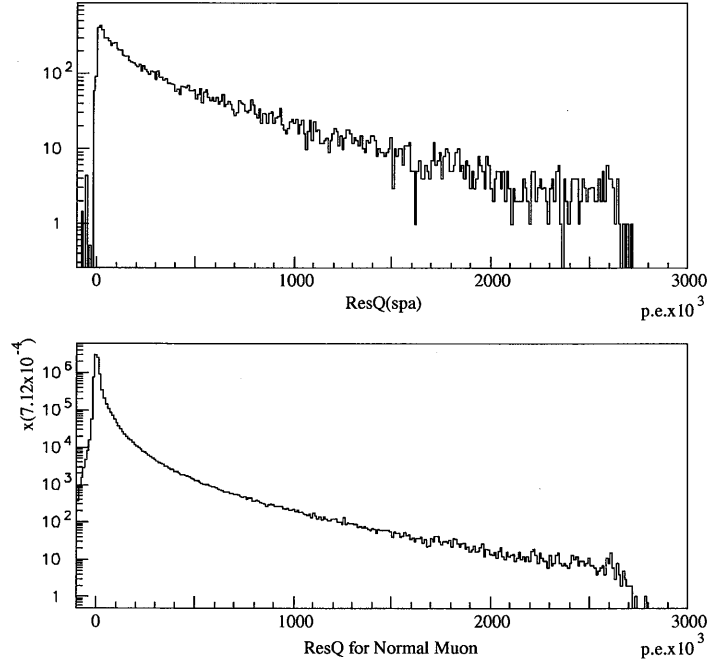


Figure E.4: $ResQ$ distributions for spallation muons(upper) and for un-biased muons(lower).

uncorrelated event and a real cosmic-ray muon reconstructed by muon fitter(see Appendix.D), as is also shown in Fig.E.4.

The probability functions $P_{spa}^{ResQ}(ResQ)$ and $P_{non\text{-spa}}^{ResQ}(ResQ)$ are calculated as follows:

$$P_{spa}^{ResQ}(ResQ) = Q_{t\text{-correlated}}(ResQ) - Q_{non\text{-spa}}(ResQ) \quad (\text{E.11})$$

$$P_{non\text{-spa}}^{ResQ}(ResQ) = Q_{non\text{-spa}}(ResQ) \quad (\text{E.12})$$

Consequently, $L_{spa}(ResQ)$ is obtained by making a fit to the function $\frac{P_{spa}^{ResQ}(ResQ)}{P_{non\text{-spa}}^{ResQ}(ResQ)}$ shown in Fig.E.5, assuming a 4th-polinomial and 2th-polinomial function of $ResQ$:

$$L_{spa}(ResQ) = \begin{cases} \sum_{i=0}^4 A_i(ResQ)^i & ResQ < 5.0 \times 10^5 \\ \sum_{i=0}^2 A_i(ResQ)^i & ResQ \geq 5.0 \times 10^5 \end{cases} \quad (\text{E.13})$$

where A_i is free parameter:

for $ResQ < 5.0 \times 10^5$

$$A_0 = 1.507 \times 10^{-4}, A_1 = 7.138 \times 10^{-9}, A_2 = 9.987 \times 10^{-14}$$

$$A_3 = -1.307 \times 10^{-19}, A_4 = 6.407 \times 10^{-26}$$

for $ResQ \geq 5.0 \times 10^5$

$$A_0 = -2.644 \times 10^{-2}, A_1 = 7.086 \times 10^{-8}, A_2 = -3.661 \times 10^{-15}$$

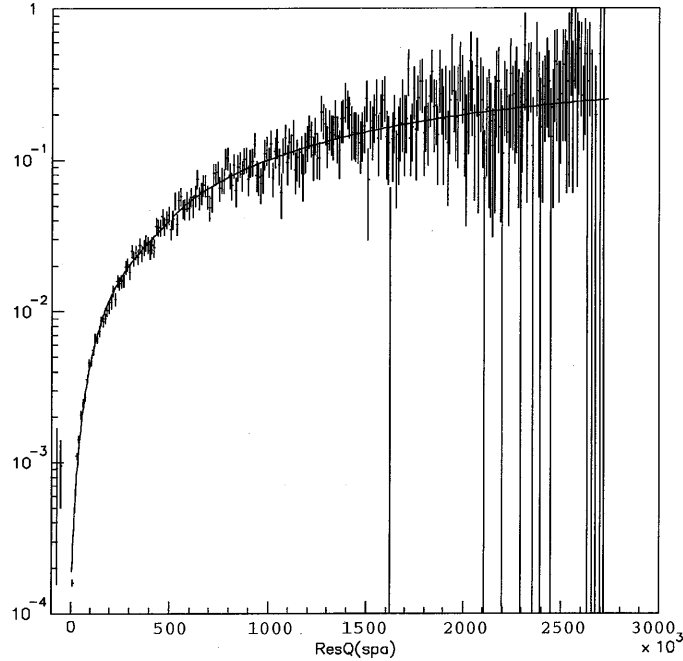


Figure E.5: $L_{spa}(ResQ)$ distributions. .

E.2.4 How to find a pairing muon

The spallation likelihood is calculated for a pair of low-energy event and preceding muon candidate. The candidate muons are traced back to 100sec before the low energy event. Then, a pair which gives the maximum likelihood($L_{spa}(DL, DT, ResQ)$) is selected. There are 2 different set of spallation likelihood distributions; one for well fit muons and the other for unfit muons(See Chapter.D), as are shown in Fig.E.6.

E.3 Dead time due to the spallation cut

To estimate dead time which comes from the spallation cut, a "Random sample" is used. To generate this sample, one collects very low-energy events($N_{50} < 25$ hit and $N_{eff} < 30$ hit(≈ 5 MeV)) roughly every 10 second, and randomize their vertex point artificially. They are supposed to be caused by β -rays from radon decays in the water or γ -rays from the surrounding rock. Hence, this sample assumedly have no correlation with cosmic-ray muons.

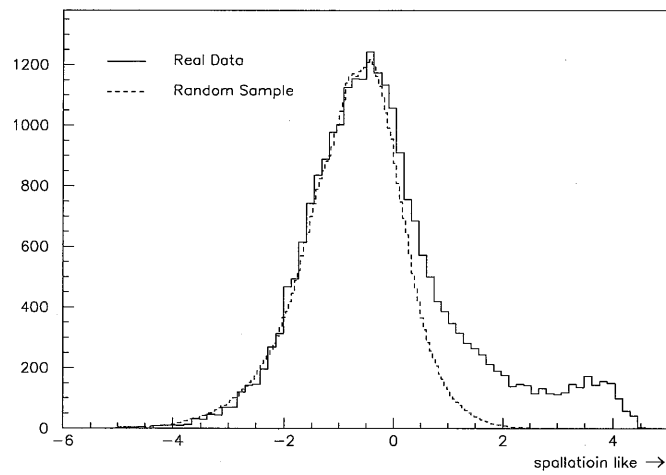
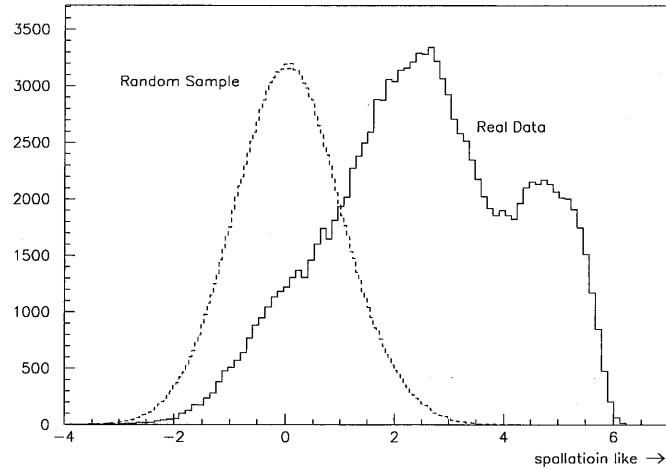


Figure E.6: spallation likelihood distributions for fit muons(upper) and for unfit muons(lower), together with the expected distributions from a random-timing sample. In each figure, the solid line represents real data, and the dashed line represents random timing sample. As is seen in the lower figure, there is no significant difference between the two distributions. Accordingly the spallation cut using unfit muon causes a large dead-time.

The cut is determined so as to maximize “Significance” defined below:

$$\text{Significance} \equiv \frac{1 - \text{deadtime}}{\sqrt{\text{remaining}}}, \quad (\text{E.14})$$

where “dead-time” is dead-time estimated by the random sample, and “remaining” is the remaining number of real events.

Figure E.7 shows two-dimensional distribution of dead time and significance. Finally, the cut

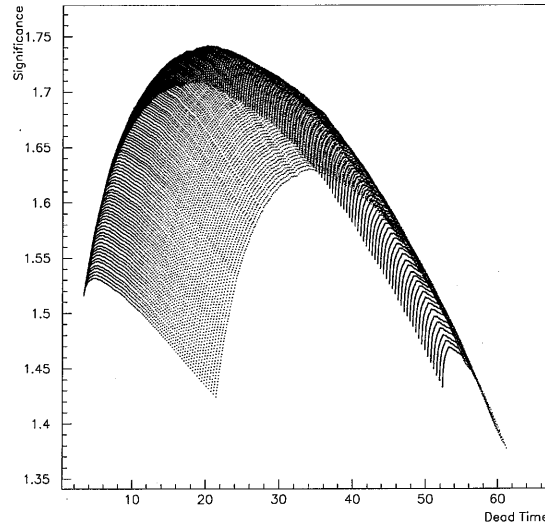


Figure E.7: Dead-time vs Significance. The horizontal axis is dead time in unit of %, estimated by a random sample, and the vertical axis is *significance* defined in Eq.E.14.

in Likelihood is set at 1.06(fit muon) and 0.92 (unfit muon) where dead time becomes 19.5%. Furthermore, event vertex position dependence of dead-time introduced by the spallation cut is studied. In Fig E.8, dead time estimated at several positions is shown. The difference in ^8B neutrino flux between a constant dead time of 19.5% and the position dependent dead-time is about 0.05%. The time variation of the dead-time is also estimated to be $\pm 0.5\%$.

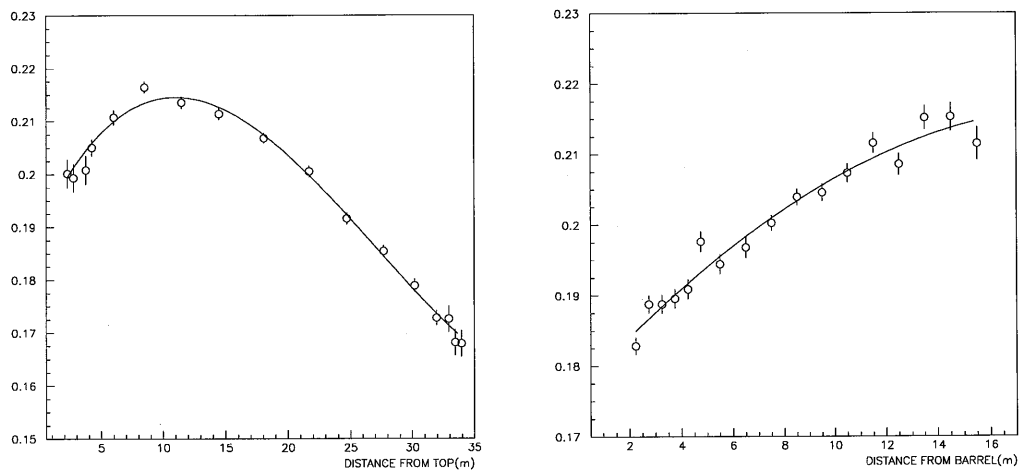


Figure E.8: Position dependence of dead-time. The horizontal axis is distance from top(barrel) of the detector in the left(right) figure. The vertical axes are dead time.

Appendix F

Energy Determination

In a low energy region($\sim 10\text{MeV}$), the number of hit PMTs is used to calculate the energy of an event. A recoil electron scattered by a ^8B solar neutrino gives typically 10MeV equivalent of energy deposit in the Super-Kamiokande detector. The hit PMTs (45 hits at 10MeV in the center of detector) detects mostly a single photoelectron signal. The energy is approximately proportional to the number of hit PMTs. Therefore, the number of hit PMT(N_{hit}) is used for energy determination after applying some corrections.

The corrected N_{hit} is called as N_{eff} and is defined by Eq.F.1. In the N_{eff} calculation, the number of hit PMTs which are included in the 50 nsec timing window after Čerenkov photon TOF¹ subtraction(N_{50}) is used. Then, the definition of N_{eff} is expressed by

$$N_{eff} = \sum_{i=1}^{N_{50}} \left[\frac{N_{all}}{N_{alive}} \times R_{cover}(\theta_i, \phi_i) \times e^{-\frac{L_i}{\lambda}} \times f_{period}(i) \times (X_i + \epsilon_{tail} - \epsilon_{dark}) \right] \quad (\text{F.1})$$

where N_{all} is the total number of PMTs in the detector which is equal to 11146, N_{alive} is $N_{all} - N_{dead}$ (approximately 100), and the other parameters will be described one by one.

The first term($\frac{N_{all}}{N_{alive}}$) in Eq.F.1 is a correction factor for dead PMTs.

The second term($R_{cover}(\theta_i, \phi_i)$) in Eq.F.1 is inverse of the photo-detection probability of each PMT. The definition of θ_i and ϕ_i is described in Fig.F.1. The $R_{cover}(\theta_i, \phi_i)$ distribution on the (θ_i, ϕ_i) plane is shown in Fig.F.2 .

The third term($e^{-\frac{L_i}{\lambda}}$) in Eq.F.1 is a correction factor for light attenuation in the water. L_i is distance between the vertex point and the i -th PMT. λ is the light attenuation length. For this correction, light attenuation length measured by μ -decay electrons is employed(Section.4.4.2).

The fourth term($f_{period}(i)$) in Eq.F.1 is a correction factor for gain variation of PMT at single photon-electron level. The gain is dependent on the production time of each PMT which is described in Section.4.1.2 Then

$$f_{period} = \begin{cases} 0.833 & \text{old PMT}(375\text{PMTs}) \\ 1 & \text{new PMT}(10771\text{PMTs}) \end{cases} \quad (\text{F.2})$$

The fifth term($(X_i + \epsilon_{tail} + \epsilon_{dark})$) in Eq.F.1 is a correction factor for the number of hit PMTs.

¹Time Of Flight

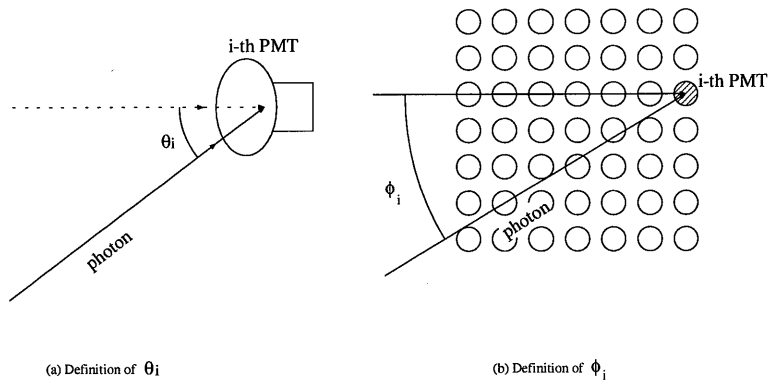


Figure F.1: Definition of θ_i and ϕ_i for photo-coverage correction.

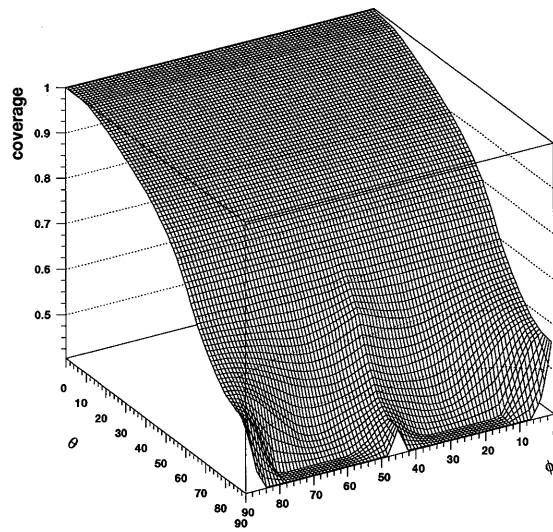


Figure F.2: $R_{cover}(\theta_i, \phi_i)$ distribution on the (θ_i, ϕ_i) plane

X_i is the expected number of photoelectrons detected by i -th hit PMT. This is estimated using the number of hit PMTs neighboring the i -th PMT. The definition of X_i is

$$X_i = \begin{cases} \frac{\lambda_i}{x_i} = \frac{\log \frac{1}{1-x_i}}{x_i} & x_i < 1 \\ 3 & x_i = 1 \end{cases} \quad (\text{F.3})$$

where x_i is the ratio of the number of hit PMTs to number of live PMTs in the neighboring PMTs around the i -th hit PMT (typically $9 \equiv$ neighboring 8 PMT + i -th PMT), and λ_i is a mean value which gives a Poisson distribution satisfying the following equation,

$$P_0 = \frac{\lambda_i^0 \times e^{-\lambda_i}}{0!} = 1 - x_i \quad (\text{F.4})$$

ϵ_{tail} is a correction factor for delayed hits originating from light reflection on the surface of PMT and ϵ_{dark} is a correction factor for dark noise. The definitions of them are:

$$\epsilon_{tail} = \frac{N_{100} - N_{50}}{N_{50}} \quad (\text{F.5})$$

$$\epsilon_{dark} = \frac{N_{pmt} \times Rate_{dark} \times 100nsec}{N_{50}} \quad (\text{F.6})$$

where N_{100} is the number of hit PMTs in 100nsec time window, and $Rate_{dark}$ is the dark noise rate in a run.

Based on a MC simulation, the correlation between N_{eff} and generated energy of electron events is demonstrated in Fig.F.3. Finally an event energy E is approximated by the following function of N_{eff} .

$$\begin{aligned} E &= 0.74736 + 0.13551 \cdot N_{eff} - 0.63038 \times 10^{-4} \cdot N_{eff}^2 + 0.45283 \times 10^{-6} \cdot N_{eff}^3 \\ &\quad - 0.68723 \times 10^{-9} \cdot N_{eff}^4 \\ &\approx 0.74736 + 0.13551 \cdot N_{eff} \end{aligned} \quad (\text{F.7})$$

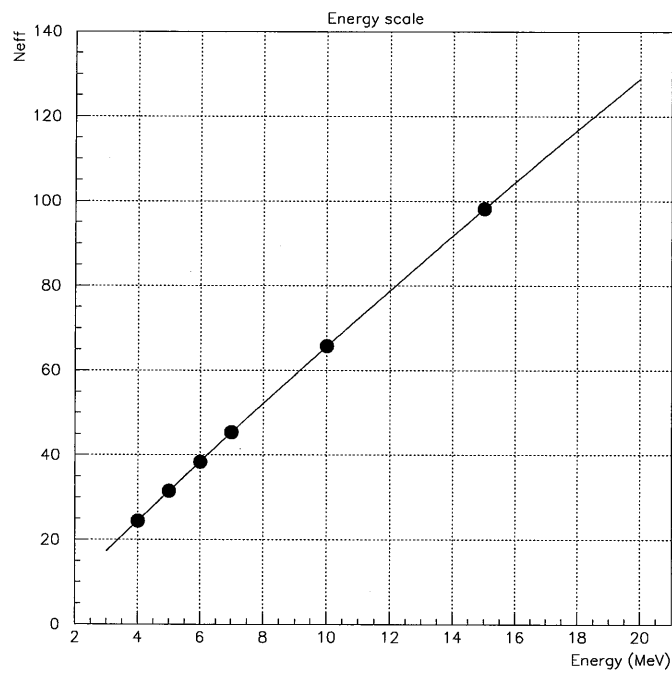


Figure F.3: The correlation between N_{eff} and generated electron energy by a MC simulation. The line is fitted by the 4th-degree polynomial function

Bibliography

- [1] J.N.Bahcall, “*Neutrino Astrophysics*”, (Cambredge,1989)
- [2] J.N.Bahcall *et al.* Phys.Rev.Lett., 20(1968)1209
- [3] R.Davis *et al.* Phys.Rev.Lett., 20(1968)1205
- [4] K.S.Hirata *et al.* Phys.Rev.Lett.,65(1990)1297
- [5] K.S.Hirata *et al.* Phys.Rev. D44(1991)2241, D45(1992)2170E
- [6] Y.Fukuda *et al.* Phys.Rev.Lett.,77(1996)1683
- [7] Z.Maki,M.Nakagawa and S.Skata, Prog.Theor.Phys. 49(1973)652
- [8] J.N.Bahcall and M.H.Pinsonneault, Rev.Mod.Phys. 64(1992)885
- [9] J.N.Bahcall and M.H.Pinsonneault, Rev.Mod.Phys. 67(1995)78
- [10] J.N.Bahcall and A.Glasner, Astrophys.J. 437(1994)485
- [11] J.N.Bahcall, Phys.Lett.B 338(1994)276
- [12] S.Turck-Chièze and I.Lopes, Ap.J. 408(1993)347
- [13] A.Dar and G.Shaviv, Technion report, 1994(unpublished)
- [14] B.T.Cleveland *et al.*,Preprint,1996
- [15] GALLEX Collaboration,P.Anselmann *et al.*,Phys.Lett. B285(1992)376; 285(1992)390; 314(1993)445, 327(1994)337; 357(1995)237; W.Hampel *et al.*, Phys.Lett.,B388(1996)354
- [16] SAGE Collaboration,A.I.Abazov *et al.*,Phys.Rev.Lett. 67(1991)3332; J.N.Abdurashitov *et al.*,Phys.Lett. B328(1994)234; Phys.Rev.Lett.,77(1996)4708
- [17] N.Hata and P.Langacker, Phys.Rev. D52(1995)420
- [18] N.Hata and P.Langacker, Phys.Rev. D56(1997)6107
- [19] L.Wolfenstein, Phys.Rev. D17(1978)2369,D20(1979)2634
- [20] S.P.Mikheyev and A.Yu.Smirnov, Sov.J.Nucl.Phys. 42(1985)913
- [21] D.L.Anderson, “Theory of the Earth”,(Blackwell scientific publications,1989)

- [22] L.D.Landau,Phys.Z. U.S.S.R. 1(1932)426
- [23] C.Zener,Proc.Roy.Soc. A137(1932)696
- [24] 't Hooft,G.,Phys.Lett. B37(1971)195
- [25] Weinberg,S.,Phys.Rev.Lett. 19(1967)1264
- [26] J.N.Bahcall,M.Kamionkowski,and A.Sirlin,Phys.Rev D51(1995)6146
- [27] A.Suzuki *et al.*,Nucl.Instr.and Meth. A329(1993)299
- [28] I.Thormählen, K.Scheffler, and J.Sraub, in *Water and Steam*, Proceedings of the 9th ICPS(Pergamon,Oxford,1980)
- [29] Rika Nenpyo(Chronological Scientific Tables)1995
- [30] A.Morel *et al.*, Limnology and Oceanography 22(1977)709
- [31] The Feynman lectures on physics Vol.IV 12-1
- [32] M.Nakahata,“*Search for 8B Solar Neutrino at KAMIOKANDE-II*”,Ph.D.thesis, Univ.of.Tokyo(1988),UT-ICEPP-86-03(unpublished)
- [33] Y.Fukuda,“*A Solution to the Solar Neutrino Problem by Matter-Enhanced Neutrino Oscillations at KAMIOKANDE-II*”,Ph.D.thesis,Osaka Univ.(1992)(unpublished)
- [34] K.Kihara,“*An Experimental Study on the 8B Solar Neutrino Flux in the Kamiokande-II Detector*”,Ph.D.thesis,Univ.of Tokyo(1992),ICRR-report-274-92-12(unpublished)
- [35] K.Inoue,“*Measurement of Neutrinos and Search for Anti-Neutrinos from the Sun at Kamiokande*”,Ph.D.thesis,Univ.of Tokyo(1994),ICRR-report-382-94-23(unpublished)
- [36] Y.Takeuchi,“*Measurement of Solar Neutrinos from One Thousand Days of Data at KAMIOKANDE-III*”,Ph.D.thesis,Tokyo Ins.of.Tech. (1995)(unpublished)
- [37] T.Suzuki, D.F.Measday and J.P.Roalsving, Phys.Rev. C35(1987)2212
- [38] P.Hänggi et.al,Phys,Lett. B51(1974)119
- [39] “*Feasibility Study for a Neutrino Observatory based on a large heavy water detector deep underground*” SNO-85-3W,(1985)
- [40] G.T.Ewan for the SNO Collaboration, “Frontiers of Neutrino Astrophysic”, eds. Y.Suzuki and K.Nakamura,(Universal Academy Press,1993),p147

O

O

Super-Kamiokande Collaboration

Institute for Cosmic Ray Research, University of Tokyo

Y. Fukuda, T. Hayakawa, K. Inoue, K. Ishihara, H. Ishino,
Y. Itow, T. Kajita, J. Kameda, S. Kasuga, Y. Koshio,
K. Martens, M. Miura, M. Nakahata, A. Okada, M. Oketa,
K. Okumura, M. Ota, N. Sakurai, M. Shiozawa, Y. Suzuki,
Y. Takeuchi, Y. Totsuka (spokesman)

National Laboratory for High Energy Physics (KEK)

J. Kanzaki, K. Nakamura, M. Sakuda, O. Sasaki, Y. Oyama

Bubble Chamber Physics Laboratory, Tohoku University

K. Fujita, A. Hasegawa, T. Hasegawa, S. Hatakeyama,
T. Iwamoto, T. Kinebuchi, M. Koga, T. Maruyama, H. Ogawa,
M. Onada, M. Saito, A. Suzuki, F. Tsushima

Tokai University

M. Eto, M. Koshihara, M. Nemoto, K. Nishijima

Department of Physics, Osaka University

A. Kusano, Y. Nagashima, M. Takita, T. Yamaguchi,
M. Yoshida

Niigata University

T. Ishizuka, Y. Kitaguchi, H. Koga, K. Miyano, H. Okazawa,
M. Takahata

Department of Physics, Tokyo Institute of Technology

Y. Hayato, Y. Kanaya, K. Kaneyuki, Y. Watanabe

Gifu University

S. Tasaka

Miyagi University of Education

M. Mori

Department of Physics, Kobe University

S. Echigo, M. Kohama, A.T. Suzuki

Institute for Nuclear Study, University of Tokyo

K. Chikamatsu, E. Ichihara, T. Inagaki, K. Nishikawa,
A. Sakai

Boston University

M. Earl, A. Habig, E. Kearns, S.B. Kim, M. Messier,
J.L. Stone, K. Scholberg, L.R. Sulak
Brookhaven National Laboratory
M. Goldhaber

University of California, Irvine

T. Barszczak, W. Gajewski, P.G. Halverson, J. Hsu,
L.R. Price, W.R. Kropp, F. Reines, H.W. Sobel
California State University, Dominguez Hills
K. Ganezer, W. Keig

George Mason University

R.W. Ellsworth

University of Hawaii

J. Flanagan, J.G. Learned, S. Matsuno, V. Stenger,
D. Takemori
Los Alamos National Laboratory
T.J. Haines

Louisiana State University

E. Blaufuss, R. Sanford, R. Svoboda, M.R. Vagins

University of Maryland

M.L. Chen, Z. Conner, J.A. Goodman, G. Sullivan

State University of New York, Stony Brook

J. Hill, C.K. Jung, C. Mauger, C. McGrew, B. Viren,
C. Yanagisawa

University of Warsaw

D. Kielczewska

University of Washington

J. George, A. Stachyra, L. Wai, J. Wilkes, K. Young

O

O